NAVAL POSTGRADUATE SCHOOL

MONTEREY, CALIFORNIA

THESIS

FRICTION STIR WELDING OF HT9 FERRITIC-MARTENSITIC STEEL: AN ASSESSMENT OF MICROSTRUCTURE AND PROPERTIES

by

Lara L. Ray
June 2013

Thesis Advisor: Luke N. Brewer
Second Reader: Joseph C. Farmer

Approved for public release; distribution is unlimited

THIS PAGE INTENTIONALLY LEFT BLANK

REPORT DOCUMENTATION PAGE			Form Approved OMB No. 0704-0188
Public reporting burden for this collection of information is estimated to average 1 hour per response, including the time for reviewing instruction, searching existing data sources, gathering and maintaining the data needed, and completing and reviewing the collection of information. Send comments regarding this burden estimate or any other aspect of this collection of information, including suggestions for reducing this burden, to Washington headquarters Services, Directorate for Information Operations and Reports, 1215 Jefferson Davis Highway, Suite 1204, Arlington, VA 22202-4302, and to the Office of Management and Budget, Paperwork Reduction Project (0704-0188) Washington DC 20503.			
1. AGENCY USE ONLY ***(Leave blank)***	**2. REPORT DATE** June 2013	**3. REPORT TYPE AND DATES COVERED** Master's Thesis	
4. TITLE AND SUBTITLE FRICTION STIR WELDING OF HT9 FERRITIC-MARTENSITIC STEEL: AN ASSESSMENT OF MICROSTRUCTURE AND PROPERTIES		**5. FUNDING NUMBERS**	
6. AUTHOR(S) Lara L. Ray			
7. PERFORMING ORGANIZATION NAME(S) AND ADDRESS(ES) Naval Postgraduate School Monterey, CA 93943-5000		**8. PERFORMING ORGANIZATION REPORT NUMBER**	
9. SPONSORING /MONITORING AGENCY NAME(S) AND ADDRESS(ES) N/A		**10. SPONSORING/MONITORING AGENCY REPORT NUMBER**	
11. SUPPLEMENTARY NOTES The views expressed in this thesis are those of the author and do not reflect the official policy or position of the Department of Defense or the U.S. Government. IRB Protocol number ____N/A____.			
12a. DISTRIBUTION / AVAILABILITY STATEMENT Approved for public release; distribution is unlimited		**12b. DISTRIBUTION CODE**	

13. ABSTRACT (maximum 200 words)

This thesis explores the processing-microstructure-property relationships in friction stir welded (FSW) HT9A ferritic-martensitic steel. HT9 has previously been studied as a structural component for fusion/fission based reactors; however, the changes in material microstructure and properties after friction stir welding have not been considered. HT9A steel plate was friction stir welded with a series of increasing heat inputs. The microstructure of this welded material was characterized using optical and electron microscopy. The mechanical properties of the welded material were determined using nanoindentation and microhardness measurements. In addition, electrochemical impedance spectroscopy (EIS) in molten lithium fluoride was used to assess the high temperature corrosion resistance of the welded material in the harsh environments found in fusion reactors. The quality of the friction stir welds was excellent, and the basic ferritic-martensitic microstructure was maintained for all of the conditions used. Some reduction in hardness was observed in the welded material, particularly in the heat affected zones. The high temperature corrosion response of the welded material was comparable to, or slightly better than, the base plate material.

14. SUBJECT TERMS Friction Stir Welding, HT9, Corrosion, EIS, ferritic martensitic, high chromium, high temperature corrosion, LiF			**15. NUMBER OF PAGES** 115
			16. PRICE CODE
17. SECURITY CLASSIFICATION OF REPORT Unclassified	**18. SECURITY CLASSIFICATION OF THIS PAGE** Unclassified	**19. SECURITY CLASSIFICATION OF ABSTRACT** Unclassified	**20. LIMITATION OF ABSTRACT** UU

NSN 7540-01-280-5500 Standard Form 298 (Rev. 2-89)
Prescribed by ANSI Std. 239-18

THIS PAGE INTENTIONALLY LEFT BLANK

Approved for public release; distribution is unlimited

FRICTION STIR WELDING OF HT9 FERRITIC-MARTENSITIC STEEL: AN ASSESSMENT OF MICROSTRUCTURE AND PROPERTIES

Lara L. Ray
Lieutenant, United States Navy
B.A. Biology, University of San Diego, 2008

Submitted in partial fulfillment of the
requirements for the degree of

MASTER OF SCIENCE IN MECHANICAL ENGINEERING

from the

NAVAL POSTGRADUATE SCHOOL
June 2013

Author: Lara L. Ray

Approved by: Luke N. Brewer, Ph.D.
Thesis Advisor

Joseph C. Farmer, Ph.D.
Second Reader

Knox T. Millsaps, Ph.D.
Chair, Department of Mechanical and Aerospace Engineering

THIS PAGE INTENTIONALLY LEFT BLANK

ABSTRACT

This thesis explores the processing-microstructure-property relationships in friction stir welded (FSW) HT9A ferritic-martensitic steel. HT9 has previously been studied as a structural component for fusion/fission based reactors; however, the changes in material microstructure and properties after friction stir welding have not been considered. HT9A steel plate was friction stir welded with a series of increasing heat inputs. The microstructure of this welded material was characterized using optical and electron microscopy. The mechanical properties of the welded material were determined using nanoindentation and microhardness measurements. In addition, electrochemical impedance spectroscopy (EIS) in molten lithium fluoride was used to assess the high temperature corrosion resistance of the welded material in the harsh environments found in fusion reactors. The quality of the friction stir welds was excellent, and the basic ferritic-martensitic microstructure was maintained for all of the conditions used. Some reduction in hardness was observed in the welded material, particularly in the heat affected zones. The high temperature corrosion response of the welded material was comparable to, or slightly better than, the base plate material.

THIS PAGE INTENTIONALLY LEFT BLANK

TABLE OF CONTENTS

LIST OF FIGURES

THIS PAGE INTENTIONALLY LEFT BLANK

LIST OF TABLES

THIS PAGE INTENTIONALLY LEFT BLANK

LIST OF ACRONYMS AND ABBREVIATIONS

AS	Advancing side
ASTM	American Society for Testing and Materials
CSM	Continuous Stiffness Measurement
CSZ	Center Stir Zone
EBSD	Electron Backscatter Diffraction
EBW	Electron Beam Welding
EDS	Energy-dispersive Spectroscopy
EIS	Electrochemical Impedance Spectroscopy
FIB-SEM	Focused Ion Beam- Scanning Electron Microscopy
FSP	Friction stir processing
FSW	Friction Stir Welding
HAZ	Heat Affected Zone
HF	Hydrogen Fluoride
IF	Interstitial Free
LLNL	Lawrence Livermore National Laboratory
NAB	Nickel aluminum bronze
NIST	National Institute of Standards and Technology
NPS	Naval Postgraduate School
ODS	Oxygen Dispersed Steel
OIM	Orientation Imaging Microscopy
OM	Optical Microscopy
PCBN	Polycrystalline cubic boron nitride
RS	Retreating side
SEM	Scanning Electron Microscopy
SZ	Stir Zone
TIG	Tungsten Inert Gas
TF	Tritium Fluoride
TMAZ	Thermo-Mechanical Affected Zone

THIS PAGE INTENTIONALLY LEFT BLANK

ACKNOWLEDGMENTS

I would like to thank my husband, Rich for his continued support, guidance and faith through this process. Our daughter, Emma who was born shortly after I completed my thesis, gave me the strength to persevere and complete my thesis on time. I would also like to thank the many people who helped make my thesis research possible and who spent countless hours assisting me collect, interpret and analyze my data. Most notably: Professors Luke Brewer, Joseph Farmer, Terry McNelly, and Sarath Menon. Additionally Jim Ferreira, and Commander Brad Baker provided invaluable assistance in mentoring and collaboration throughout the process. Ultimately I would like to express my gratitude to my parents for providing the opportunities that have allowed me to pursue my education.

THIS PAGE INTENTIONALLY LEFT BLANK

I. BACKGROUND AND MOTIVATION

A. MOTIVATION

Structural materials efforts for future nuclear-based fission and fusion reactors are driven by the desire to find suitable materials that can withstand high temperatures, neutron bombardment, and exposure to reactive coolants. In a fusion reactor, the highest material damage occurs in the first wall because it will be exposed to the highest neutron, gamma ray and charged particle currents produced in the fusion chamber [1]. Material damage occurs as a result of atomic displacement and helium gas production. In addition, extremely high temperatures (about 150 million degrees) taking place in the plasma burn cycle, will induce severe cyclic thermal stresses in the first-wall/blanket structure and could result in stress corrosion cracking and/or intergranular fracture [2]. Consequently, the use of reactive coolants and their effect on the fatigue properties of structural materials is an important consideration in material selection and design of first-wall/blanket systems. In order to decrease operational costs of a fusion reactor, replacement of first wall structural materials should be minimized. Therefore, long-term stability and predictability of these materials are extremely important from a waste material generation point of view [2, 3].

Structurally, one of the largest challenges in building a fusion/fission reactor is in the fabrication and joining of tubing and structural components. Joining of these new alloys poses a challenge and limits their application in nuclear reactors. Traditionally, fusion welding has been used to join alloy components. Unfortunately, fusion welding of components can result in a number of problems such as loss of strength, stress corrosion cracking (SCC) susceptibility, loss in fatigue performance, and increased hot-cracking sensitivity as a result of the highly corrosive environment [2, 4]. In an attempt to structurally improve reactor components, an improved welding technique, which allows metals to be welded into relatively complicated shapes and is metallurgically stable over a wide temperature range, needs to be identified. Based on research involving possible

alloy candidates, it is believed that friction stir welding (FSW) may potentially improve the joining of advanced steels for reactor applications [5-11].

B. HIGH CHROMIUM STEELS FOR REACTOR ENVIRONMENTS

Renewed interest in the susceptibility of ferritic/martensitic steels to the corrosive environment of high temperature molten salt coolants for nuclear fusion reactors has prompted the study of thermodynamic and mechanical properties of cladding materials in fast reactor design [12]. In the 1970's, high chromium (9-12%) ferritic/martensitic steels became candidates for such applications [13]. One candidate of particular interest was Sandvik HT9, nominally Fe-12Cr-1MoVW-0.2C, a martensitic steel originally developed for conventional power plants. HT9 has been extensively tested [14-17] for its performance in structural applications in fusion reactors and has shown to have excellent resistance to swelling and radiation damage, thus providing an excellent creep and swelling resistant alternative to austenitic stainless steels [18].

Figure 1 is a depiction of a nuclear fusion chamber developed at Lawrence Livermore National Laboratory (LLNL), with tungsten nominally comprising the first wall. Broad ranges of refractory, radiation-tolerant first wall structural material have been proposed for fusion-fission reactor structures. Possible candidates to replace tungsten include, but are not limited to, a wide variety of refractory alloys, ferritic steels with oxide-dispersion strengthening, and ferritic/martensitic steels with high chromium content (8-30%Cr) including HT9. The coolant used in this diagram is Li_2FBeF_4, also known as Flibe, which is one of many possible coolants used in fusion reactors.

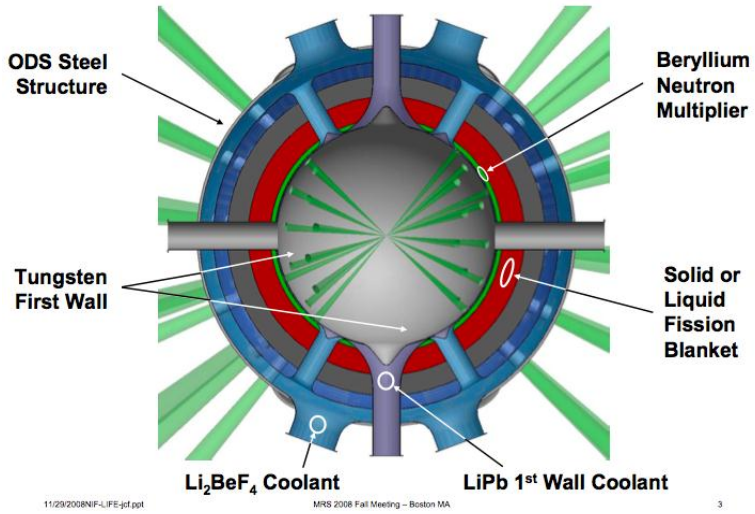

Figure 1. Lawrence Livermore National Laboratory depiction of the fusion/fission chamber. From Farmer et al. [19].

C. JOINING OF HIGH CHROMIUM FERRITIC-MARTENSITIC STEELS

Although the thermo-mechanical and radiation resistance properties of HT9 are promising, joining of these advanced materials is particularly problematic. Welds are often a source of component failure; and traditional fusion welds, in particular, can cause a loss of strength, hot-cracking sensitivity, and accelerated corrosion. A corrosive, irradiated environment further exacerbates weld joint failure, leading to deterioration of mechanical properties such as, a decrease in toughness in the weld nugget, weakening in the HAZ region, and a 25% decrease in tensile strength when compared to base metal [4, 20]. Despite the extensive research and development in welding high chromium steels, the performance of these welds is still considered to be a life-limiting factor at high temperatures and when exposed to corrosive environments [21]. While high chromium, ferritic-martensitic alloys, have been thoroughly explored as a plate material and as a joined material using traditional fusion welding [21-23] such as Tungsten Inert Gas (TIG) welding and Electron beam welding (EBW) [21, 23], the performance of friction stir welded (FSW) joints however, has not been addressed in the literature.

TIG welding has been one of the predominant welding processes used for joining high chromium steels [12]. Although useful for welding thin sections, a major limitation

of autogenous TIG welding process is in its limited heat input, and thus only suitable for joining sections 1/4 inch or thinner [24]. While regarded as having a low heat input compared with other types of welding, TIG welding is still a fusion welding process, where melting of metal is required for coalescence to occur. Unlike solid state welding, the lower heat input required in fusion welding leads to an uneven particle distribution in the heat-affected zone (HAZ). This uneven particle distribution leads to the formation of a coarser martensitic structure, which decreases the toughness of ferritic/martensitic steels [20, 22]. As a result, the weld joint and HAZ is often over-strengthened, and can lead to failure in the base metal, close to the HAZ, under stress [20, 22]. Lucon reported a similar trend in conventional TIG welding of EUROFER97 (9%Cr, 0.12%C, 1%W). An unequal distribution of particles was correlated to higher hardness and tensile properties as well as inferior ductility, toughness, and higher irradiation hardening and embrittlement [25]. In oxide dispersion strengthened (ODS) steels, such as MA956, this uneven distribution of strength seen in TIG welding is attributed to the agglomeration of the oxide dispersants [26], thus leading to a decrease in mechanical properties such as lowered yield strength, inferior ductility, and increased embrittlement in comparison to that of the base metal. An additional study concluded that the tensile strength values obtained in TIG weld joint were comparable to that obtained in (Electron beam) EB weld joints of low activation ferritic/martensitic steel (nominally a 9Cr steel) [27]. Lindau concluded, however, that EB welds on an ODS variant of EUROFER, resulted in weak weld seams, deterioration of mechanical properties and an unfit joining process when used in high loading applications [22, 28]. The addition of a post weld heat treatment has been observed to mitigate the effects thus far presented [22, 23, 29], and therefore, the welding of reduced activation ferritic/martensitic steels therefore requires adequate preparation and control to avoid cracking during welding.

While TIG welding has been used in the past as one of the primary means for joining ferritic-martensitic steels used in fusion applications, based on the findings there remains considerable room for improvement in the joining of these materials and in the performance of these joints under high stress, high temperature environments.

Friction stir welding (FSW) is a relatively new solid-state joining process invented at the Welding Institute of UK in 1991. The basics of FSW involve rotating a friction-tool at high rotational speeds into the metal to be welded. The shoulder makes firm contact with the top surface of the work-piece. Heat generated by friction softens the material, while severe plastic deformation and tool rotation allows for the highly plasticized material to be transported from the front of the tool to the trailing edge where it is forged into a joint [30]. Mishra discusses a detailed review of the FSW process to include process parameters, tool properties, material selection, and microstructure evolution in his paper, which focuses primarily, although not exclusively, on aluminum alloys [5]. FSW offers many advantages over fusion welding approaches, including maintaining well-featured microstructures and mechanical properties. Nandan demonstrated in his analysis of FSW of steels, that the microstructure in the weld region was not grossly deformed, but surprisingly homogenous throughout the weld joint. As a result, there should be no detrimental corrosion behavior associated with FSW. In fact, he notes that there may even be an advantage since the chemical composition of the weld region is identical to that of the plates, i.e. a homogenous electrochemical potential [30].

Unlike fusion welding, FSW has much lower heat inputs and does not require melting of the steel. As a result there are fewer metallurgical changes in the HAZ and weld nugget, resulting in a decrease in susceptibility to hydrogen-assisted cracking [31]. Secondly, as a solid-state process, friction stir welding can avoid the formation of solidification and hydrogen cracking in addition to porosity associated with fusion welding processes [30]. FSW of steels have also shown to exhibit good ambient-and elevated temperature tensile strengths [6, 7, 20].

Friction stir welding has increasingly been applied to steels over the past five years, enabled primarily by improvements in tool development. While high speed steel or WC-Co tools can be used for aluminum and copper alloys, FSW of steel generally requires even more refractory tools. Polycrystalline cubic boron nitride (PCBN) has become the standard for FSW tools applied to steels [32]. In addition to being quite refractory, PCBN also has a low coefficient of friction, which produces a smoother weld

finish. The largest drawback for these tools is the high cost, which can be several thousand dollars per tool.

FSW has been successfully used to join carbon steels [33-35], high strength low-allow (HSLA) steels [31, 36], ferritic stainless steels [37-39], austenitic steels [20], and ODS steels [7, 8, 40, 41]. The linkage between the composition of the steel and the microstructure produced by FSW is much more critical than in aluminum alloys. The $\alpha \rightarrow \gamma \rightarrow \delta$ phase transformations can cause complex, multi-phase microstructures, some of which are cooling rate sensitive (e.g., martensite) [20]. The work of Cui et al. demonstrated successful FSW on carbon steels with carbon contents up to 0.5 weight percent [35]. For carbon contents less than 0.2 weight percent, a simple microstructure of ferrite and pearlite was observed. For carbon contents higher than this level, a ferritic-martensitic microstructure was observed. The phase populations were observed to be sensitive to the tool rotational and traverse speeds as these directly impact the temperature of the welding and the cooling rate.

Fully ferritic stainless steels ($\geq$11 weight percent Cr) can be readily joined by FSW as they do not experience the $\alpha \rightarrow \gamma$ phase transformation [20, 37-39]. The FSW of ferritic stainless steels (<0.08 weight percent carbon) all showed a grain refinement from the base plate metal (~30μm) to the center of the stir zone (~5μm). The results of Barak and Cho showed only the ferrite phase before and after welding, while Lakshminarayanan demonstrated a ferritic-martensitic microstructure after welding. This paper points out the importance of applied strain in promoting martensite formation. FSW applies very high strains ($\sim\varepsilon_p$=10) [42], and this influence must be considered when considering the formation of martensite during FSW. All of the reported work on FSW of ferritic stainless steels describes an increase in hardness in the stir zone as compared with the base metal. The only report of FSW on a ferritic-martensitic stainless steel is the work of Chung, which applied this approach to a dissimilar weld between F82H (ferritic-martensitic) and SUS304 (austenitic stainless) [43].

D. CORROSION OF FERRITIC/MARTENSITIC STEELS IN HIGH TEMPERATURE MOLTEN SALT COOLANTS

In addition to joining challenges, the general corrosion resistances of new reactor steels in high temperature, corrosive coolant environments are a key potential limitation for these materials. Corrosive attack in a high-temperature molten-salt environment, specifically in alkali salts, can have a detrimental effect on the mechanical properties of HT9, in particular increased fatigue crack propagation, and intergranular fracture leading to a reduction in fatigue life [2]. While research has been done involving the corrosive attack of alkali salts such as Flibe, Flinak and LiF on ferritic martensitic steels [19, 44, 45] there is still limited research involving the corrosive attack of these salts on HT9, specifically for the alkali salt LiF. Understanding the corrosive mechanism of HT9 in alkali salts, as well as the significance of welded joints, is crucial in the implementation of this steel as a first wall material.

Corrosion of HT9 in molten fluoride salts exposed at high temperatures (600-900 ° C) may limit the life of advanced reactor systems. Cheng et al. [46] discusses the corrosion mechanism of chromium steel exposed to high temperature coolants, to include the generalized oxidative corrosion reaction of reduced metal (M) with the molten fluoride salt (XF). The reaction is given as follows: $M + XF \rightarrow MF + X$, where X represents lithium, sodium, beryllium, or transmutation products, such as tritium [47]. In this mechanism, the transmutation of lithium produces hydrogen isotopes, which react with free fluoride forming two highly corrosive constituents; hydrogen fluoride (HF) and tritium fluoride (TF). The high temperature encountered in a nuclear reactor further accelerates this problem of corrosion. The corrosion mechanism of HT9 in these electrolytes is not yet completely understood, however, reasonable assumptions can be made based upon published experimental data involving the corrosion of high chromium, ferritic-martensitic steels (12-22wt%Cr) in high temperature alkali salts, to include: Hastelloy-N (16wt%Cr) [48], MA956 (18.7wt%Cr) [41], JLF-1 (Fe-9Cr-2W) [49]and SUS430 (Fe-18Cr) [49]. In a study conducted at Lawrence Livermore National Laboratory, an oxygen-dispersed steel (ODS), MA956 (18.5-21.5%Cr) was exposed to Flinak between the temperatures of 600°C and 900°C [44]. The following observations

included: the steel experienced corrosion between the temperatures of 550°C and 900°C but was dramatically accelerated, indicated by a decrease of polarization resistance from 120Ω to 0Ω at temperatures above 800°C. In addition, exposure to the salt resulted in the preferential dissolution of chromium into electrolytic solution, until the point of saturation.

This mechanism for the corrosive attack and preferential dissolution of chromium from Fe-Cr alloys was best described by Williams et al. [48], where the corrosive effects of LiF on Hastelloy N and Inconel were addressed. Unlike the more conventional oxidizing media, the products of oxidation of metals in molten fluoride tend to be completely soluble [48]. As a result, passivation does not occur and corrosion of the solid depends directly on the thermodynamic driving force of the corrosion reaction [48]. By understanding the thermodynamics of the reaction, i.e. the Gibbs free energy of each component, the most active of the metal components can be found, and therefore, the most likely component to be attacked and leached from the system. The free energies of formation for the various alloy components of Inconel and Hastelloy N showed that CrF had the largest free energy, thus indicating that chromium was the most active of metal components, and therefore any oxidative attachment should be expected to show selective attack on the chromium. The study further indicated that the removal of chromium from the alloy occurred primarily in the presence of higher temperatures ($800°C\ vs\ 900°C$), resulting in the formation of discrete voids in the alloy. The voids were not confined to the grain boundaries but are relatively uniformly distributed throughout the alloy surface in contact with the melt [48]. Farmer et al. found a similar mechanism, where the preferential chromium was seen to leach from high chromium ODS steels (12-14wt%Cr) after exposure to fluoride-based molten salts [44]. Furthermore, at some point, the solution became saturated with chromium, and dissolution of the steel ceased [44]. Similar to the study by Williams, Farmer found that galvanic coupling, increased temperature and the formation of transmutation products (HF and TF), a result of neutron bombardment; seem to accelerate the corrosion of the steel.

Another key factor to consider is the different chromium content in each of these alloys. As previously discussed, corrosion occurs predominantly from the dealloying of Cr from these Cr bearing alloys, an affect that is particularly pronounced at the grain boundaries [48, 50]. This correlation of corrosion to chromium content was further investigated by Olson, where static corrosion tests in Flinak and a molten chloride salt (KCl-MgCl2) were undertaken to determine the corrosion behavior of several candidate materials to include Hastelloy-N (16wt%Cr) and Hastelloy-X (22wt%Cr) [50]. As previously seen, selective leaching of chromium from the metal, particularly at the grain boundaries were observed. Furthermore, the alloy weight-loss/area due to molten fluoride salt exposure correlated with the initial chromium content of the alloys and was consistent with the chromium content measured in the salts after corrosion tests.

Exposure of the Hastelloys to Flinak, resulted in visible grain boundary attack, resulting from the preferential leaching of Cr. It can be seen in that grain boundaries in the Hastelloy-X matrix, has been depleted in chromium (Figure 2).

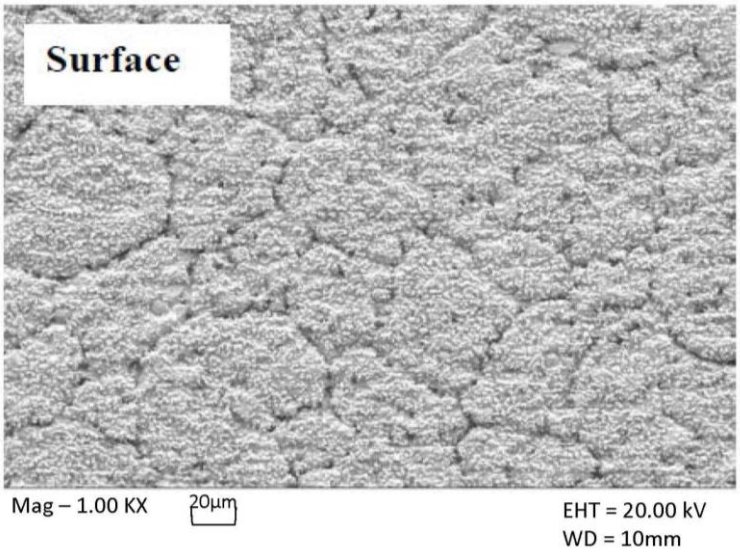

Figure 2. SEM image of Hastelloy-X after corrosion tests in molten Flinak salt at 850°C. From Olson [50].

Figure 2 confirms the preferential leaching of Cr near the grain boundaries. In contrast, Hastelloy-N experienced minor corrosion in comparison to Hastelloy-X (50µm verses 300 µm depth of grain boundary attack), due to the lower Cr content present in Hastelloy-N. A comparison image can be seen in Figure 3, where an SEM was taken of Hastelloy-N after the same exposure to Flinak. These results were confirmed using Energy Dispersive Spectroscopy (EDS) x-ray mapping, and cross sectional imaging. Both assessments confirmed the results found in the SEM imaging.

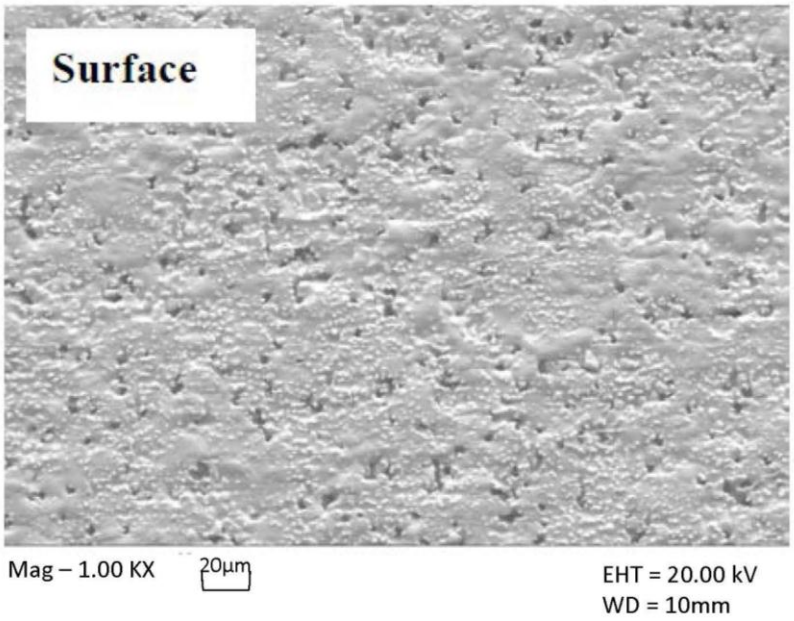

Figure 3. SEM image of Hastelloy-N after corrosion tests in molten Flinak salt at 850°C. From Olson [50].

Although the mechanism for corrosion of ferritic/martensitic steels is complex and not fully understood, a few conclusions can be drawn from these studies. First, the mechanism for the corrosive attack of high chromium ferritic-martensitic steels involves the preferential dissolution of chromium into solution, second, the corrosion rates slow as saturation of chromium is reached in the circulating coolant, but increased with an increase in temperature. Finally, initial chromium content affects the rate of corrosion.

Alloys with higher chromium content were seen to have more severe grain boundary attack than similar alloys with lower chromium content.

1. Study of corrosion resistance using Electrical Impedance Spectroscopy (EIS)

Electrochemical impedance spectroscopy (EIS) has been used in the past to measure the temperature dependence of charge transfer kinetics *in situ* for high chromium steels [44]. EIS studies of the corrosion resistance of ODS (oxide dispersion strengthened) FM (ferritic martensitic) steels in high-temperature molten-salt coolants has been reported by Farmer and El-Dasher [44, 51-53]. However, to the best of our knowledge, no comprehensive studies showing differences in the passive film stability and corrosion resistance of HT9A subjected to FSW or friction stir processing (FSP) have yet been published. In regard to the effects of FSW and FSP on alloy microstructure, the effects on the microstructure of nickel-aluminum bronze (NAB) have been studied [54]. Subsequently, EIS has been used to quantify the beneficial effects of FSW on the passive film stability of NAB [51]. This data was modeled using a wide range of electric circuit models in order to represent corrosion microstructures of varying complexity. Based on these previous studies, EIS is an effective means of revealing differences in passive film behavior on HT9A as a result of such friction stir welding.

E. THESIS OBJECTIVES: FEASIBILITY OF FSW ON HT9A STEEL

The work in this thesis assesses the feasibility of FSW on joining of HT9A, so that it may be utilized in future first-wall fusion reactor designs. The objectives of this thesis are as follows:

1. *Demonstrate the feasibility of FSW on HT9A steel.*

Feasibility of FSW of HT9A will be verified via in-depth observations of both microstructural and mechanical properties.

2. *Determine microstructural and mechanical property relationships subsequent to FSW*

Utilizing scanning electron microscopy (SEM), electron backscatter diffraction, energy-dispersive spectroscopy (EDS), microhardness, nanoindentation and optical images, a correlation between microstructural and mechanical properties will be drawn.

3. *Assess molten fluoride corrosion behavior of HT9A plate and FSW'd material.*

Using electrochemical impedance spectroscopy (EIS), a correlation between the instantaneous rate of corrosion at either 600°C or 800°C, and the different welding parameters i.e. TIG and FSW of HT9 will be made. Based on current literature, it is hypothesized that TIG welded HT9A will perform poorly in comparison to base metal, while FSW HT9A should perform equally or better than base metal.

II. METHODS

A. HT9A FABRICATION AND FRICTION STIR WELDING

The material used in this study was HT9A, a high Cr ferritic steel variant of HT9 with a measured material composition shown in Table 1.

C	Cr	Mo	Mn	Si	W	Fe	Nb
0.05	12.0	<0.0001	0.51	0.04	1.94	Bal.	<0.0001

Table 1. Chemical composition of HT9 (wt%).

Lawrence Livermore National Laboratory commercially procured the HT9A plate. Production of the plate included hot rolling (approximately 2025F/1100C) it to 5mm thickness, followed by air-cooling. It should be noted that this composition is a modification of the traditional HT9 composition with less carbon and more tungsten than in older formulations [55]. Friction stir welding was performed by MegaStir Technologies (Provo, Utah). A photograph of the welded HT9A plate is shown in Figure 4. The tool depth was established by the pin length and once the desired tool or plunge depth was reached, the tool was held in position for 7 sec., i.e., the dwell time to heat the tool and the plate. Weld parameters included a tool travel speed of 4.8 mm/sec (2 IPM) with rotation speeds of 400, 350, and 300 rpm. Weld tools were fabricated using a Q60 grade of polycrystalline cubic boron nitride. The tool design consisted of a flat scroll shoulder with a small pin with three flats (Figure 5). This flat tool design is believed to be more appropriate for friction stir welding a small diameter curved surface due to the fact that there is more shoulder contact compared to a convex shoulder [56].

Figure 4. The friction stir welded HT9A plate, 12.7cm in length, with 8.9cm weld path.

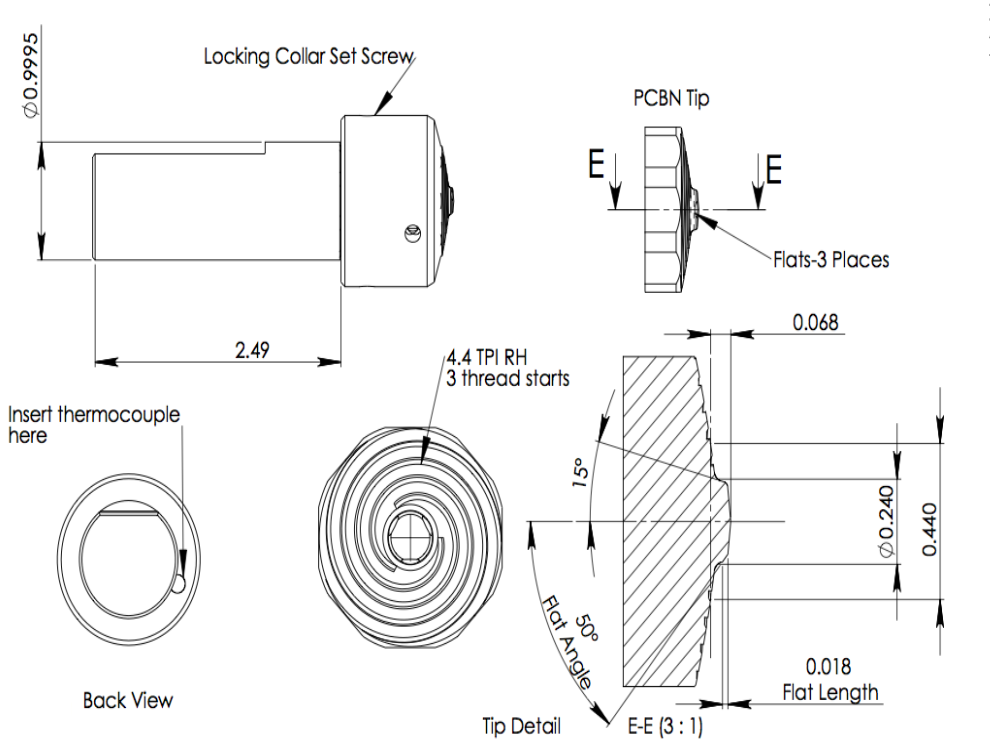

Figure 5. Schematic of tool design used for FSW of HT9A. Units are in inches.

1. TIG Welded Plate

TIG welding of HT9A was accomplished by the Naval Postgraduate School welding facility using Argon gas, 308 stainless steel filler rod, a 45° approach angle and 80 amperes of current.

2. HIGH TEMPERATURE CORROSION EXPERIMENTS

a. *Reference and Working Electrode Production*

For both the TIG welding and the Friction Stir Welded HT9A samples, the design for the buttons consisted of a reference electrode measuring 0.635 cm (0.25 (in)) in diameter, and a working electrode with 0.95 cm (0.375 (in)) in diameter. Both working and reference electrode contained a standard 6-32 threaded hole, which allowed it to be mounted to the 316 stainless steel rod in the electrochemical cell. Dimensions for the buttons and threaded hole can be seen in Figure 6. Buttons for 350 rpm, 400 rpm friction stir welded and TIG welded plates were fabricated by Full Spectrum Machining.

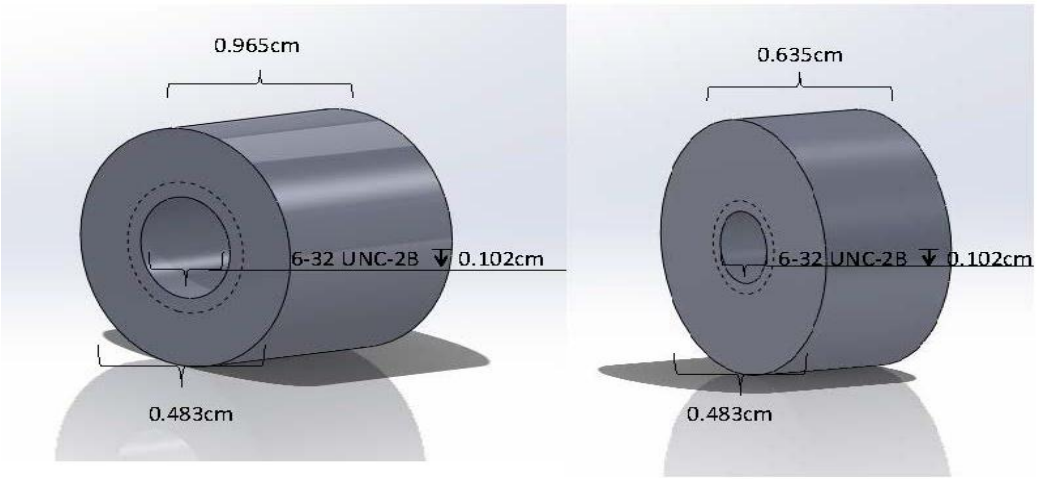

Figure 6. Reference electrode and working electrode geometries.

b. *Molten Lithium Fluoride EXPOSURE*

Exposure to high temperature lithium fluoride (LiF) was accomplished via an electrochemical cell developed by Lawrence Livermore National Laboratory as seen

in Figure 7. The working electrode, reference electrode, and counter electrode, which were mounted on a 316ss rod contained in hollow ceramic rods, can be seen in Figure 6a. The material being tested was held in the electrochemical cell by a machined ceramic plug. This figure also shows the cell being operated at 800°C. The electrochemical cell was designed to be used with a crucible furnace in a glove box with carefully controlled glove box environment containing argon gas, limiting oxygen and moisture to less than 1 part per million. Using this three-electrode electrochemical cell, the working electrode was subjected to a small amplitude potential modulation ($\pm 5\,mV$) and the resultant current response was measured.

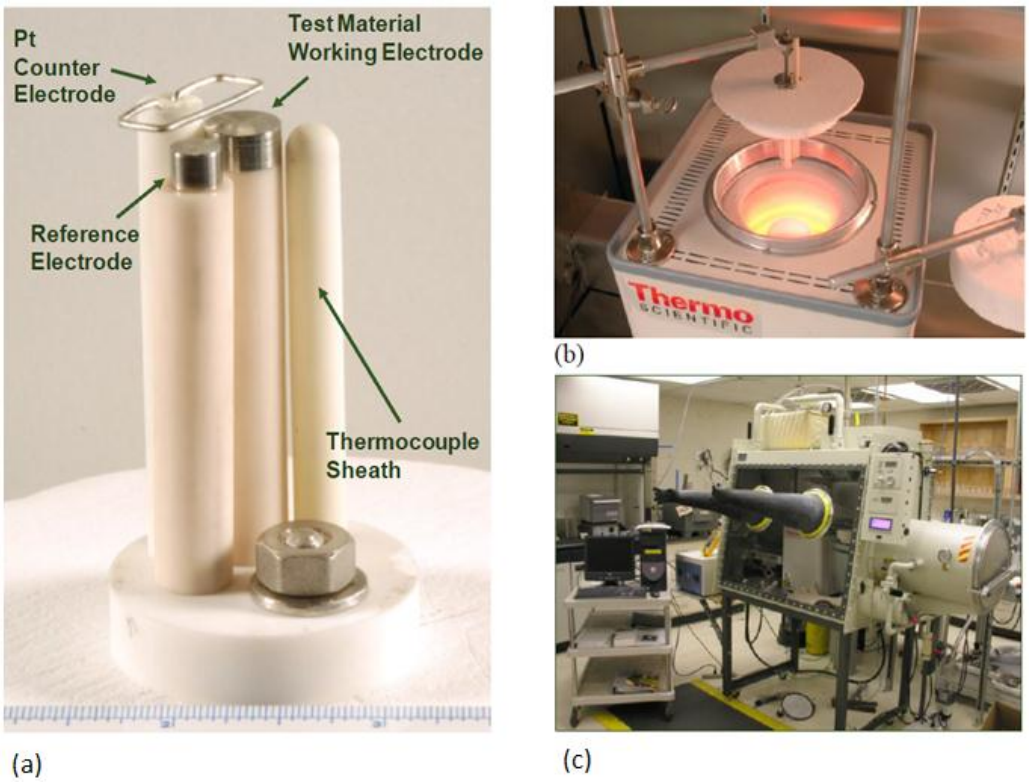

Figure 7. Setup for working, reference and platinum counter electrode can be seen in (a). Crucible at 800°C can be seen in (b). Glove box where crucible is contained, seen in (c) [44].

Two exposures to molten LiF were completed for each welding parameter. The first exposure was at 600°C and the second exposure was at 800°C. In order to reach

these temperatures, the LiF in powder form was heated above its melting temperature (845°C) to 950°C for 1 hour to ensure sufficient melting. The temperature was then reduced to ~40°C above the required experimental temperature. This sequence was performed to allow for a slight drop in temperature as the electrochemical cell was loaded into crucible.

c. *Electrochemical Impedance Spectroscopy*

Electrochemical impedance spectroscopy (EIS) was used to measure, *in situ,* the temperature dependence of charge transfer kinetics. The three-electrode electrochemical cell shown in Figure 7 has enabled the corrosion of HT9A steel to be analyzed via linear polarization and electrochemical impedance spectroscopy. The working electrode was subjected to a small amplitude ($\pm$ 10mV) potential modulation centered at either the reference electrode or the open circuit corrosion potential, and the resultant current response measured. Settings can be seen in table 2.

The successful utilization of EIS to determine the corrosion response of a material requires careful development of an equivalent circuit model to describe the experimental data. The most common equivalent circuit for an electrochemical cell includes the solution resistance, the charge-transfer resistance, the double-layer capacitance, and the Warburg impedance associated with mass-transport limitations, as seen in Figure 8. This model was used to generalize the corrosion mechanism for HT9A in LiF. Unfortunately, the behavior of a real system may not conform to a simple single circuit model due to the complexities involved in an evolving interfacial structure of the corroding sample. Additional time constants can be captured by sequentially combining parallel and series impedances until enough complexity has been included to account for these complexities [56].

	Reference Electrode	Open Circuit
Initial frequency(Hz)	100000	100000
Final Frequency(Hz)	0.2	0.2
Points/decade	10	10
AC voltage (mV RMS)	10	10
DC voltage (mV RMS)	0	0
Area (cm^2)	0.7	0.7
Density (g/cm^2)	7.87	7.87
Equivalent weight (g)	27.92	27.92
Time (sec)	20	80
Estimated Z (Ohms)	100	100
Temperature (600±15°C) Or (800±15°C)	Per experiment	Per experiment

Table 2. Parameters for EIS.

Before discussing the details of the EIS model developed to explain the current data, we will begin with a general description of the EIS approach, and some of the more classic EIS models used to explain the electrochemical response of a corroding surface (electrode). The complex impedance is defined in terms of its real and imaginary parts [57]:

$$\hat{Z} = Z_r + jZ_j \qquad \text{(Equation 1)}$$

It is important to recognize that an inverse relationship exists between the complex impedance and the complex admittance that is analogous to the relationship that exists between resistance and conductance:

$$\hat{Y} = \frac{1}{\hat{Z}} \qquad \text{(Equation 2)}$$

The amplitude is defined as the root-mean-square (RMS) of the real and imaginary parts of the complex impedance:

$$|Z(\omega)| = \sqrt{Z_r^2(\omega) + Z_j^2(\omega)} \qquad \text{(Equation 3)}$$

The real and imaginary parts and the amplitude the complex impedance are also related through the phase angle:

$$Z_j = |Z| \sin(\phi)$$ (Equation 4)

$$Z_r = |Z| \cos(\phi)$$ (Equation 5)

The phase angle can therefore be defined in terms of the real and imaginary parts of the complex impedance:

$$\phi = \arcsin\left(\frac{Z_j}{|Z|}\right)$$ (Equation 6)

$$\phi = \arccos\left(\frac{Z_r}{|Z|}\right)$$ (Equation 7)

In the case of series impedances (Z_1) and (Z_2), the total impedance (Z_{total}) is given by:

$$\hat{Z}_{total} = \hat{Z}_1 + \hat{Z}_2$$ (Equation 8)

In the case of parallel impedances (Z_1) and (Z_2), the total impedance (Z_{total}) is given by:

$$\hat{Z}_{total} = \frac{1}{\frac{1}{\hat{Z}_1} + \frac{1}{\hat{Z}_2}}$$ (Equation 9)

In the case of parallel admittances (Y_1) and (Y_2), the total admittance (Y_{total}) is given by:

$$\hat{Y}_{total} = \hat{Y}_1 + \hat{Y}_2$$ (Equation 10)

In the case of series admittances (Y_1) and (Y_2), the total admittance (Y_{total}) is given by:

$$\hat{Y}_{total} = \frac{1}{\frac{1}{\hat{Y}_1} + \frac{1}{\hat{Y}_2}}$$ (Equation 11)

Series-parallel combinations of circuit elements define the overall impedance of the standard three-electrode electrochemical cell used for corrosion testing, and are shown in Figure 8.

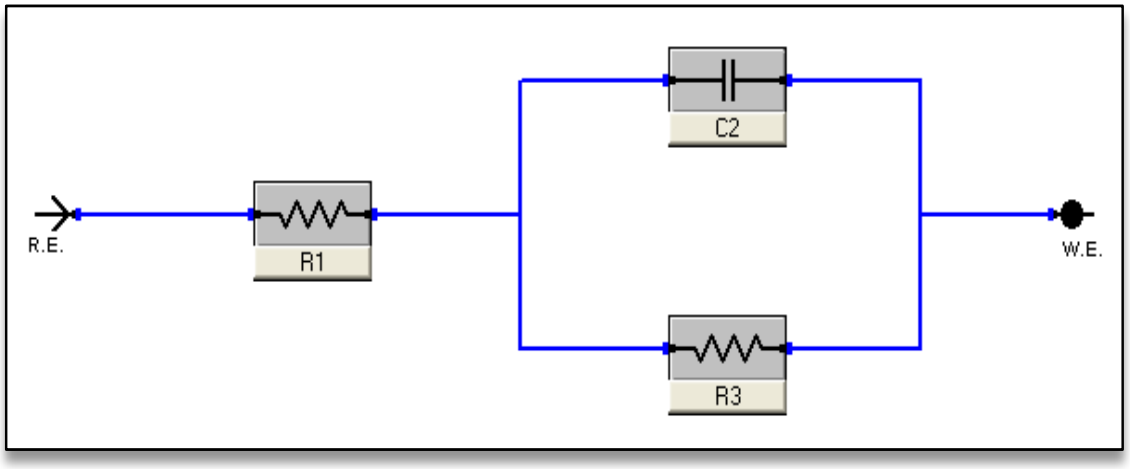

Figure 8. Equivalent circuit model for standard three-electrode electrochemical cell (all equivalent circuit drawings generated with Gamry Electrochemical Analyst Software™).

In this case, R_e represents the resistance of the electrolyte that lies between the reference electrode (Ag/AgCl) and the working electrode (AR or FSP NAB), R_f represents the charge-transfer resistance, which is usually due to oxidation or reduction Faraday-type charge-transfer processes occurring at the interface, and C_{dl} representing the capacitance of the electric double-layer formed at the interface. By first combining R_f and C_{dl} in parallel, and then combining the result with Re in series, the following equations representing the frequency-dependent complex impedance of this simple circuit is derived:

$$\hat{Z} = R_e + \frac{1}{\frac{1}{R_f} + j\omega C_{dl}} \qquad \text{(Equation 12)}$$

$$\hat{Z} = R_e + \frac{R_f}{1 + j\omega R_f C_{dl}} \qquad \text{(Equation 13)}$$

$$\hat{Z} = R_e + \frac{R_f}{1+\left(\omega R_f C_{dl}\right)^2} - j\frac{\omega R_f C_{dl}}{1+\left(\omega R_f C_{dl}\right)^2}$$ (Equation 14)

The well-known frequency responses of equivalent circuit model representing the standard three-electrode electrochemical cell are shown in figures 9 and 10. Figure 9 is the classical Nyquist Plot, where the imaginary part of the complex impedance is plotted against the real part, at various frequencies, thereby yielding the well-known semi-circle. Figure 10 is the corresponding Bode Plot, where both the amplitude of the complex impedance, and the phase angle, are plotted verses frequency, revealing the distinctive peak in phase angle, which occurs at the inflection point in the amplitude.

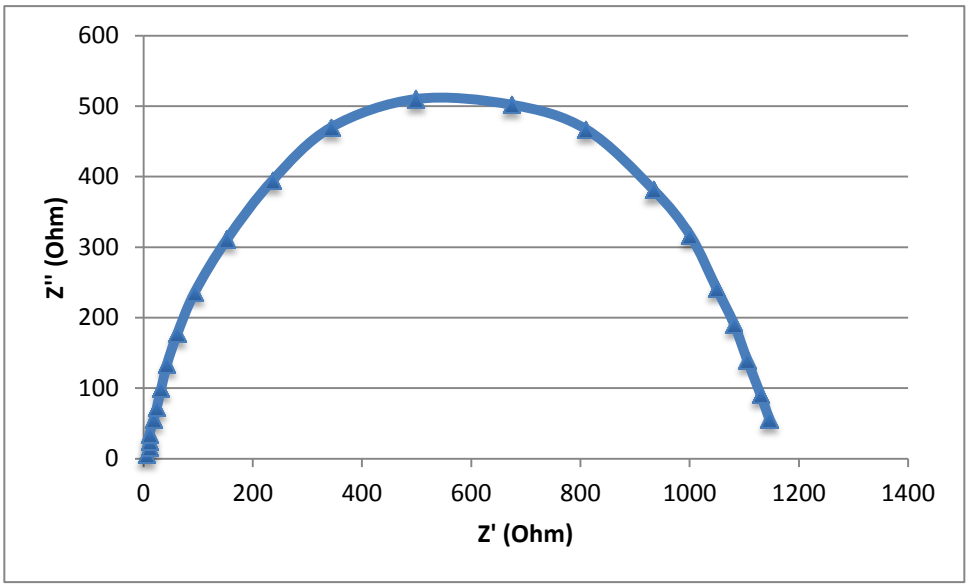

Figure 9. Well-known frequency response of three-electrode cell shown as a Nyquist plot.

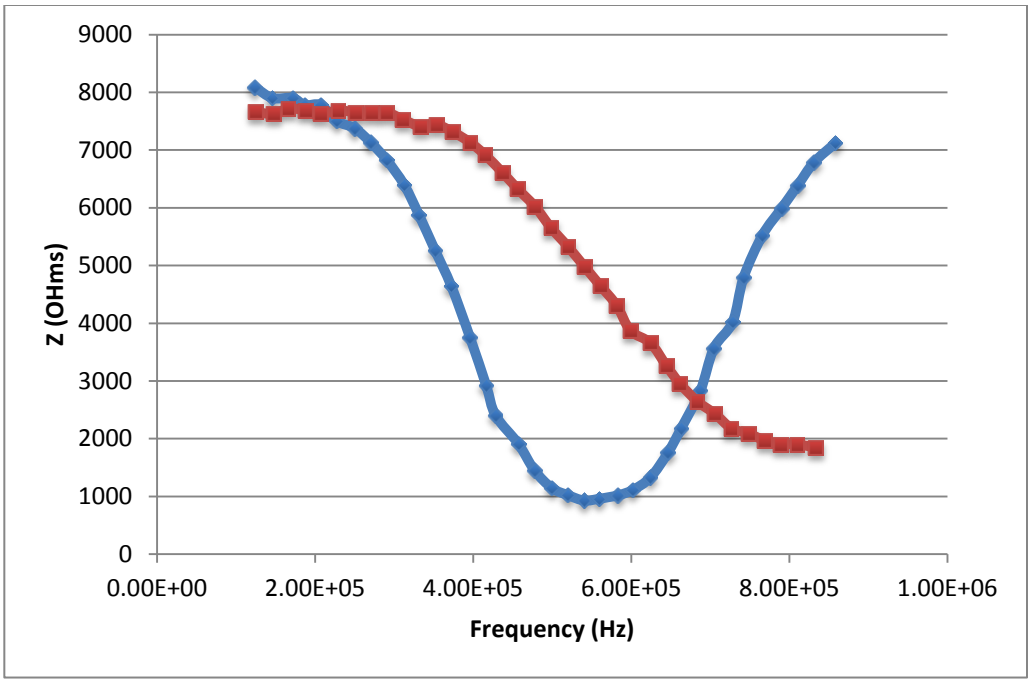

Figure 10. Well-known frequency response of three-electrode cell shown as a Bode plot.

The instantaneous corrosion rates for the various welding parameters of HT9A were measured and analyzed using EIS and GAMRY software. The equivalent circuit model developed to fit the measured impedance spectra is seen in Figure 11.

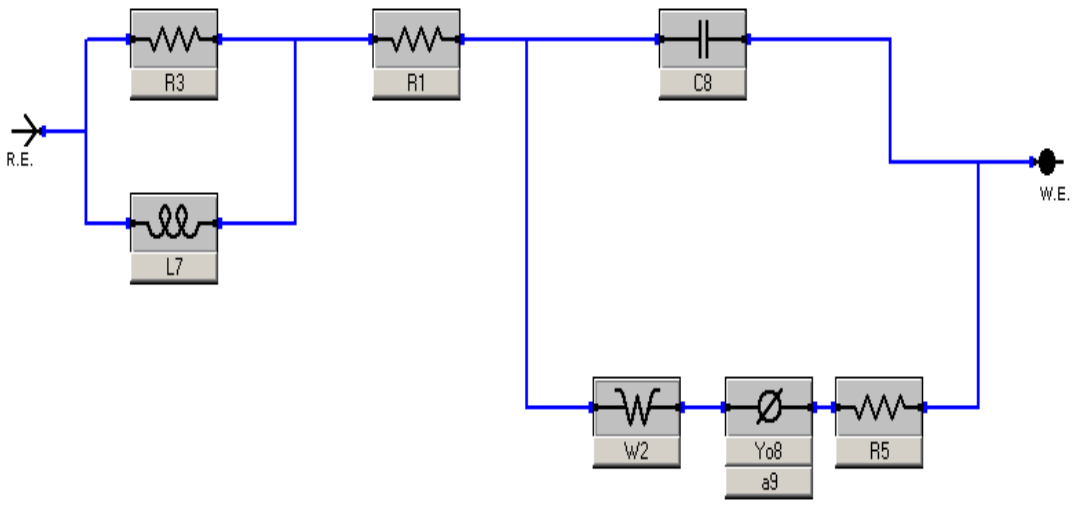

Figure 11. Equivalent circuit model developed to fit impedance spectra.

Components were grouped together based on temperature dependence. R3,L7, R1 and C8 all are weakly temperature correlated, whereas W2, Yo8, a9, and R5 were highly temperature dependent.

The equivalent circuit model, along with the physical meaning of the various equivalent circuit components is shown in Figure 12. Such model includes terms for the impedance of the inductive layer and capacitive layer, electron transfer at the electrode-electrolyte interface, the charge separation at immune metal or oxide-covered metal interfaces, and mass transfer limitations [51].

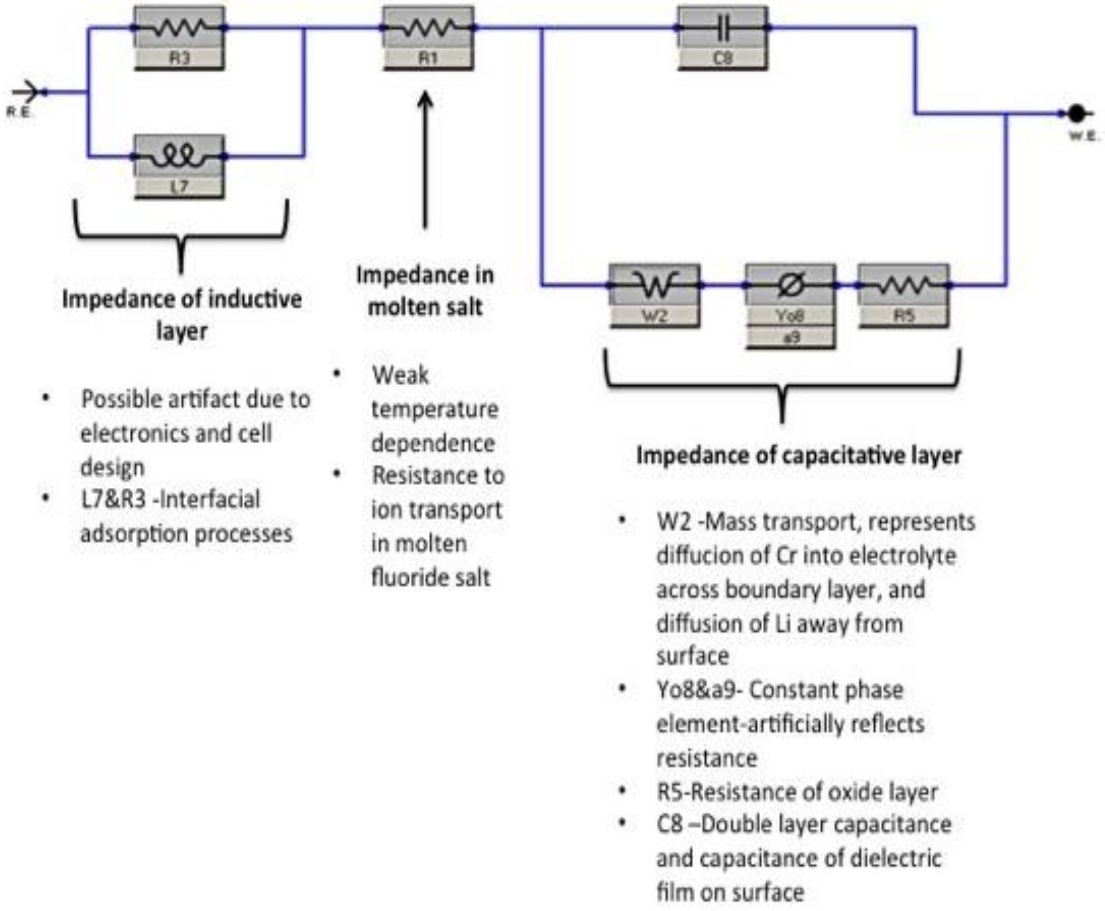

Figure 12. Equivalent circuit model with the physical meaning of the various equivalent circuit components shown.

The model includes terms for ionic conductivity in the molten salt and resistance of the oxide layer and solution. Additional models and equations can be seen in appendices A and B.

3. Material Characterization

a. *Metallography and Optical Microscopy*

Samples of FSW and TIG welded HT9A plate were sectioned and analyzed by scanning electron microscopy (SEM), optical microscopy (OM), electron backscatter diffraction (EBSD), and nanoindentation.

Standard metallographic preparation for cross sections of the weld path were used using 400, 600, and 800 grit silicon carbide abrasive disks, followed by 6µm diamond polishing on nylon cloth with Buehler Matadi 6µm diamond polishing compound. Polishing was finished with 0.05µm colloidal silica on chem-met cloth. Samples were mounted in thermoplastic acrylic-Buehler TransOptic compression mounts for polishing. After polishing, the samples were etched using an acid etchant mixture having the components 20ml H_2O, 20mL HNO_3, 20ml HCl, and 10ml HF. Optical images were taken of all samples using a Nikon Optiphoto 200 microscope. Images were taken at 25x, 200x and 500x magnification.

b. ***Electron Microscopy***

Microstructural examinations were conducted using a Zeiss Neon 40 field emission gun focused ion beam-scanning electron microscope (FIB-SEM). Defined parameters and their values are as seen in Table 3.

Parameter	**Value**
Objective Aperture	60µm
Working Distance	5mm
Dead time percentage	25-45%
Sample time	60min
Amplifier time constant	50µs
Beam voltage	20kV
Beam current	1.32 x 10^{-6} mA

Table 3. SEM Parameters used in samples and experimental EDS.

Line scans and surface and matrix point spectra were used in order to determine the Fe to Cr ratios throughout the metal. Examples of these measurements are seen in Table 4.

Fe (counts)	**Cr (counts)**	**Location of sample**	**Ratio of Cr to Fe**
1848	272	Surface of corrosion layer	14.7
1534	407	In corrosion layer	26.5
2321	845	In the matrix	38

Table 4. HT9-TIG welded, exposed at 800°C in LiF.

c. *Electron Backscatter Diffraction*

Electron backscatter diffraction (EBSD) was employed to measure microstructural quantities such as grain size, micro texture, and recrystallized fraction in the welded microstructures. The Zeiss Neon 40 FIB-SEM was used for these measurements with nominal operating parameters of 20keV beam energy, a 60μm objective aperture, "high current" lens settings, and a specimen tilt of 70°. EBSD data were collected in large area scans; with a step size of 0.5μm, and in small area scans, with a step size of 0.1μm. Typical sizes for large area scans were 250 steps by 500 steps, while small areas scans were typically 100 steps by 100 steps. After the data were collected, it was de-noised using a three-step process: 1.) Rejection of data with a confidence index (CI) less than 0.3, 2.) One iteration of grain dilation, and 3.) One iteration of CI standardization.

4. Nanoindentation

a. *Equipment*

Nanoindentation measurements were performed at Naval Postgraduate School, Monterey on an Agilent G200 Nanoindenter (shown in Figure 13) utilizing a Berkovich diamond indenter tip.

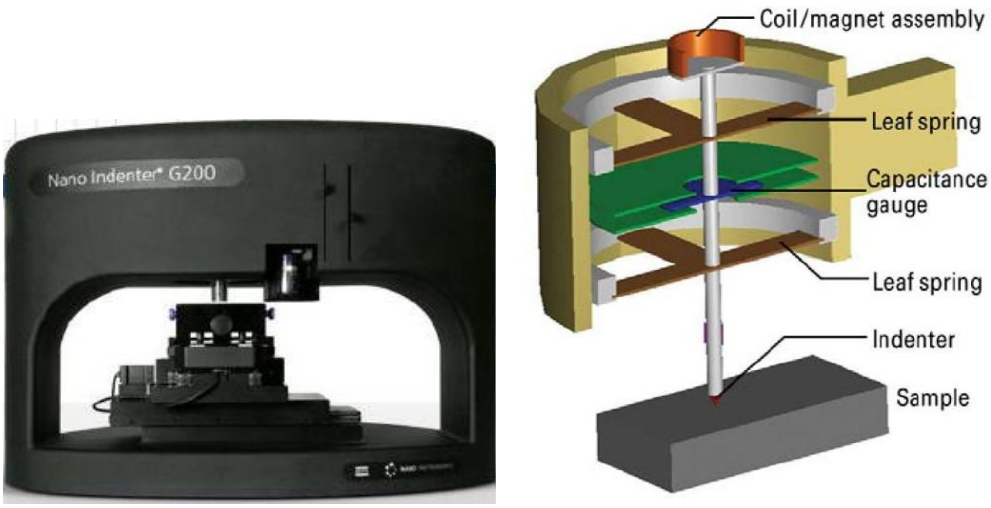

Figure 13. (Left) Agilent G200 Nanoindenter. (Right) Indenter column schematic. (Images from Agilent Inc.)

b. ***Assumptions***

The focus of the nanoindentation phase was to attain representative hardness and elastic modulus data for each parameter used i.e., TIG weld, HT9A base material, and the three-rpm FSW samples. The results were then coupled with EBSD, SEM and microhardness in order to see how the welding parameter affects the hardness and elastic modulus. Nanoindentation was performed in an array of 5x5 indents in various positions with regards to the stir zone. These positions can be seen in Figure 14. Figure 15 shows an example for the indentation pattern.

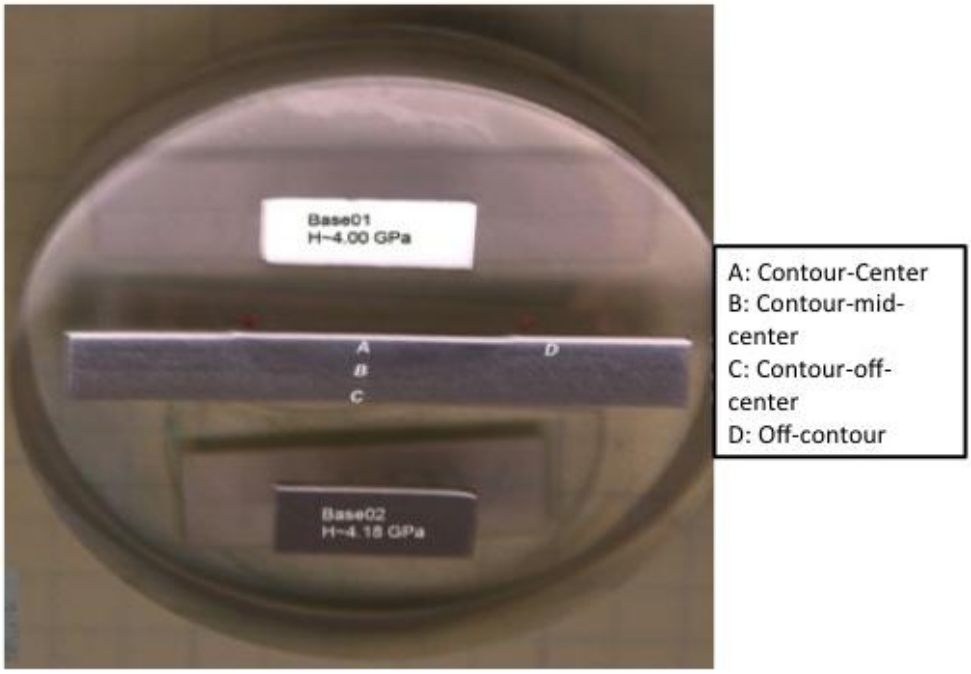

Figure 14. 400 rpm set up for nanoindentation. Right and left hand images show indentation patterns.

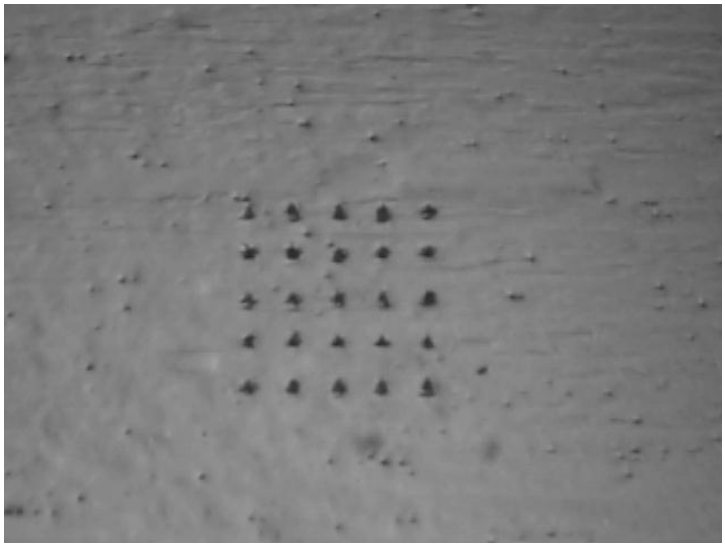

Figure 15. 5x5 indentation pattern for HT9A.

For a Berkovich tip, the width-to-depth ratio for an indentation is approximately 7:1.Based on previous nanoindentation on steels, indentations were spaced

at least twice the width of indentation apart [58]. For these experiments, an indentation depth of 2000nm was chosen with an associated spacing of 50µm between indents.

c. *Experimental Procedure and Parameters*

All specimen indentations were performed using the G200 XP indenter head via Continuous Stiffness Measurement (CSM). For this research, an indentation depth range of 400-2000 nm was used to average values of hardness and modulus. For depths less than 400 nm, the data tended to be noisy. Between 400-2000 nm indentation depth range, the rate of change of properties is minimal, as shown in Figure 16.

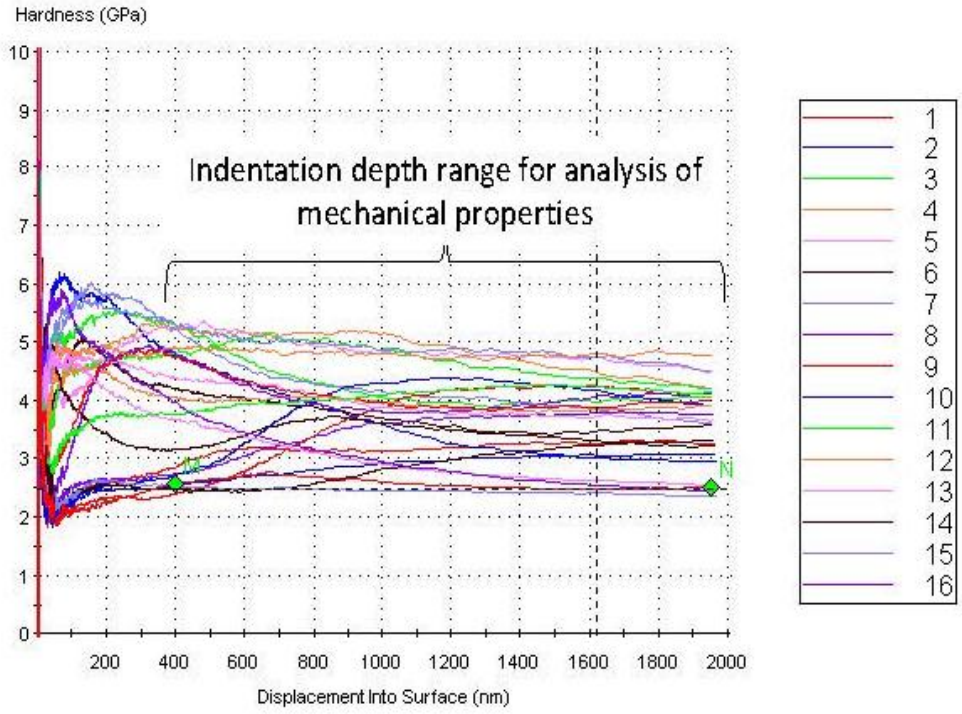

Figure 16. Plot of modulus vs. indentation depth for 9 indentations, HT9A 300 rpm sample.

Prior to indentation, tip calibration was performed on a fused silica sample, in order to determine the indenter tip area function. The remaining input parameters used in the specimen CSM measurements are listed in Table 5:

Parameter	Value
Berkovich tip serial number	TB15658
x-spacing	50 µm
y-spacing	50 µm
Surface approach distance	1000 nm
Surface approach speed	10 nm/s
Surface detect stiffness criteria	200 N/m
Indent depth limit	2000 nm
Poisson's ratio	0.34
Maximum drift rate	0.05 nm/sec
Strain rate target	0.05 1/s
CSM harmonic displacement	2.0 nm
Frequency target	45 Hz
Maximum drift delay time	6hrs

Table 5. CSM method nanoindentation parameters.

5. Microhardness

Microhardness measurements were accomplished using a HVS-1000 microhardness tester with a diamond indenter. Settings of 1 kg-force (9.8N) load, and a dwell time of 15 second were used. According to the American Society for Testing and Materials (ASTM) [59], the minimum distance between indentations in order to avoid interaction between the work-hardened regions and effects of the edge, should be 2.5*d for steel. A value of 0.5mm in between each indentation was used. Calibration of the instrument was verified using a National Institute of Standards and Technology (NIST) certified specimen with a hardness of 729 HV and a certified error of 1.915%. Figure 17 shows the microhardness indentation traverse across the stir zone and into the base metal. The same traverse was used for all three samples.

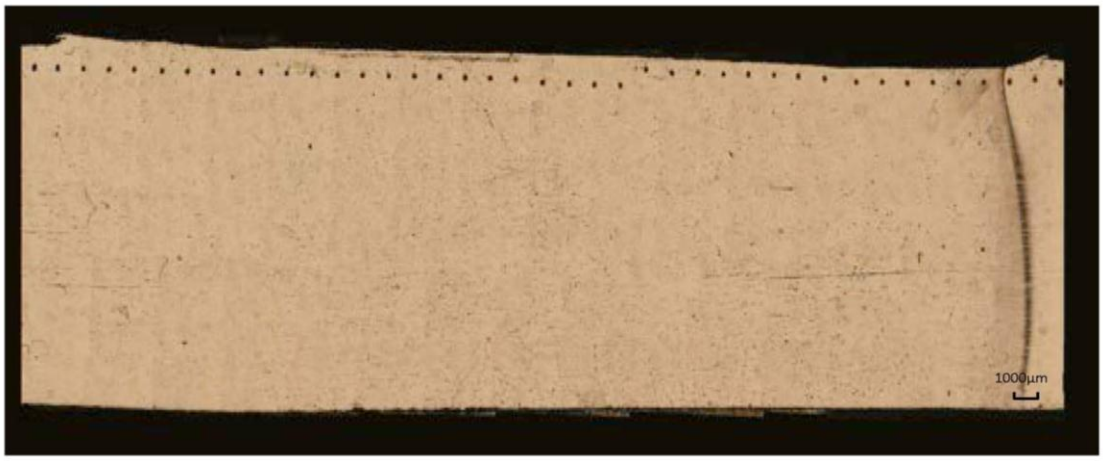

Figure 17. Optical image in order to illustrate stir zone and microhardness indentation traverse.

6. Grain Size

Analyzing the EBSD orientation data performed an accurate measurement of grain size. In order to differentiate the ferritic and martensitic lamella, high angle grain boundaries were added. High angle grain boundaries were set as those with a misorientation greater than 10 degrees. Figure 18 shows how adding high angle grain boundaries help differentiate the two different grain structures. The grain size was determined by taking the average segment length of 50 grains. Size measurements (x and y) of the grains were taken for both ferritic and martensitic grains.

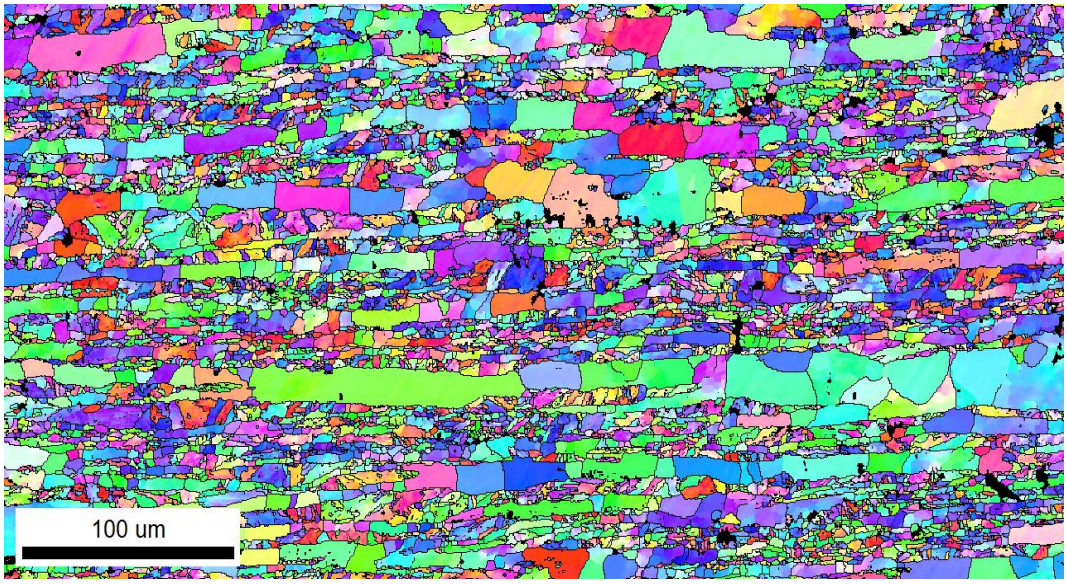

Figure 18. High angle grain boundaries (>10°) clearly differentiate the ferritic-martensitic grains from one another.

III. RESULTS

A. FEASIBILITY OF FRICTION STIR WELDING HT9A

HT9 was friction stir welded without difficulty using the following welding rotational speeds: 300 rpm, 350 rpm and 400 rpm. The weld appearance of the HT9A plate was excellent, i.e., no defect in the tool exit hole, no tunnel defect, a small volume of flash, no undercut, and a smooth surface, i.e., no sticking. Integrity of weld can be seen in Figure 19. Two microhardness traverses can be seen in addition to electropolishing residue. A correlation between the location of the microhardness traverses to the various regions of the weld can be seen in Figure 20.

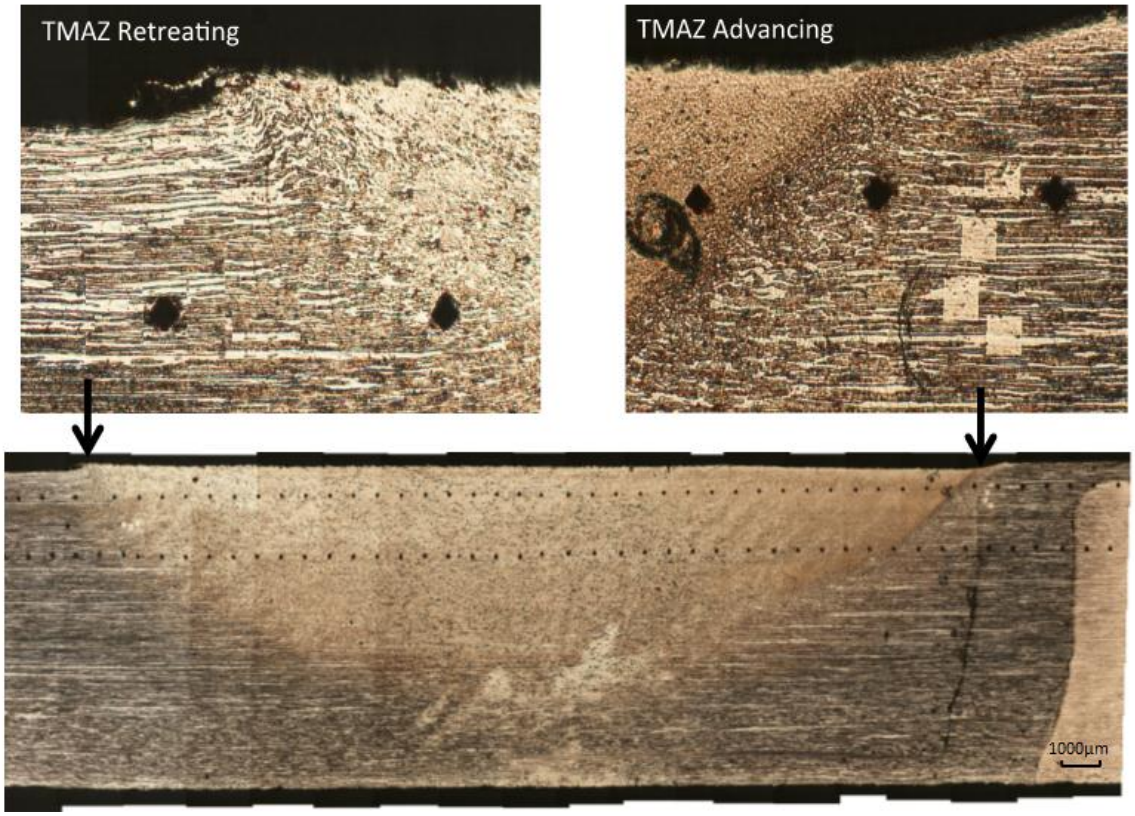

Figure 19. Welded section of 350 rpm FSW HT9. Advancing and retreating sides are clearly depicted.

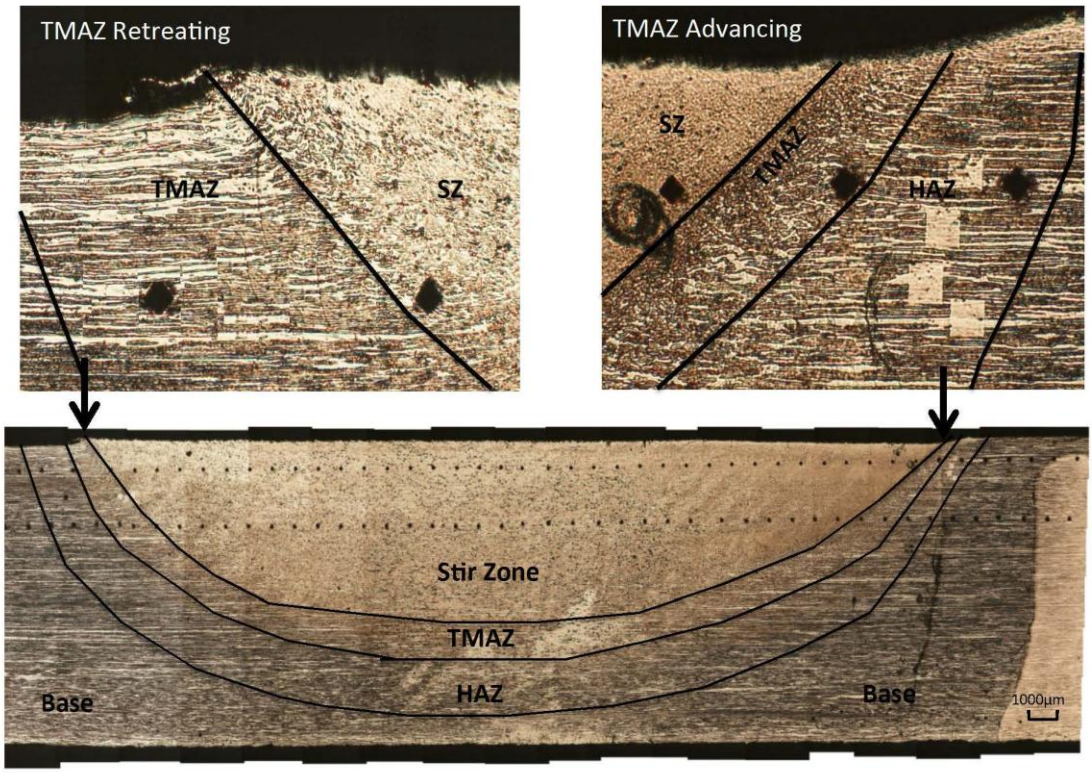

Figure 20. Microstructure of stir zone. All four regions of the weld can be seen: Stir zone (SZ), Thermo-mechanical affected zone (TMAZ), Heat affected zone (HAZ) and the base material.

The well-defined interface between the advancing and retreating sides can be seen in the top two images of Figure 20. The advancing side depicted by the top right image can be differentiated from the retreating side by a marked refinement in grain size in the weld region. This is due to the front of the weld, which rotates and advances simultaneously with the pin, resulting in a highly deformed material, which is sloughed off behind the pin [5]. Alternatively, a much lighter, less deformed material can be seen in the retreating side. Instead of advancing with the rotating tool, the retreating material is moved around to the rear of the tool, filling in gaps between the advancing side materials.

Tool temperature was held relatively constant for all welding parameters, while normal load increased slightly with increasing rotation rate (Figure 21). Temperature

equilibrium (~830°C) was reached after a weld length of 8.9 cm. The temperature remained relatively constant even with reductions in the tool rotation rate from 400 to 300 rpm. It should be noted that this temperature is less than the temperature experienced by the metal during the welding. The z-axis force was low (13.34kN to 17.79kN) for a ferrous alloy, which is likely due to the small tool shoulder diameter (0.44in/1.12cm) [56]. The normal force increased with decreasing tool rotation rate. Forces, both traverse and in the weld direction are illustrated in Figure 22. These forces are very low, due to the shallow weld penetration and small tool shoulder, and indicate the potential for long tool life for this tool design in this material. There is a small increase in force in the tool travel direction with decreasing tool rotation rate. Transverse forces are essentially negligible compared with those in the weld direction [56].

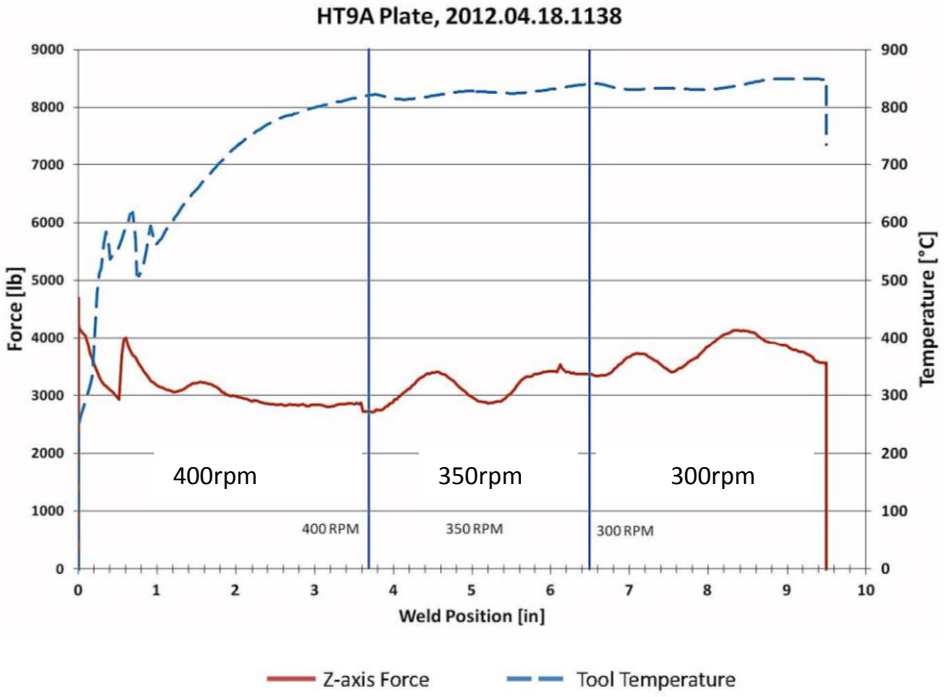

Figure 21. Temperature and normal load in the HT9A friction stir welded plate.

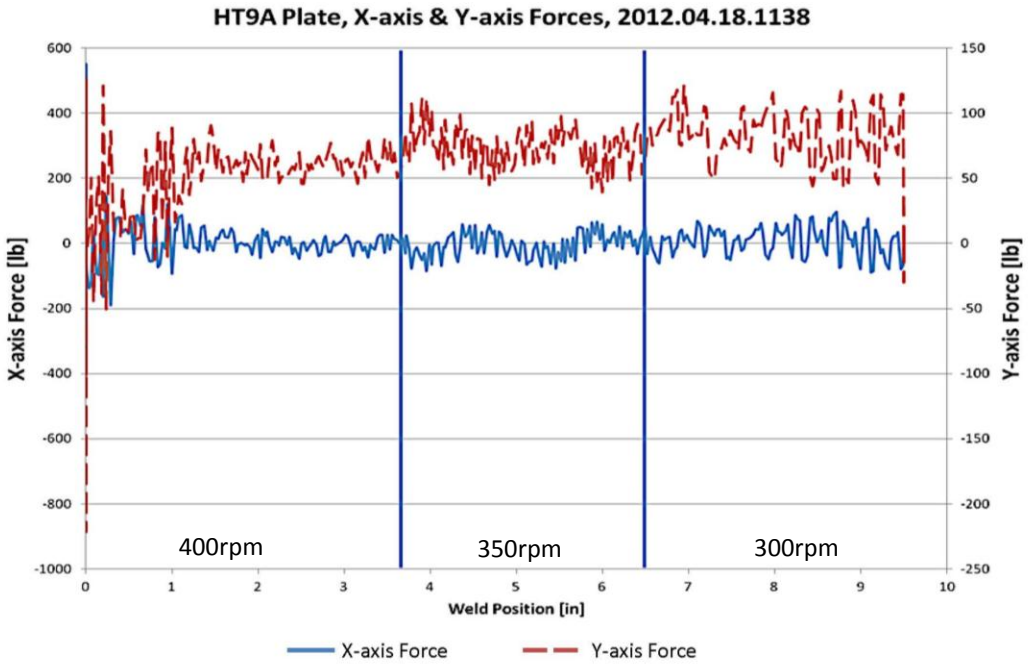

Figure 22. Loads transverse (x-direction, blue) and in the weld direction (y-direction, red) for the friction stir welded HT9A plate.

B. ELECTROCHEMICAL IMPEDANCE SPECTROSCOPY (EIS)

The equivalent circuit model developed to fit the measured impedance spectra was found to adequately fit the impedance data and was conceptually consistent with microstructural observations of the interface. Due to the complexity of this electrical circuit model, the behavior of this system did not conform to a single nyquist or bode plot. In order to obtain a closer fit, and to determine the true response of LiF on HT9A, certain parameters, that showed minimal temperature dependence, were held constant. These values, highlighted in grey, as well as quantitative determinations of additional parameters, can be seen in Table 6. An example of the electrochemical impedance spectroscopy data obtained in both forms: (a) impedance amplitude Z and (b) phase angle φ can be seen in Figure 23. Additional models and comparison of all welding data can be found in Appendix C.

350RPM FSW HT9A			400RPM FSW HT9A		Base Plate HT9A		TIG HT9A	
	600C	**800C**	**600C**	**800C**	**600C**	**800C**	**600C**	**800C**
R1 (Ω)	1.38	1.38	1.38	1.38	1.38	1.38	1.38	1.38
W2 (s*√s)	0.93	0.93	0.93	0.93	0.93	0.93	0.93	0.93
R3 (Ω)	3.29	3.29	3.29	3.29	3.29	3.29	3.29	3.29
L7 (H)	1.91e-6	1.91e-6	1.91e-6	1.91e-6	1.91e-6	1.91e-6	1.91e-6	1.91e-6
R5 (Ohms)	0.04	0.16	0.01	0.11	0.02	0.13	0.02	0.13
Yo8 (s*s^a)	0.11	0.31	0.13	0.27	0.26	0.87	0.20	0.30
a9 (-)	0.60	0.59	0.52	0.56	0.61	0.70	0.57	0.51
C8 (F)	0.01	0.02	0.00	0.01	0.01	0.04	0.01	0.01

Table 6. Quantitative determination of parameters for electrochemical impedance spectroscopy from 0.1 to 100,000 Hz during corrosion of HT9 steel in molten LiF.

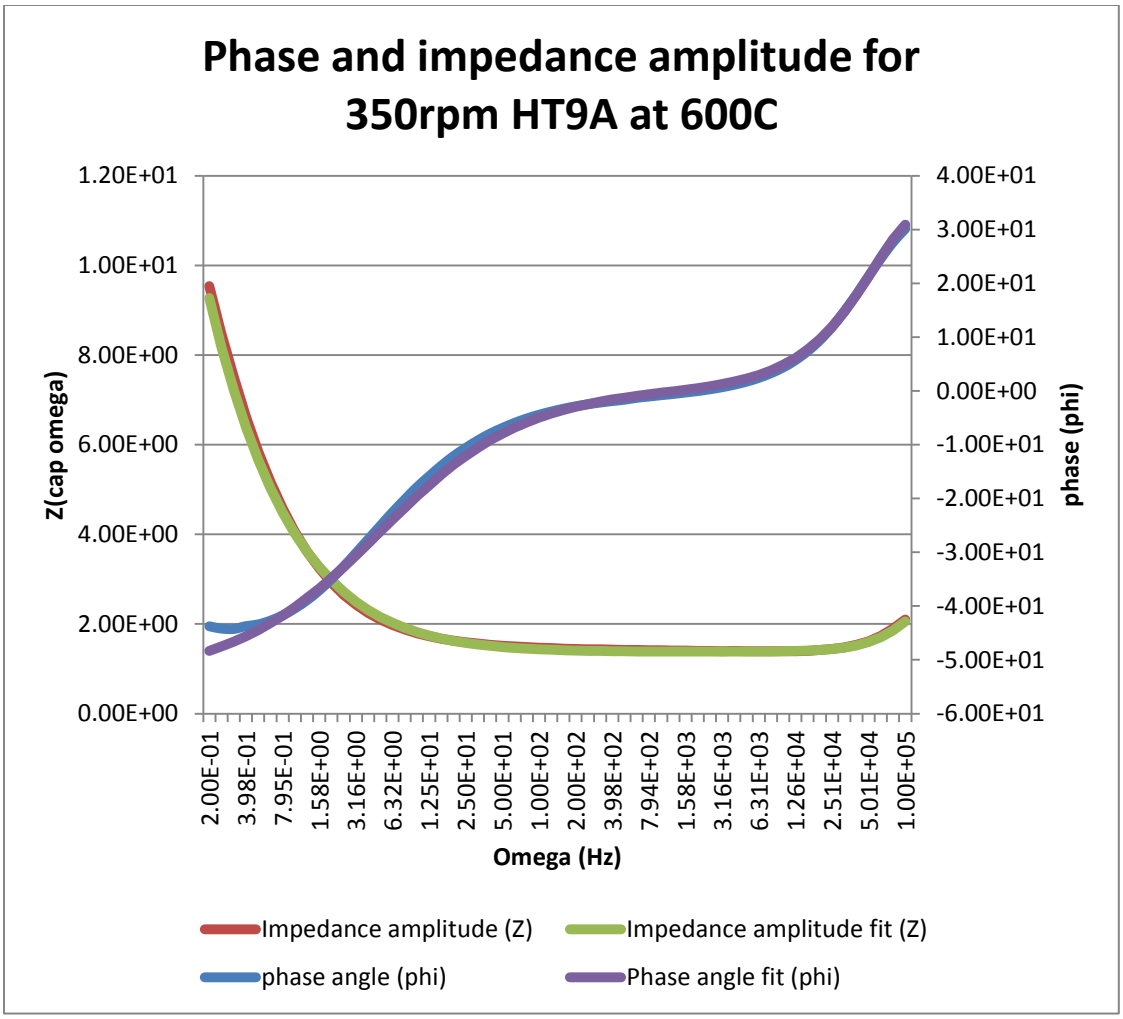

Figure 23. A close fit in both phase and impedance supports my appropriate selection of this model as the most accurate portrayal of the behavior of HT9A in LiF.

With increasing temperature, the polarization resistance increased for all weld parameters (Table 6, and Figure 23). At 600C, the base material is comparable to all welding conditions with the exception of 350 rpm, which performed better than all conditions at both temperatures. At higher temperatures, 350 rpm FSW has the highest polarization resistance and therefore the lowest instantaneous corrosion rate as compared to TIG welding. An increase in polarization resistance can be attributed to the presence of an aluminum oxide layer formed at higher temperatures and confirmed using quantitative EDS. Admittance and capacitance were also seen to increase with

temperature (Figures 24 and 25). This trend is consistent with an increase in polarization resistance, as admittance can artificially reflect resistance. Due to the growing oxide layer at higher temperatures, capacitance would also be expected to increase with temperature. This trend was seen for all samples with the exception of the TIG welded plate. Capacitance and admittance values were similar at lower temperatures (600°C) for all welding parameters, yet base metal experienced much higher levels of both capacitance and admittance at 800°C.

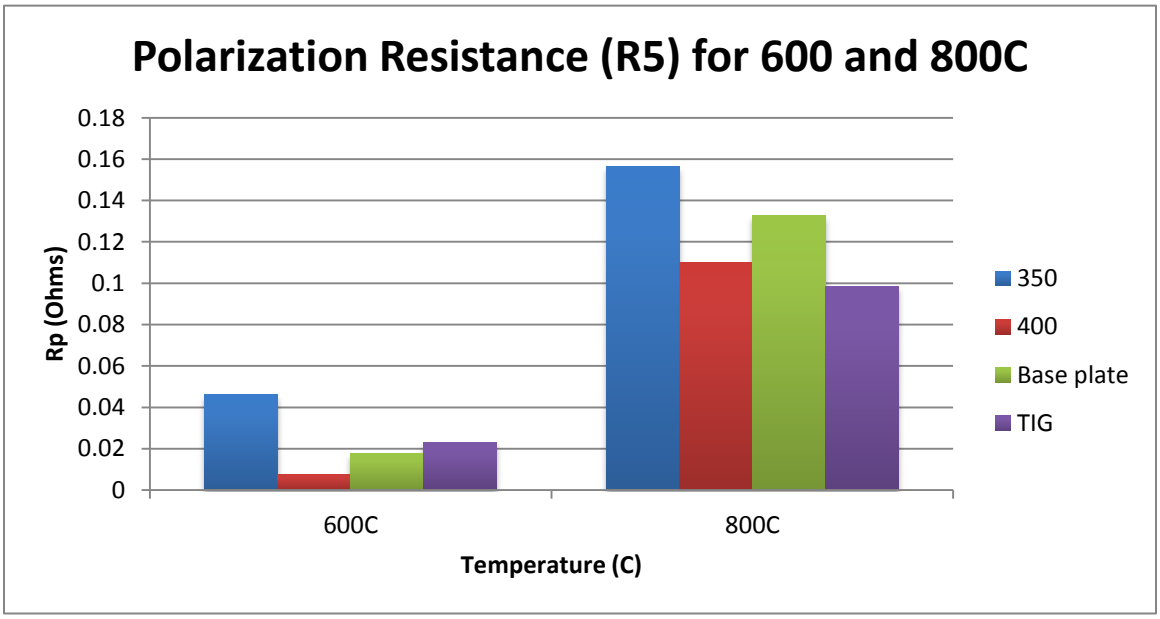

Figure 24. Graphical representation of polarization resistance verse temperature for all four welding parameters.

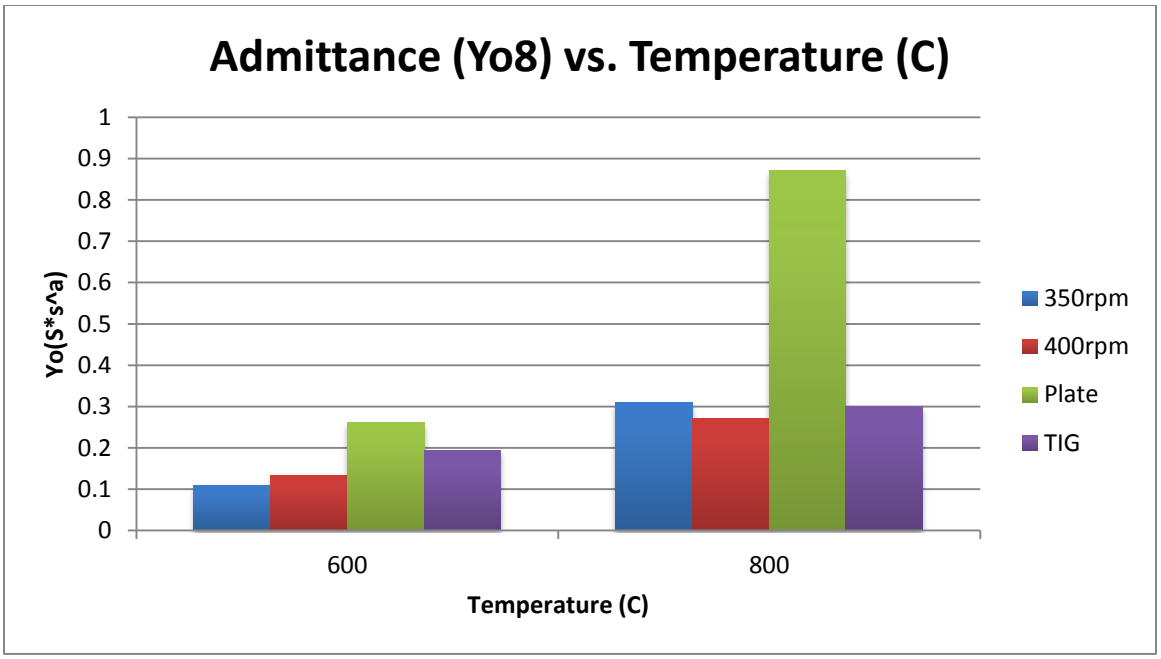

Figure 25. Temperature dependency of circuit element Yo8, reveals results associated with corrosion resistance due to the presence of the aluminum oxide layer formed at higher temperatures.

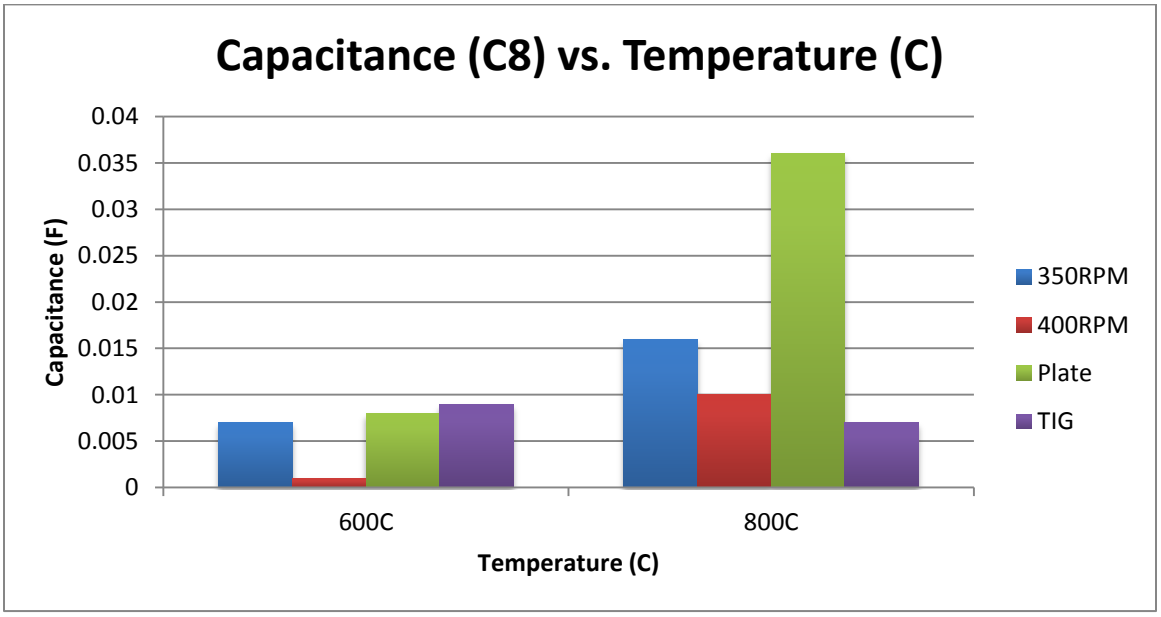

Figure 26. Temperature dependency of circuit element capacitance reveals a growing oxide film at higher temperatures.

See Appendix C for other models investigated.

1. Compositional Variation: Energy Dispersive X-ray spectroscopy

a. *Refractory Element Composition versus Position*

Depletion of chromium and surface deposition of aluminum was observed in all but one molten lithium fluoride exposures. A pair of EDS point spectra taken from the surface (black) and the matrix (red) show the depletion of chromium and the presence of aluminum at the surface (Figure 27). In addition, line scans demonstrated that the chromium depletion, and thus preferential leaching, extended about 5 microns below the surface (Figure 26). The depth of the aluminum signal coincides with the chromium depletion. X-ray maps of these regions further show that the aluminum deposition and chromium depletion was uniform along the surface of the steel that was in contact with the molten lithium fluoride (Figure 28). One tested sample did not show the aluminum surface layer and only limited chromium depletion (Figure 29). Additional x-ray line-scans and maps can be found in Appendix D.

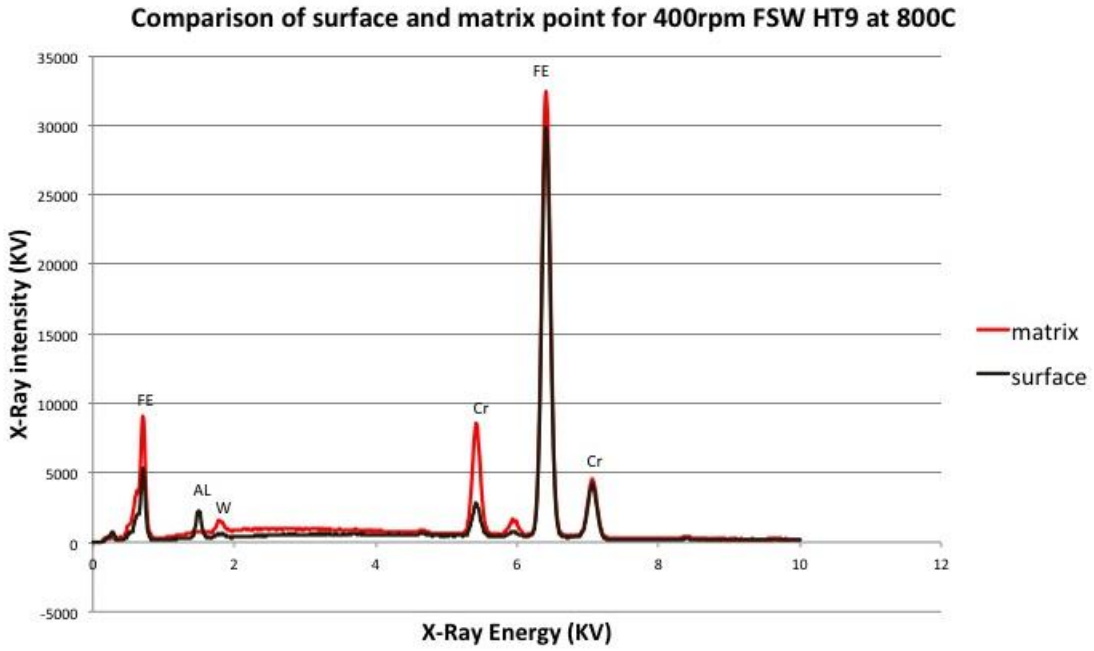

Figure 27. EDS spectra for a matrix and surface point for 400 rpm FSW HT9 at 400°C.

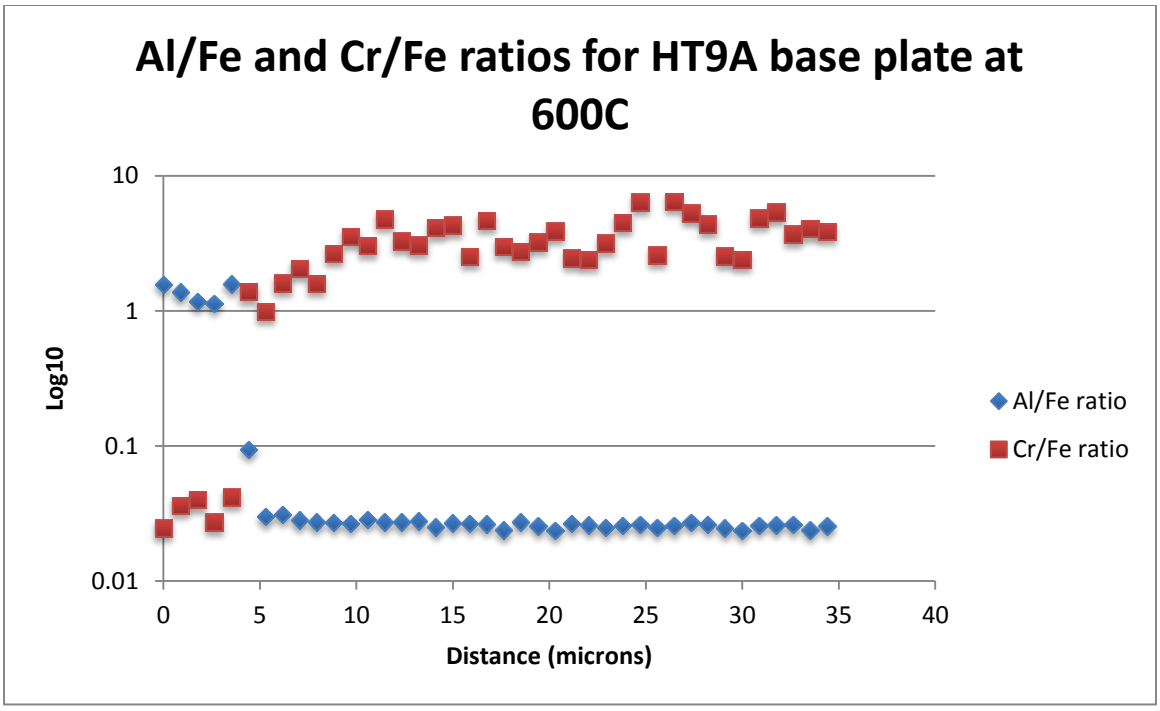

Figure 28. Plots of aluminum and chromium to iron ratios versus position for HT9 base plate at 600°C.

EDS map scan for Base Plate HT9A at 800C

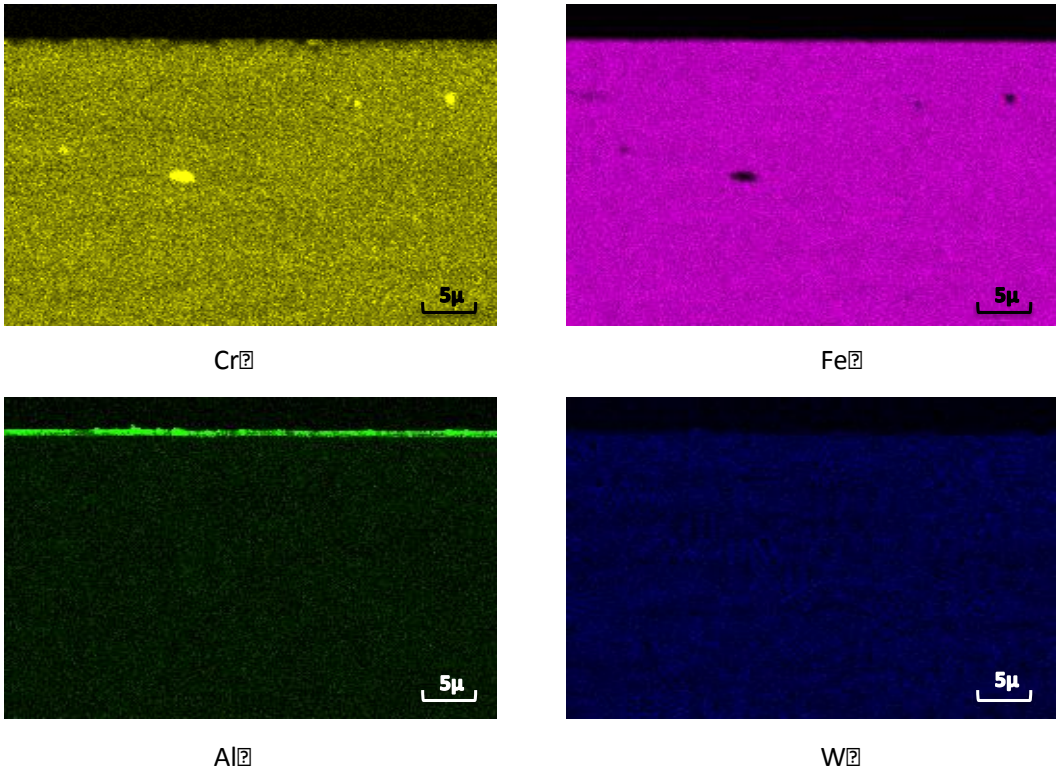

Cr Fe

Al W

Figure 29. EDS map scans of base plate HT9A material at 800°C. Note a visible surface layer of aluminum formed at this temperature.

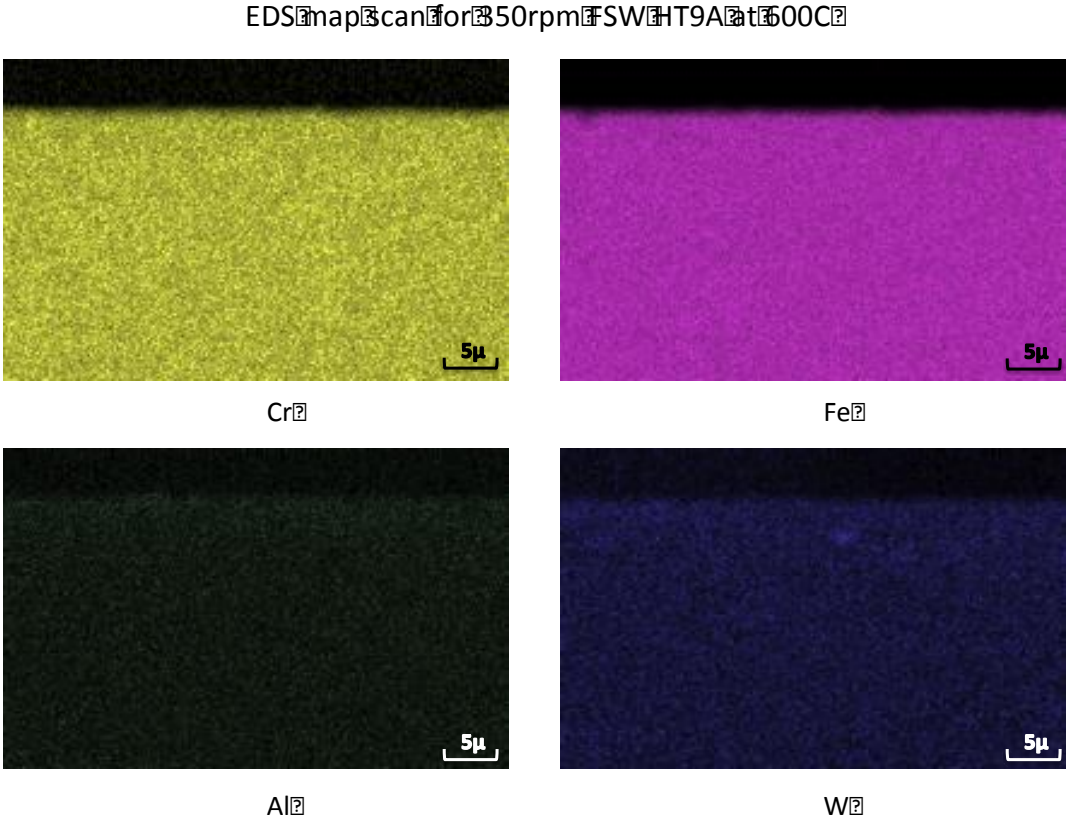

Figure 30. EDS Map scans of 350 rpm FSW HT9 at 600°C. Note no visible surface layer of aluminum formed at this temperature. Chromium depletion still occurred in the first two microns of the surface layer.

C. MICROSTRUCTURAL EVOLUTION

1. Electron Back Scattered Diffraction

EBSD orientation mapping indicated preservation of the ferritic-martensitic microstructure in HT9A steel after friction stir welding. The basic microstructure of the rolled plate HT9A was comprised of long (several hundred micron) ferrite platelets with regions of finer-sized martensite in between platelets (Figure 31A). The ferrite platelets were highly elongated and extended in the transverse direction of the material. The center of the stir zone, for each FSW condition, possessed the same, basic microstructure: ferrite platelets with martensitic regions in between platelets (Figure 31B-D).

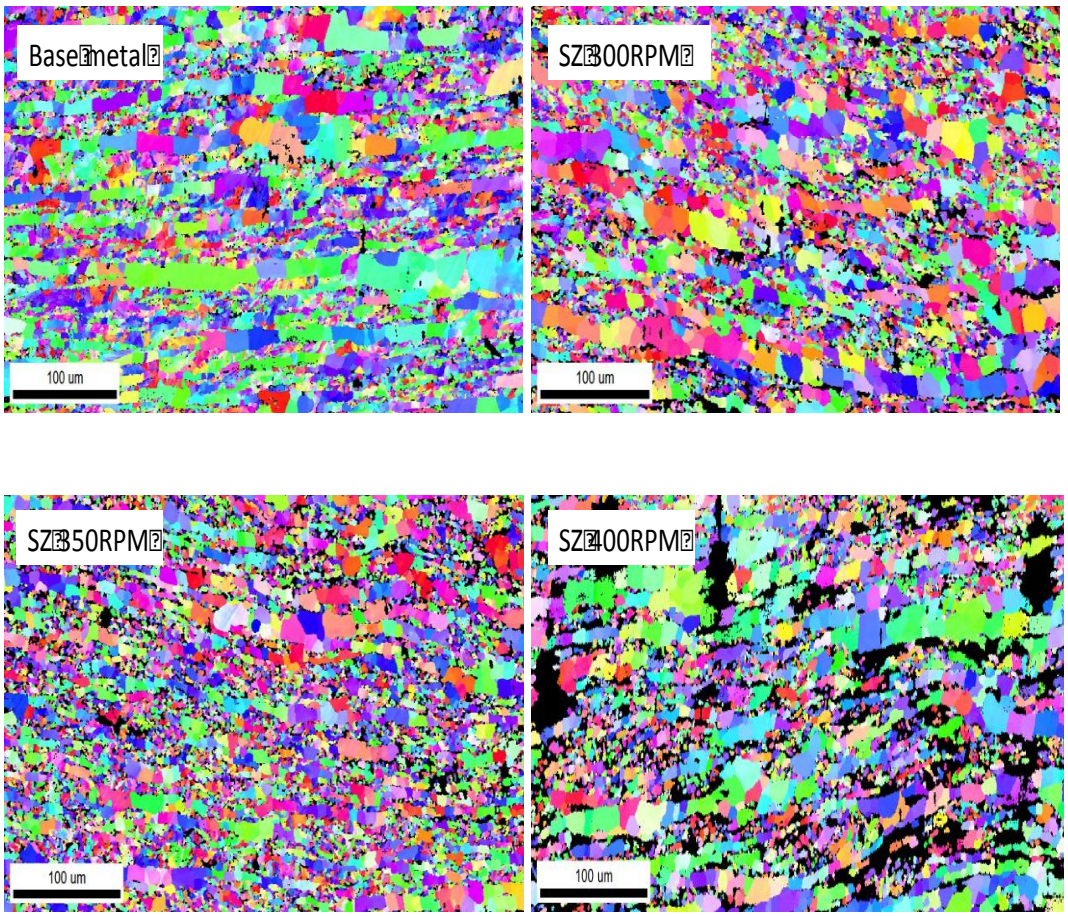

Figure 31. EBSD data taken at the center of the stir zone for 300, 350 and 400 rpm at 0.5-micron step size.

With increasing rotational tool speed, small, but distinct, changes in the stir zone microstructure were observed (Figures 32). In the base plate, the high angle grain boundaries (misorientation greater than 10°) were all nearly perpendicular to the long axis of the platelets. As the rotational speed increased, the grain boundaries were observed to no longer be perpendicular to the platelet axis. For the 400 rpm condition, a number of triple junctions were observed inside of ferrite platelets with angles approaching 120° (Figure 32 D). In addition, the lenticular shape of the martensitic grains observed in the base plate (Figure 32A), evolved towards a more equiaxed shape as the rotation tool speed increased. The ferrite grain size within the platelets was reduced significantly after FSW (Table 7): from 27μm in the base plate to 14μm in the

stir zone of the 300 rpm condition. The ferrite grain size increased slightly with increasing rotational tool speed to 20μm for the 400 rpm condition. The FSW process for any of the conditions explored did not significantly alter the martensite grain size. In all cases, the martensitic grain size was approximately 1μm (Table 7).

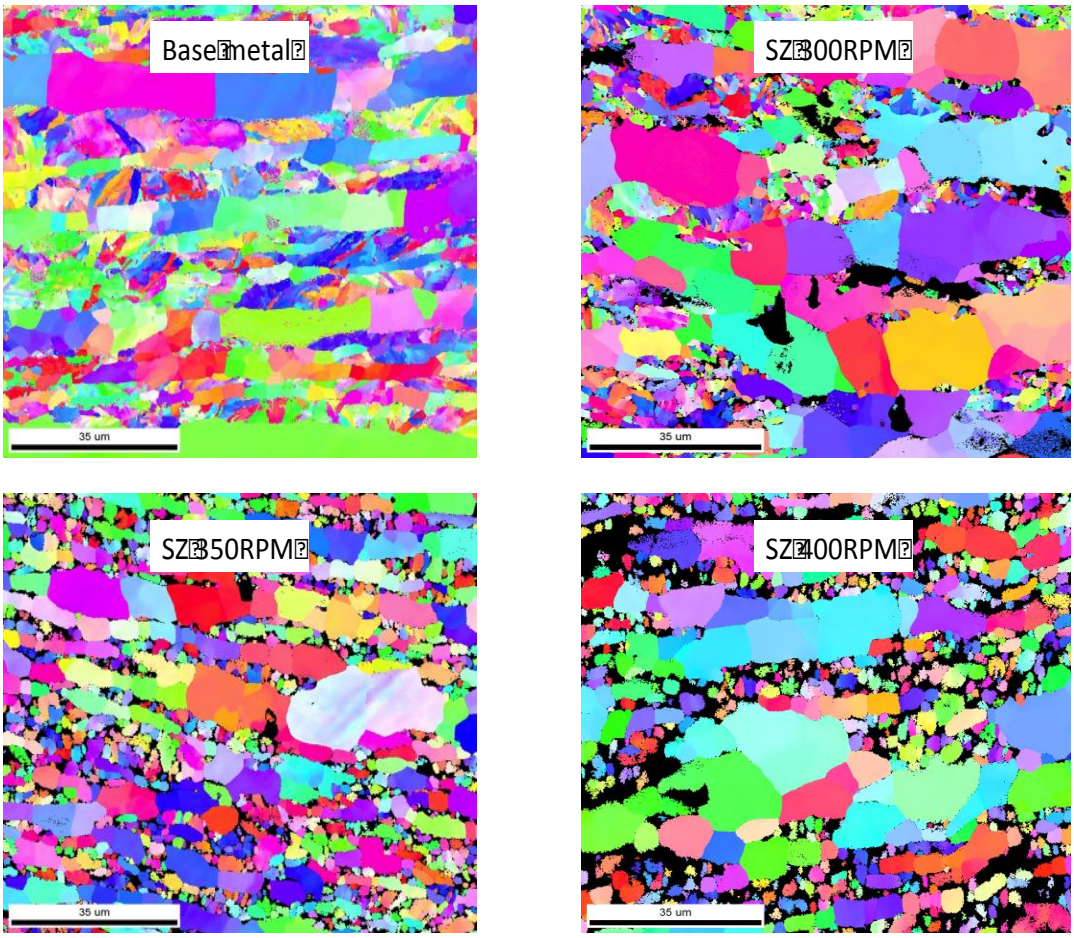

Figure 32. EBSD data taken at the center of the stir zone for 300, 350 and 400 rpm at 0.1 step size.

	Ferrite Grains (μm)		Ratio (X/Y)	Martensite Grains (μm)		Ratio (X/Y)
	X	Y		X	Y	
Base Plate	27.3±6.9	11.83 ±3	2.3	2.3±1.1	2.2±0.8	1.0
300rpm CSZ	13.9±5.5	11.3±6.6	1.2	2.7±1.1	2.4±0.7	1.1
350rpm CSZ	17.3±5.3	10.0±2.9	1.7	2.7±0.8	2.4±1.2	1.1
400rpm CSZ	20.5±8.0	12.2±3.5	1.7	3.6±0.9	3.3±0.6	1.1
300rpm TMAZ advancing	26.9±8.9	8.3±3.6	3.2	3.3±1.3	2.3±0.7	1.5
350rpm TMAZ advancing	21.2±7.2	7.3±3.4	2.9	3.2±1.1	2.3±0.6	1.4
400rpm TMAZ advancing	19.4±5.3	7.9±4.1	2.5	3.00±1.2	2.3±0.7	1.3
300rpm TMAZ retreating	48.4±8.6	8.4±2.8	5.8	3.9±1.5	2.4±0.8	1.6
350rpm TMAZ retreating	23.4±7.4	12.9±4.6	1.8	2.8±0.9	3.7±4.8	0.8
400rpm TMAZ retreating	38.4±7.5	8.9±5.7	4.3	2.8±1.0	2.5±0.8	1.1

Table 7. Grain size data for both ferritic and martensitic grains.

The microstructure of the thermo-mechanically affected zone (TMAZ) for each weld resembled the microstructure of the base plate material even more closely. This similarity to base microstructure was particularly strong for the retreating side of the weld (Figures 33-35). However, both the advancing and retreating sides maintained grain boundaries perpendicular to the platelet axis. The lenticular shape of the martensitic grains observed in the base plate evolved in both the advancing and retreating sides towards a more equiaxed shape. While the martensitic grain size remained the same (approximately 1μm) for both the advancing and retreating sides, a higher percentage of martensitic grains appear to be present in the advancing sides for all welding parameters.

The ferrite grain size within the platelets was significantly reduced in length in the advancing side as compared to the retreating side (Table 7): from 26.9μm to 48.4 μm for the 300 rpm condition, 21.2 μm to 23.4 μm for the 350 rpm condition, and 19.4 μm to 38.4 μm for the 400 rpm condition. A correlation in decrease in ferritic grain size with increasing heat input was observed.

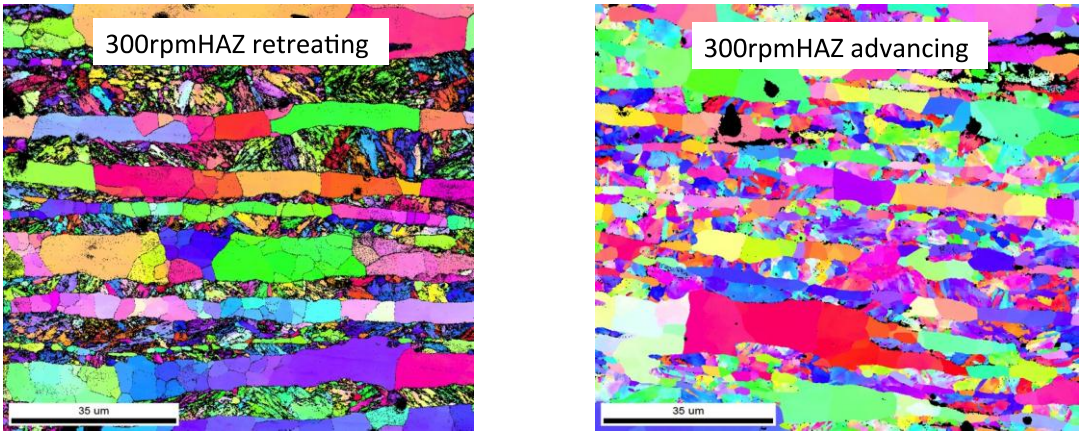

Figure 33. Comparison of advancing and retreating sides for 300 rpm FSW HT9 taken at 0.1-step size.

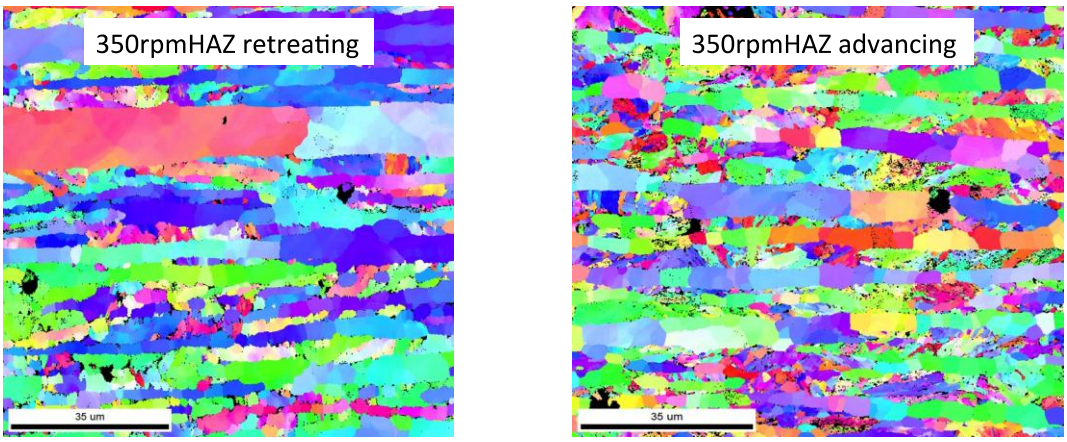

Figure 34. Comparison of advancing and retreating sides for 350 rpm FSW HT9 taken at 0.1-step size.

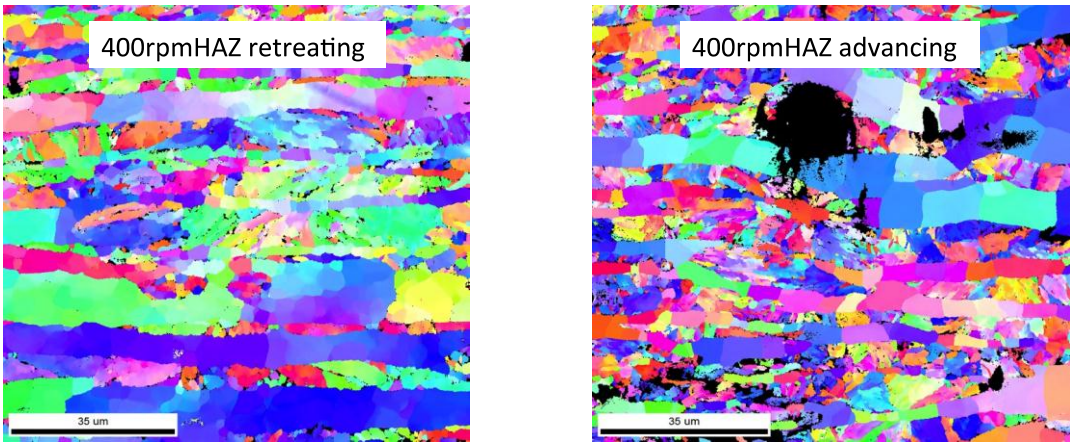

Figure 35. Comparison of advancing and retreating sides for 400 rpm FSW HT9 taken at 0.1-step size.

a. *Micro-Texture Evolution*

The micro-texture after FSW maintained the {hkl}<111>- partial fiber texture observed in the base plate, albeit at a weaker intensity for all welding conditions. The intensity maximum between pole figures from FSW stir zones was not meaningfully different. The pole figures represent data from both the ferrite platelets and the martensitic grains; however, there were many more martensitic grains, so they represented most of the intensity observed in the pole figures.

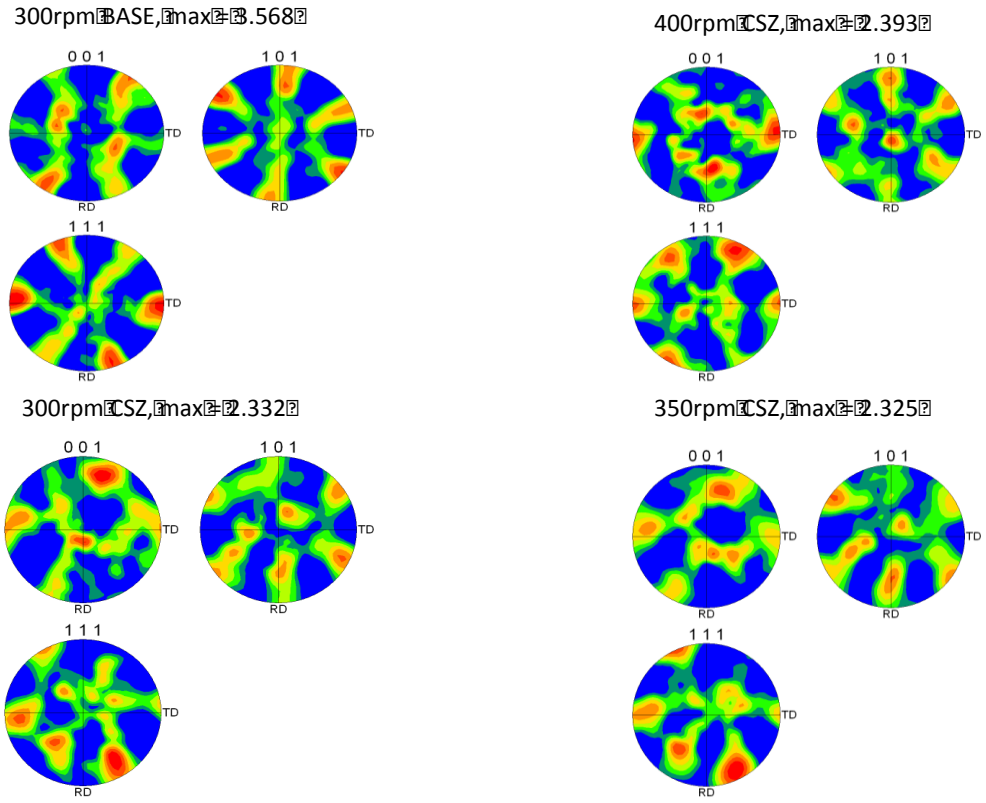

Figure 36. EBSD pole figures from stir zones of friction stir welds (normal to welding direction, transverse direction to the right).

The micro-texture of the TMAZ regions did change significantly from both the base plate and the stir zones (Figure 37). The differences were strongly affected by the tool rotation speed. On the retreating side (RS) of the TMAZ, the same {hkl}<111> partial fiber was observed as in the base plate material for the 300 rpm conditions, but with lower intensity. The pole figure for the 400 rpm condition on the RS, suggests this same texture, but with a small degree of rotation and significant scatter. Interestingly, the pole figure for the 350 rpm condition on the RS showed both a strengthening of the texture and a 45 degree rotation from that observed in the base plate and the stir zone. The textures on the advancing side (AS) of the welds were weakened to the point of being insignificant for the 300 rpm and 400 rpm conditions (Figure 38). The texture for

the 350 rpm condition on the AS; however, shows the same strengthening and 45 degree rotation observed in the pole figure from the RS.

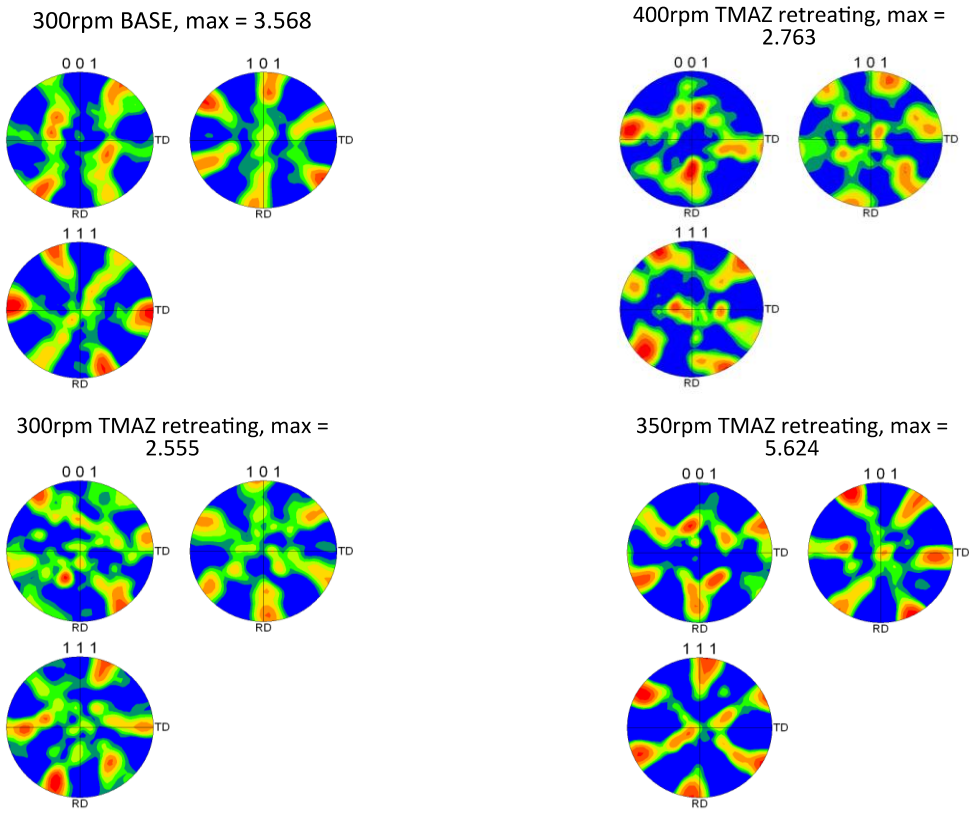

Figure 37. EBSD pole figures from the retreating side of the TMAZ for friction stir welds (normal to welding direction, transverse direction to the right).

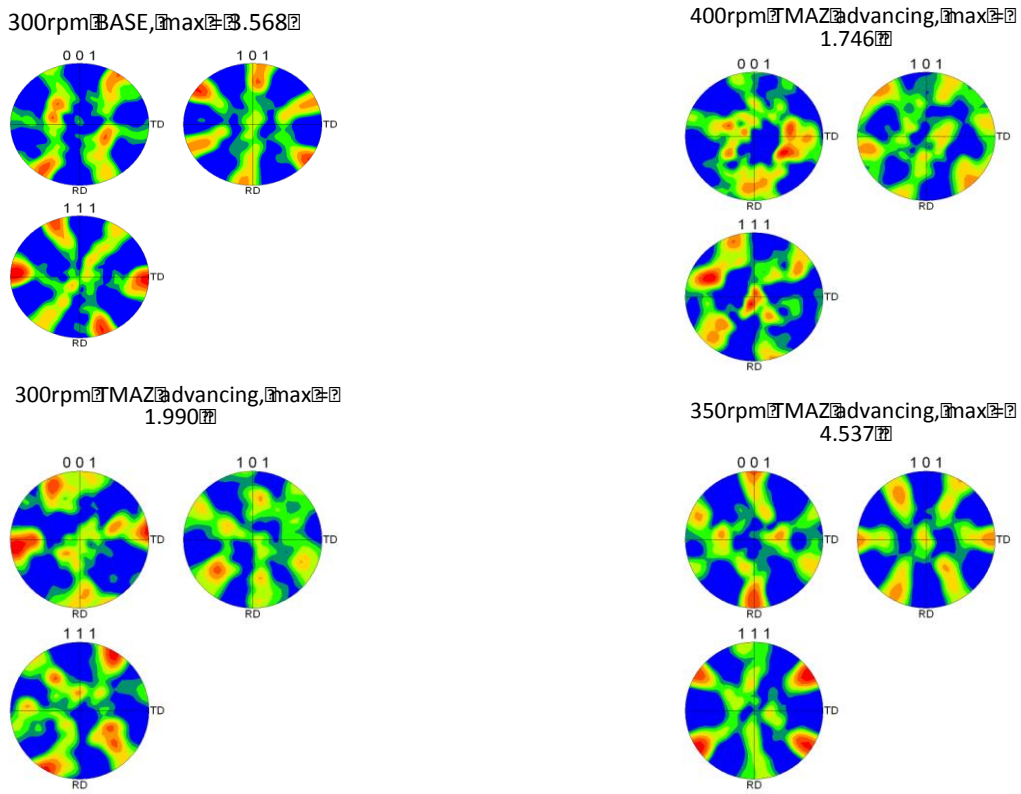

Figure 38. EBSD pole figures from the advancing side of the TMAZ for friction stir welds (normal to welding direction, transverse direction to the right).

D. NANOINDENTATION AND MICROHARDNESS RESULTS

Both microhardness and nanoindentation tests indicated a small decrease in the hardness of the welded material. Both nanoindentation and Vickers microhardness showed a 10-15% softening in the stir zone, which increased with increasing heat input. Nanoindentation on the 350 rpm sample suggested that the TMAZ was slightly harder than the center of the stir zone (Table 9). Similar trends were observed in 300 rpm and 400 rpm welds, and can be seen in appendix E. In contrast, the heat affected zone (HAZ) for all welds displayed a significant drop in hardness. This trend was fairly symmetric for both the advancing and retreating sides of the weld with the exception of the advancing side for the 400 rpm weld (Figure 38). The drop in hardness in the stir zone and the HAZ was more pronounced in the profile taken 3mm below the surface.

Welding Condition	Hardness (GPa)	Modulus of Elasticity	Hardness (HV)
FSW 300rpm (CSZ)	3.4±0.5	216.9±8.1	275±5.3
FSW 350rpm (CSZ)	3.3±0.3	215.2±5.4	270±5.2
FSW 400rpm (CSZ)	3.2±0.3	215.0±4.5	265±5.1
FSW 300rpm (Base)	3.9±0.8	225.2 ± 7.6	283±5.4

Table 8. Summary of results for nanoindentation and microhardness: a comparison of hardness values for the center of the stir zone compared to the base metal.

350 rpm Parameter	Hardness (GPa)	Modulus of Elasticity (GPa)
CSZ	3.5±0.7	215.2±5.4
TMAZ	3.6±0.6	217.6±5.3
HAZ	3.2±0.5	219.3±4.8
Base	3.9±0.4	223.3±4.6

Table 9. Nanoindentation hardness and modulus of elasticity data indicates a softening effect in the CSZ, followed by a more severe softening in the HAZ, and a regain of hardness in the base material.

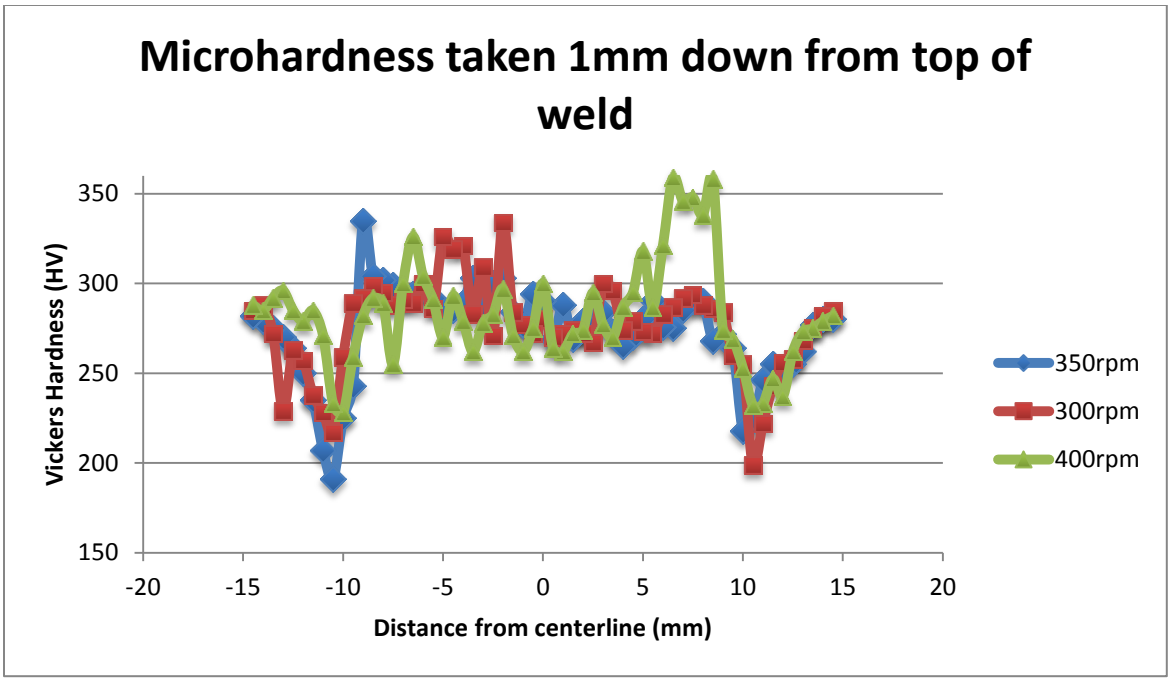

Figure 39. Microhardness traverse taken 1 mm down from the top of the weld plate.

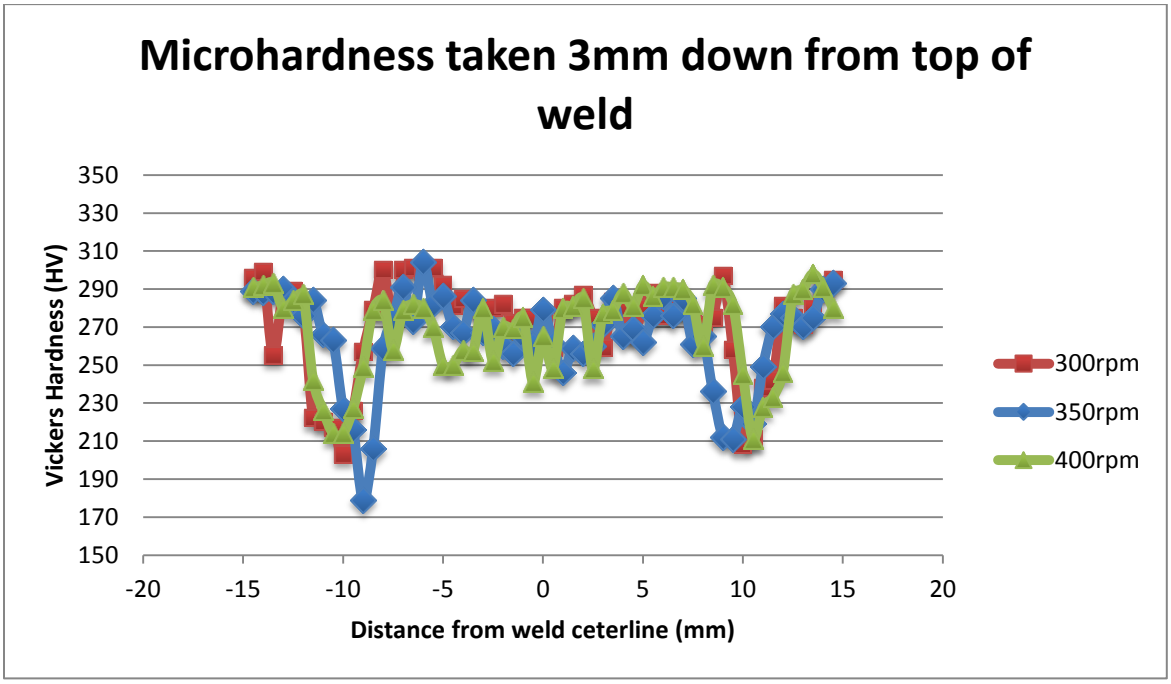

Figure 40. Microhardness traverse taken 3 mm down from the top of the weld plate.

IV. DISCUSSION

A. FEASIBILITY OF FSW HT9

Obtaining a sound, defect-free weld using friction stir welding is important in maintaining maximum material properties. Process parameters such as travel speed, forge force, and rotational speed are important in controlling the thermal energy in the weld zone therefore minimizing weld zone defects [60]. Though various welding parameters exist, only the heat input was varied in this study. High quality welds were obtained for all three-heat inputs (300 rpm, 350 rpm and 400 rpm). Additionally, the overall mechanical response of HT9A demonstrates that the use of these welding parameters is reasonable, resulting in relatively minimal change to the original performance of the material. The transverse speed, although not varied in this study, also plays an important role in the applied heat input, directly affecting the overall quality of the weld. While no systematic review of defects versus FSW parameters exists for steels, weld defects have been seen to occur for low heat input ratios (less than 100) [41]. Biswas further discusses the importance of obtaining the correct heat input ratio in order to avoid weld defects and obtain high quality mechanical properties in his paper involving aluminum alloys [61]. While the relative order and correlation between transverse speed and rotation rate resulted in a suitable relationship in this study, the concept of a relationship between these two parameters in order to obtain successful weld consolidation is an important consideration.

B. PRESERVATION AND EVOLUTION OF MICROSTRUCTURE-DURING FSW

The preservation of the ferritic-martensitic microstructure after FSW can be understood in terms of the appropriate phase diagrams for the HT9A system. While no specific, detailed phase diagram exists for HT9A, a great deal of thermodynamic and phase transformation information exists for related steels. Again, the nominal composition for HT9A steel is Fe-12Cr-1.94W-0.05C. In essence, HT9A is a high Cr, low carbon steel with a refractory addition that is a ferrite stabilizer. The Fe-Cr binary

phase diagram (Figure 41) would suggest the HT9A would cycle between a single-phase alpha ferrite regime and a two-phase, $\alpha + \gamma$ regime before, during, and after welding. The presence of martensite is, of course, dictated by cooling rates and is not indicated on the phase diagram itself. The Fe-Cr binary phase diagram predicts that at a composition of 12wt%Cr, and a hot-working temperature of approximately 1100°C a two-phase region ($\alpha + \gamma$) would be present during welding, particularly in the stir zone. Upon cooling, the γ phase would transform back into martensite provided that the cooling rate is sufficiently high. A ferritic-martensitic structure would therefore be expected as observed in the microstructural analysis of friction stir welded HT9A. The presence of tungsten in HT9A does not seem likely to affect this cycle of phase transformations given the low of carbon in the alloy (Figure 42). Lakshminarayanan makes this same observation for FSW of a 409M ferritic steel. Although their work began with ferritic steel, martensite was observed after FSW. They show a similar γ-loop in the Fe-Cr binary phase diagram (at a carbon content of 0.03 weight percent) as pictured in Figure 41 [37]. For these reasons, it seems that HT9A exists as a two phase steel before, during and after friction stir welding, with the martensite of the base material transforming to $\gamma\ phase$ and then back to martensite, while the α ferrite region remains throughout the process (as suggested in Figure 43).

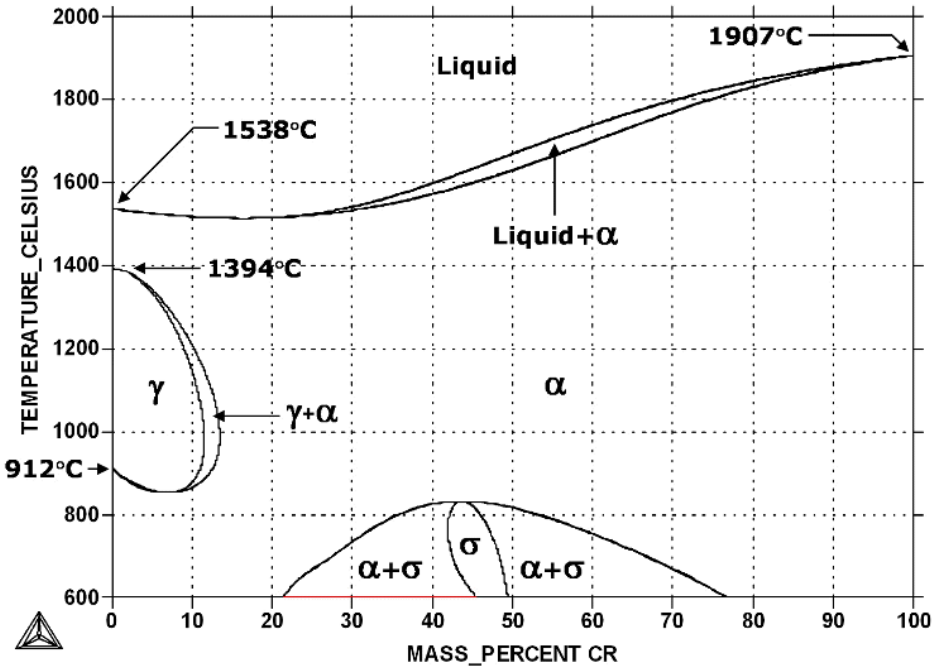

Figure 41. Phase Diagram for Fe-Cr [62]. HT9A falls in a two phase $\alpha + \gamma$ regime.

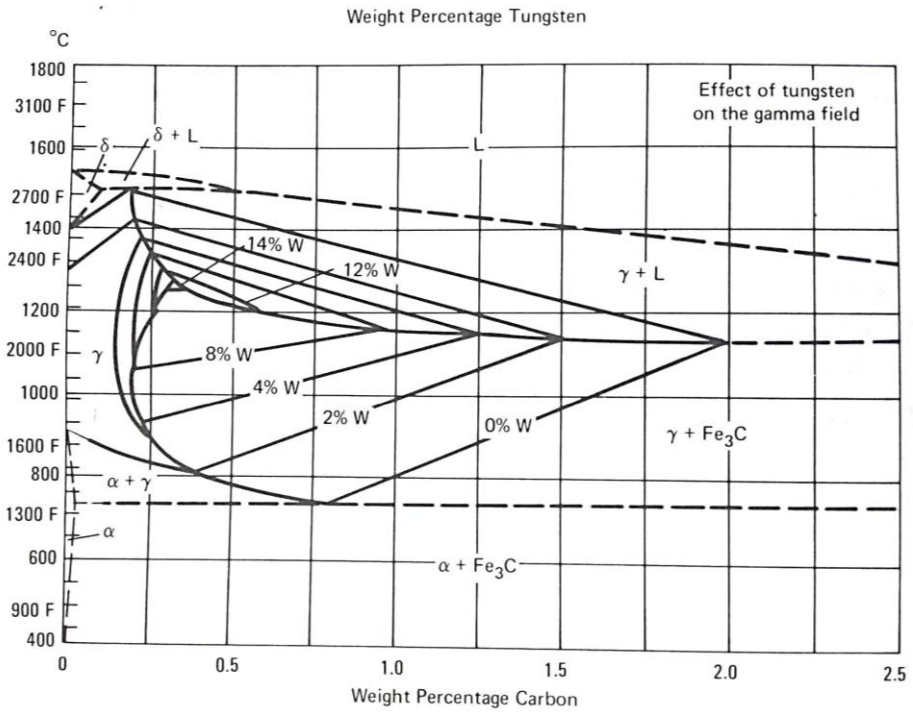

Figure 42. Phase Diagram for Fe-C-W [62]. 0.05Wt%C does not alter the W loop significantly.

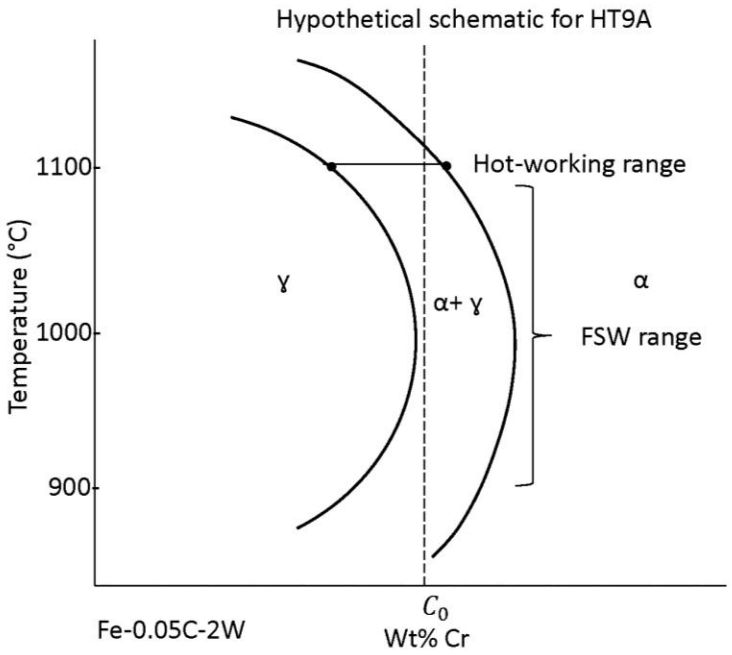

Figure 43. Hypothetical phase diagram for HT9a. The two-phase region is magnified for detail.

The role of the kinetics in the maintenance of a ferritic-martensitic microstructure after FSW should also be considered. Lakshminarayanan, Cho, and Bilgin all performed FSW on Fe-11Cr, ferritic steels with carbon contents ranging from 0.01-0.08 weight percent (Table 10). The carbon content in this work was 0.05 weight percent. Only Lakshminarayanan (0.03 weight percent carbon) and this thesis (0.05 weight percent carbon) observed martensite after welding. The results of Bilgin and Cho, did not report the observation of any martensite in the microstructure before or after FSW. An important difference in between the current work and the others is the total heat input and the cooling rate. The maximum rotational speed in this thesis is still the lowest of the four studies. As the traverse rate is the same as that in the work of Lakshminarayanan, it can be estimated that the heat input of the current study is much less. Both Cho and Bilgin used significantly higher traverse speeds. A higher traverse speed will lower heat input but will increase the cooling rate. Seemingly, increased cooling rate would promote the retention/creation of martensite. Clearly, the relationship between carbon content, rotational tool speed, traverse speed, and the formation of martensite is quite complex and merits further study.

	Carbon content (wt %)	RPM	Traverse speed (mm/min)	Martensite present?	SZ ferrite grain size (μm)
Lakshminarayanan	0.028	1000	50	yes	4
Cho	<0.08	600	254	no	1.75
Bilgin	0.01	560-1400	80-200	no	6.5
Current Results	0.05	300-400	50	yes	13

Table 10. Comparison of FSW parameters for recent work on ferritic stainless steels.

C. ASSESSMENT OF MECHANICAL PROPERTIES

The mechanical hardness was by-and-large preserved in the stir zone after friction stir welding. The hardness values in Table 8 do suggest some softening in the stir zone, due to grain coarsening in the ferrite platelets. This softening is only statistically significant for the 400 rpm condition. Again, the scatter in the data is due to substantial oscillations in hardness as a result of the presence of ferritic lamella bands, with inter-dispersed martensitic grains. The heat affected zone for both sides of the weld experienced a large degree of softening, approximately a 30% reduction from the base metal values. These effects seemed somewhat more pronounced for the hardness profile taken deeper in the sample where the temperatures should remain higher for a longer period of time.

These observations of softening in HT9A after FSW are quite different from those on other ferritic stainless steels [37-39]. All of these studies reported substantial grain refinement as compared to the base metal, while the current work reports an increase in ferrite grain size after FSW. The martensite grain size in friction stir welded HT9A does not change appreciably, so it seems that the hardness of the stir zone is controlled by the ferrite grain size.

As is often the case the thermomechanically affected zones for friction stir welded HT9A showed distinct differences from the stir zone. For the *advancing* side (AS) TMAZ, the ferrite grain size at 300 rpm is the same the stir zone (27μm). This grain size reduces substantially as the tool rotation speed increases to 400 rpm (19μm), but is still larger than the stir zone (12μm). For the *retreating* side (RS), the ferrite grain size is actually quite a bit larger than the stir zone, ranging from 23-48μm. The two hardness profiles indicated both a slight hardening in the AS TMAZ compared to the RS TMAZ. This effect was seen by Mishra, where he pointed out that the material near the top of the weld (approximately the upper one-third) moved under the influence of the shoulder rather than the threads of the pin [5]. As a result, one would expect to see a less symmetric profile and more of an affect from the advancing and retreating sides of the weld. He further points out that grains seen on the advancing side, were smaller and harder compared to larger, softer grains seen in the retreating side [5]. Nandan also noted this softening effect, where he saw a similar softening effect of FSW martensitic steels [30]. He noted, that in all cases, FSW causes a large reduction in hardness within the stir zone, and that a slower tool rotation speed would lead to a lesser reduction and a narrower weld.

D. ASSESSMENT OF MOLTEN FLUORIDE CORROSION BEHAVIOR OF HT9 PLATE AND FSW'S MATERIAL

After the investigation of tens-of-models, a relatively simple impedance model was used, with parameters reflecting changes in passivity as samples transitioned from the as received (AR) to the friction stir welded (FSW) state. This electrical circuit models contained multiple time constants, which were found essential for adequately fitting the impedance data, and were also conceptually consistent with microstructural observations of the interface. We know that the passive film formed on such an alloy may involve several discrete layers, with porous layers formed during the reaction of near-surface chromium-rich phases with the molten fluoride salts, and other oxide layers impervious to attack.

The HT9A steel exhibited reasonably good corrosion performance in molten lithium fluoride salt. At lower temperatures HT9A performed as well as if not better than the base metal. As temperature increased, corrosion resistance increased for all welded samples, with 350rpm FSW HT9A having the highest resistance and TIG welding having the lowest resistance. This trend is consistent with previous studies performed on high chromium steels (12YWT and 14YWT) exposed to LiF at temperatures greater than $550°C$ [3, 44]. In this study, Farmer et al. demonstrated an increase in corrosion resistance due to the formation of a passive film between the temperatures 600℃ and 800℃. For HT9A, the formation of a passive film occurred due to the breakdown of the high purity alumina crucible used to contain the LiF and HT9A buttons. Quantitative EDS used to estimate the near surface concentration of aluminum, showed a clear correlation between aluminum content and polarization resistance observed.

Linescans and points taken within the matrix of each sample clearly demonstrated that the aluminum came from the crucible, as the chemical composition of HT9A did not contain any aluminum. Preferential leaching of chromium from the HT9A into the LiF resulted in a decrease in chromium content in the first 5 microns of the surface. Simultaneously, as corrosion occurred in the surface layer, aluminum diffused from the alumina crucible into the steels matrix. Both the leaching of chromium and the diffusion of aluminum was seen for all samples at both 600 and 800°C, with the exception of 350rpm FSW HT9A at 600°C, which contained no aluminum surface layer until exposure at the higher temperature of 800°C. Although a different crucible was used for each LiF exposure, thus preventing possible contamination, the purity and composition of each crucible was not tested beforehand and therefore could have contributed to the breakdown of the crucibles.

Finally, the instantaneous corrosion rate of the welded material was not meaningfully affected by the tool rotational speed. While 350rpm FSW HT9A exhibited a higher polarization resistance at both temperatures, this same trend was not seen for admittance or capacitance. While it may seem plausible that 350rpm is the optimal tool rotation rate for FSW HT9A, it cannot be solely verified utilizing polarization resistance.

Compared with other studies involving the exposure of high chromium steels to LiF, HT9A significantly underperformed. Farmer et al. saw a polarization resistance for ODS steels exposed to LiF salts between 550 and 900℃, between the values of 20 and 120 ohms [3, 44]. At similar temperatures, HT9A obtained vales between 0.1 and 0.9 ohms. While HT9A may not outperform certain high chromium steels, more important is its ability to perform as well, if not better, than both TIG welded HT9A and base metal at high temperatures.

V. CONCLUSION

1. *Demonstrate the feasibility of FSW HT9*

HT9A ferritic martensitic steel was successfully joined by friction stir welding over a series of welding parameters. The welds at each condition were defect-free and required relatively low loads during welding, which should prolong tool life.

2. *Determine microstructural and mechanical property relationships subsequent to FSW*

The ferritic martensitic microstructure of HT9A steel was preserved with little change during friction stir welding. A small, but measurable, change in the morphology of the martensitic grains after welding was observed. As the rotational speed of the tool increased, the martensitic grains became more equiaxed. Some refinement in the ferrite plate grain size was observed after welding with the degree of refinement increasing with increasing rotational tool speed.

The mechanical properties of the stir zone and the thermomechanically-affected zones, as measured by indentation, were similar to the base plate material. The hardness of the stir-zone was reduced by about ten percent from the plate value, while the thermo-mechanically affected zone, for each rotational speed, was comparable to that of the base plate material. A significant softening was observed in the heat-affected zone on both sides of the weld.

3. *Assess molten fluoride corrosion behavior of HT9 plate and FSW'd material.*

The HT9A steel exhibited reasonably good corrosion performance in molten lithium fluoride salt. The base plate material displayed a slightly lower instantaneous corrosion rate than the welded material. The instantaneous corrosion rate of the welded material was not meaningfully affected by the tool rotational speed.

THIS PAGE INTENTIONALLY LEFT BLANK

APPENDIX A: OTHER MODELS INVESTIGATED FOR EIS

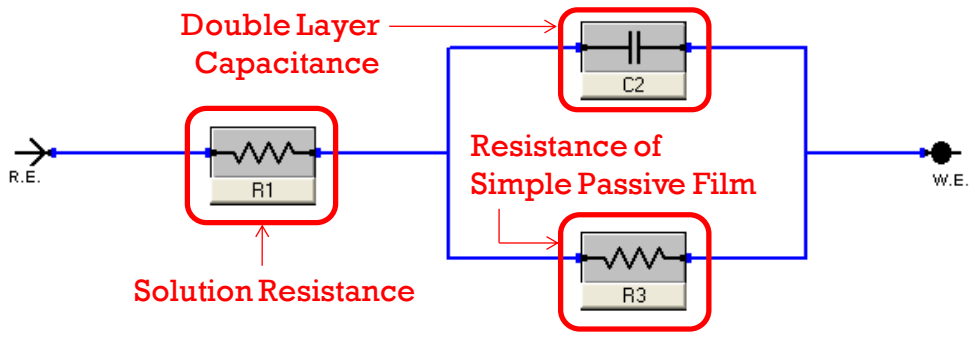

Figure 44. Simple single time constant RC network

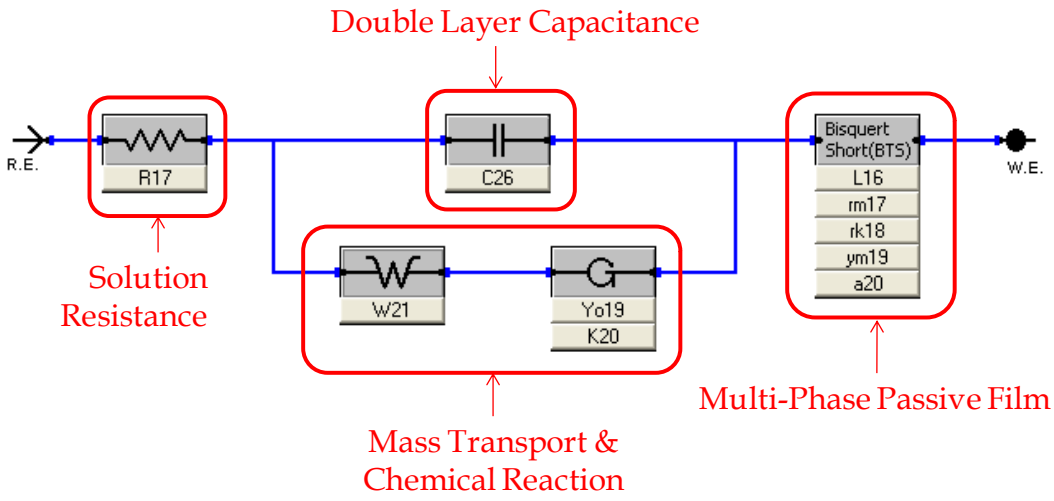

Figure 45. Warburg/Gerischer/Bisquert short.

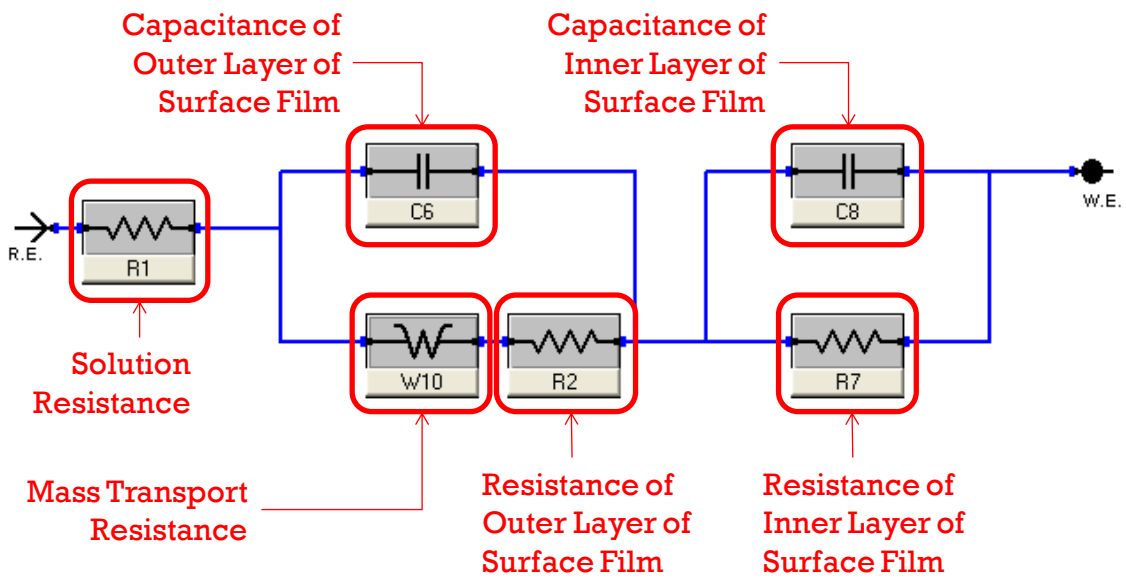

Figure 46. Warburg/outer layer/inner layer.

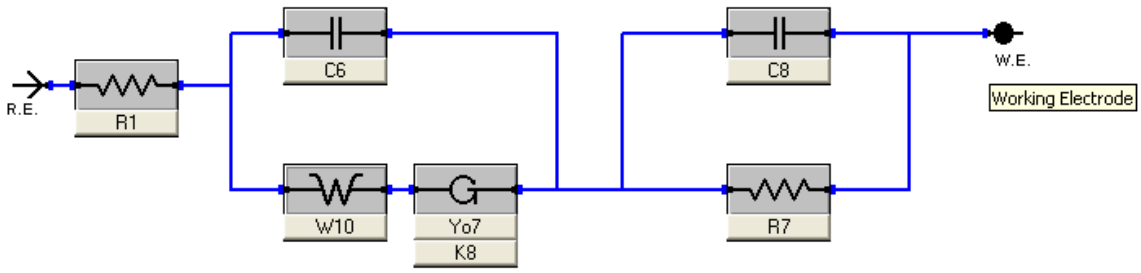

Figure 47. Solution resistance (1); Warburg impedance, Gerischer impedance, capacitance (2); and RC parallel (3)

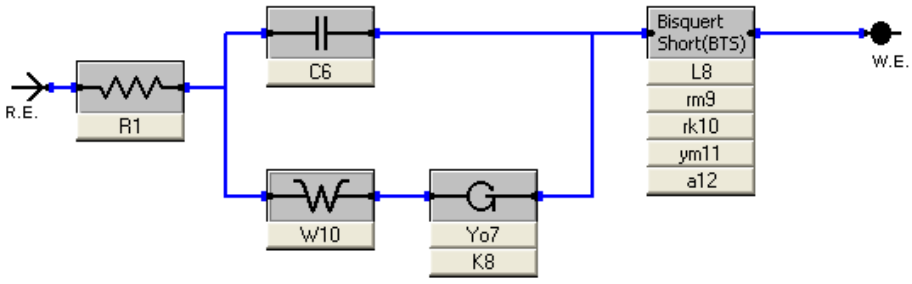

Figure 48. Solution resistance(1); Capacitance, Warburg, Gerischer (2); and Bisquert short impedance (3.

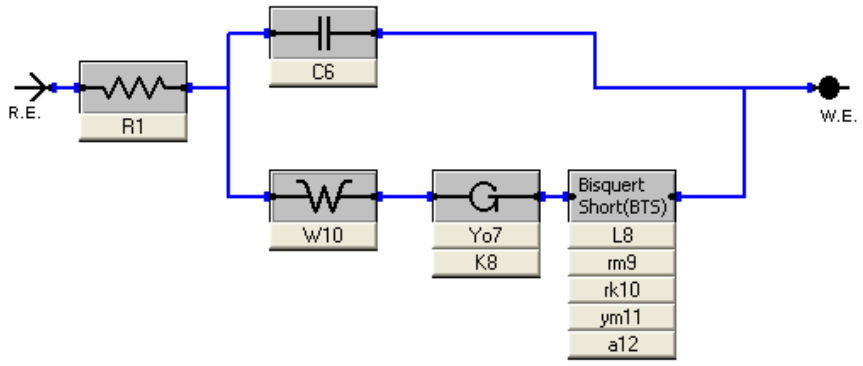

Figure 49. Solution resistance (1); Capacitance, Warburg impedance, Gerischer impedance & Bisquert short impedance (2).

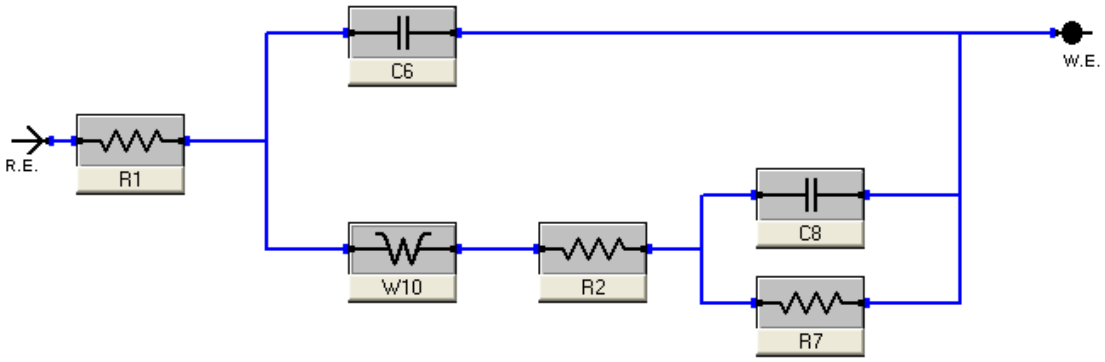

Figure 50. Solution resistance (1); Double layer capacitance (2); Warburg impedance (3); and Simple three-element RC circuit (4).

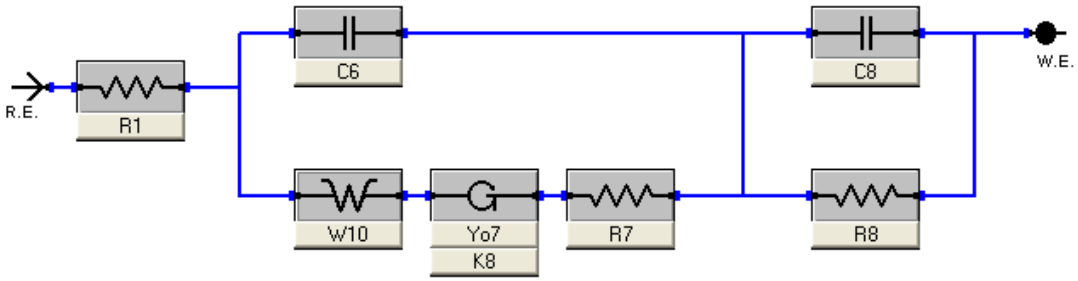

Figure 51. Solution resistance (1); Double layer capacitance (2); Warburg impedance (3); Gerischer impedance (4); Simple resistance (5); and RC parallel (6).

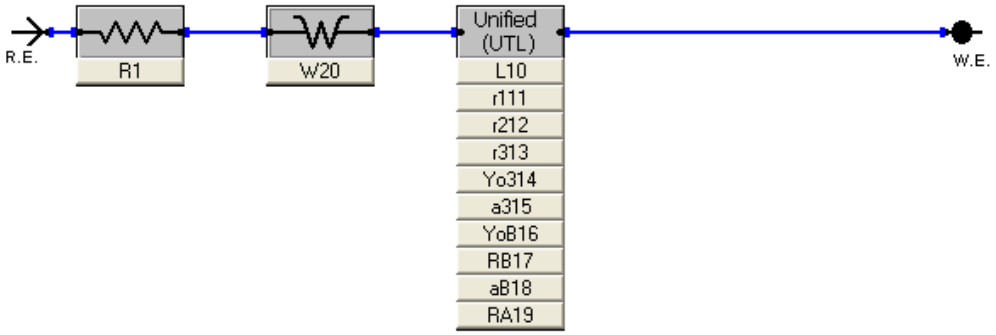

Figure 52. Solution resistance (1); Warburg impedance (2); Unified transmission line UTL model (2).

APPENDIX B: BISQUERT SHORT MODEL

The Bisquert Impedance account for conduction through a convoluted porous interface and is:

$$\widehat{Z} = \frac{1}{R_k^{-1} + (j\omega)^a Y_m} \qquad \text{(Equation 15)}$$

$$\widehat{Z} = \frac{\left\{ \begin{array}{l} L\lambda\chi_1\chi_2(\chi_1+\chi_2)S_\lambda + \chi_1(\lambda\chi_1 S_\lambda + L\chi_2 C_\lambda)Z_A \\ + \chi_2(\lambda\chi_2 S_\lambda + L\chi_1 C_\lambda)Z_B + \dfrac{Z_A Z_B}{\chi_1+\chi_2}\left(2\chi_1\chi_2 + (\chi_1^2+\chi_2^2)C_\lambda + \dfrac{L}{\lambda}\chi_1\chi_2 S_\lambda\right) \end{array} \right\}}{(\chi_1+\chi_2)\left\{\lambda(\chi_1+\chi_2)S_\lambda + (Z_A+Z_B)C_\lambda + \dfrac{Z_A Z_B S_\lambda}{\lambda(\chi_1+\chi_2)}\right\}} \qquad \text{(Equation 16)}$$

$$C_\lambda = \cosh(L/\lambda) \qquad \text{(Equation 17)}$$

$$S_\lambda = \sinh(L/\lambda) \qquad \text{(Equation 18)}$$

$$\lambda = (\xi/(\chi_1+\chi_2))^{1/2} \qquad \text{(Equation 19)}$$

THIS PAGE INTENTIONALLY LEFT BLANK

APPENDIX C: IMPEDANCE AND PHASE AMPLITUDE

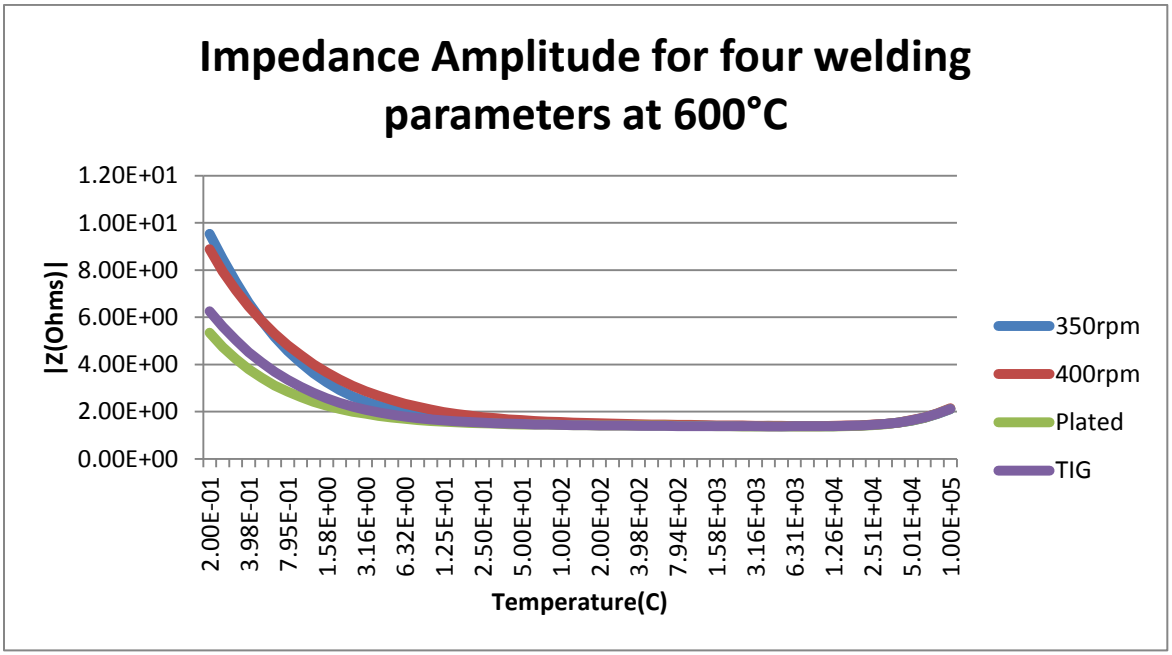

Figure 53. Impedance for four welding parameters at 600°C.

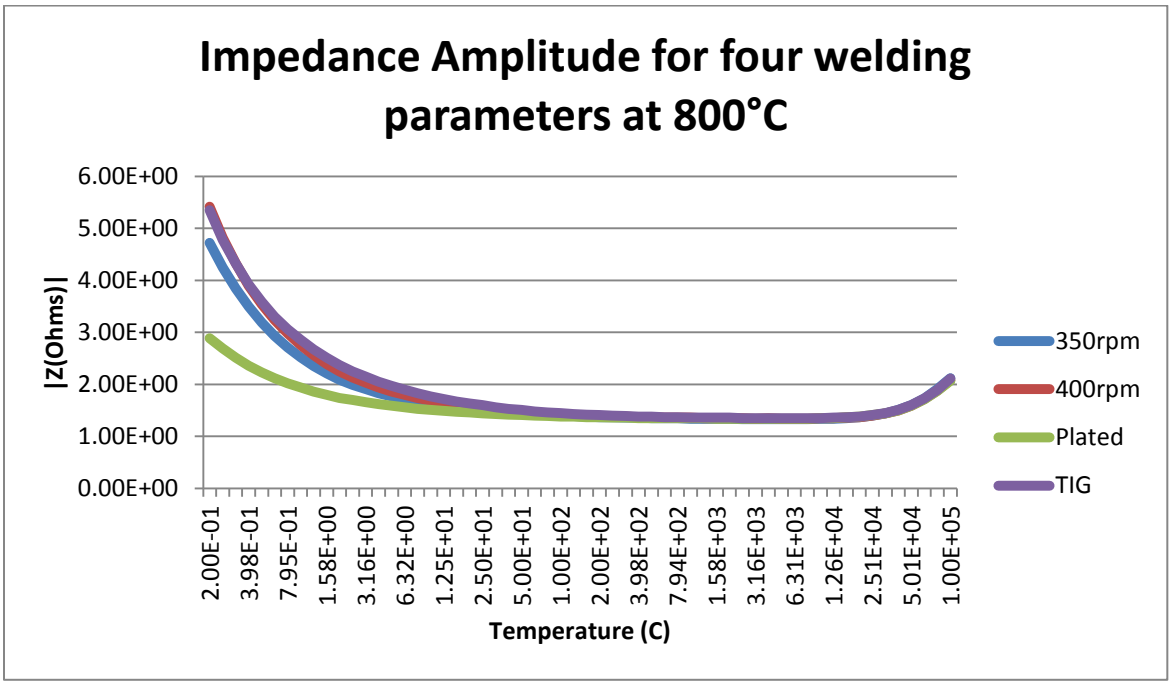

Figure 54. Impedance for four welding parameters at 800°C.

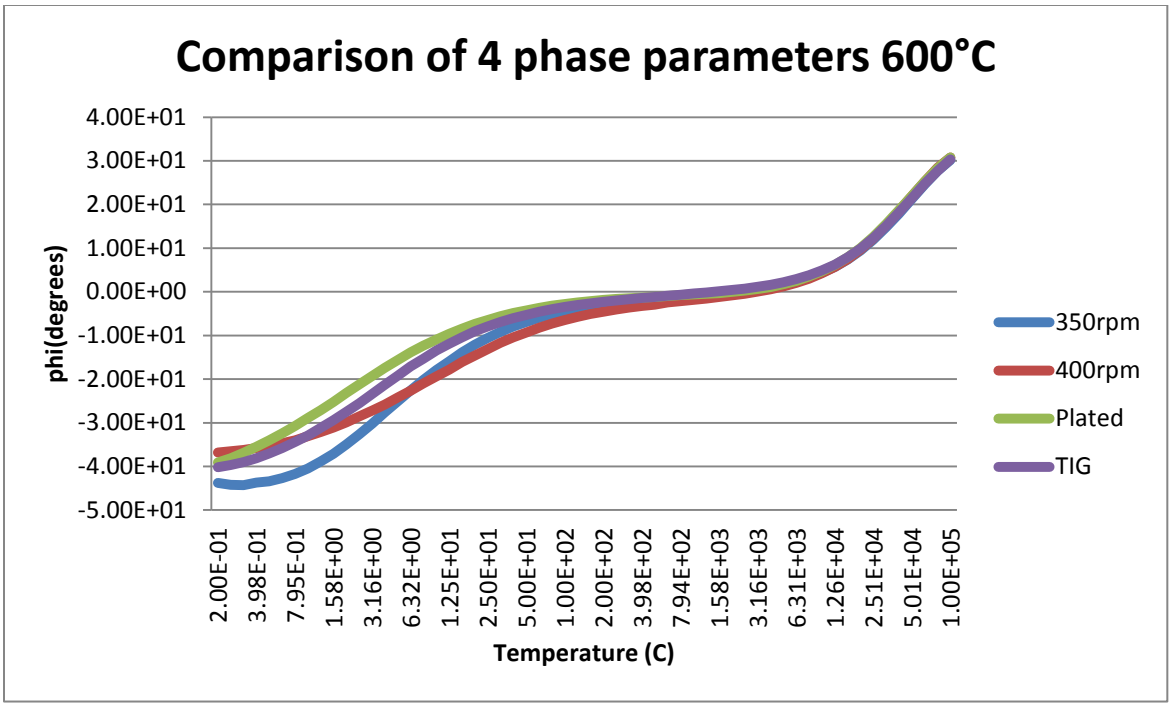

Figure 55. Comparison of the four phase parameters at 600°C.

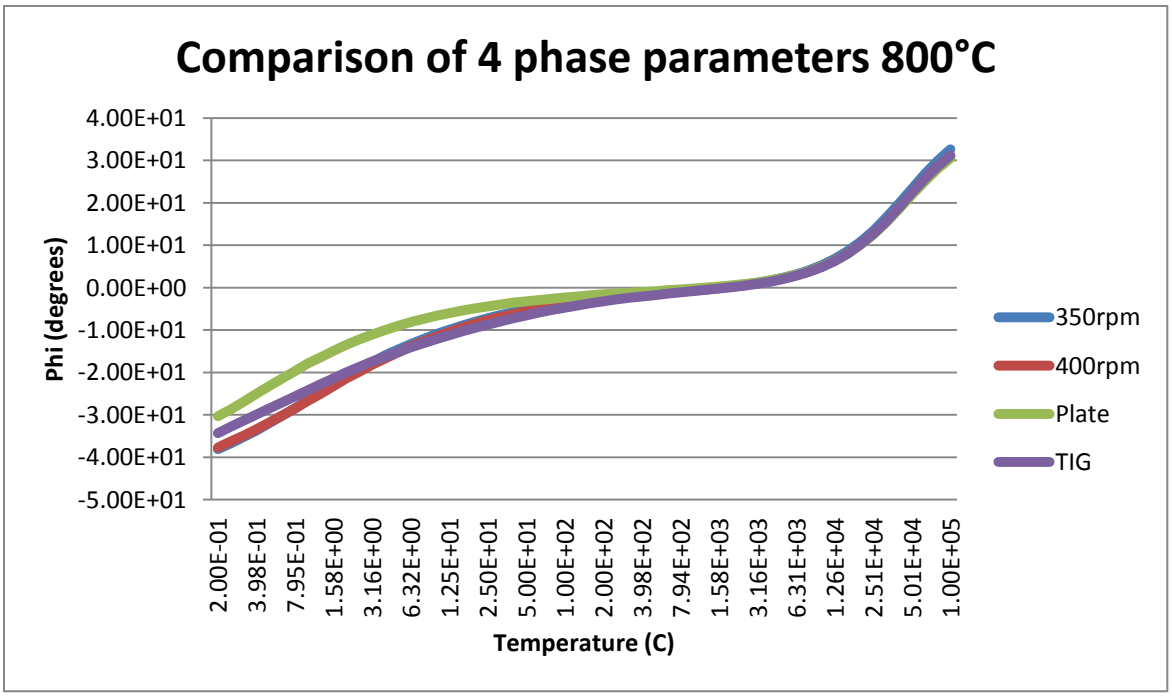

Figure 56. Comparison of the four phase parameters at 800°C.

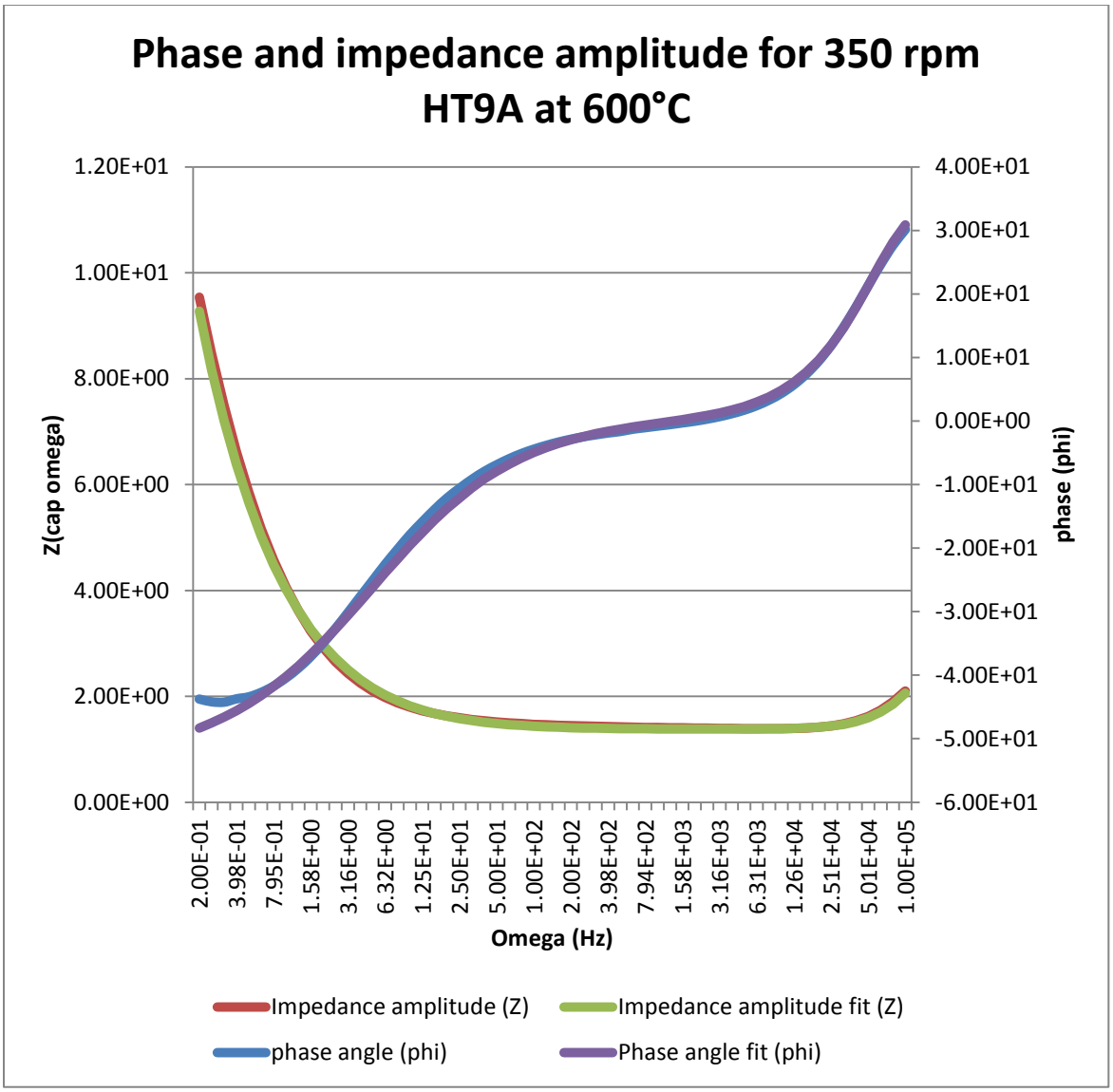

Figure 57. Phase and impedance amplitudes for 350 rpm FSW HT9A at 600°C.

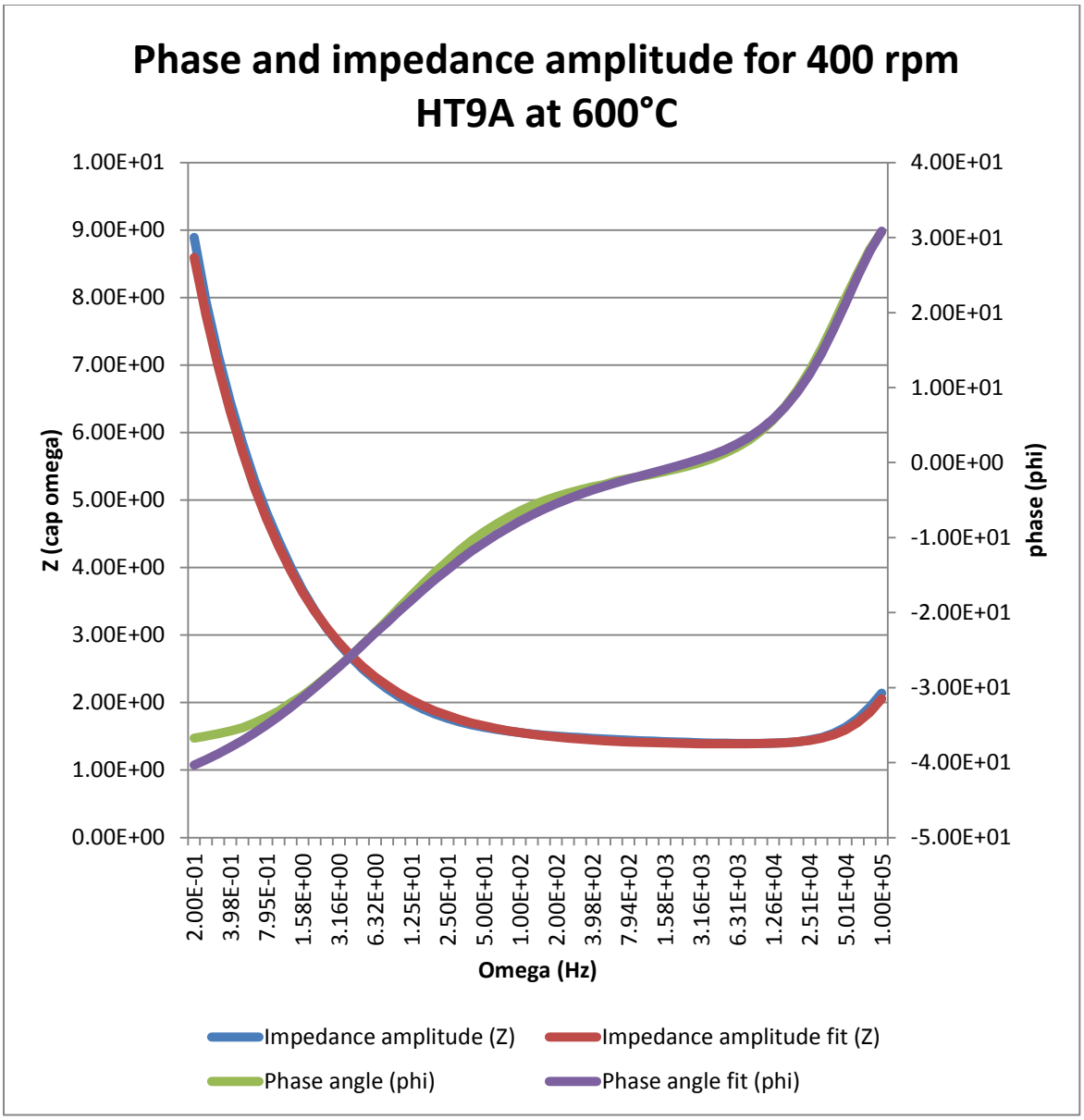

Figure 58. Phase and impedance amplitude for 400 rpm FSW HT9A at 600°C.

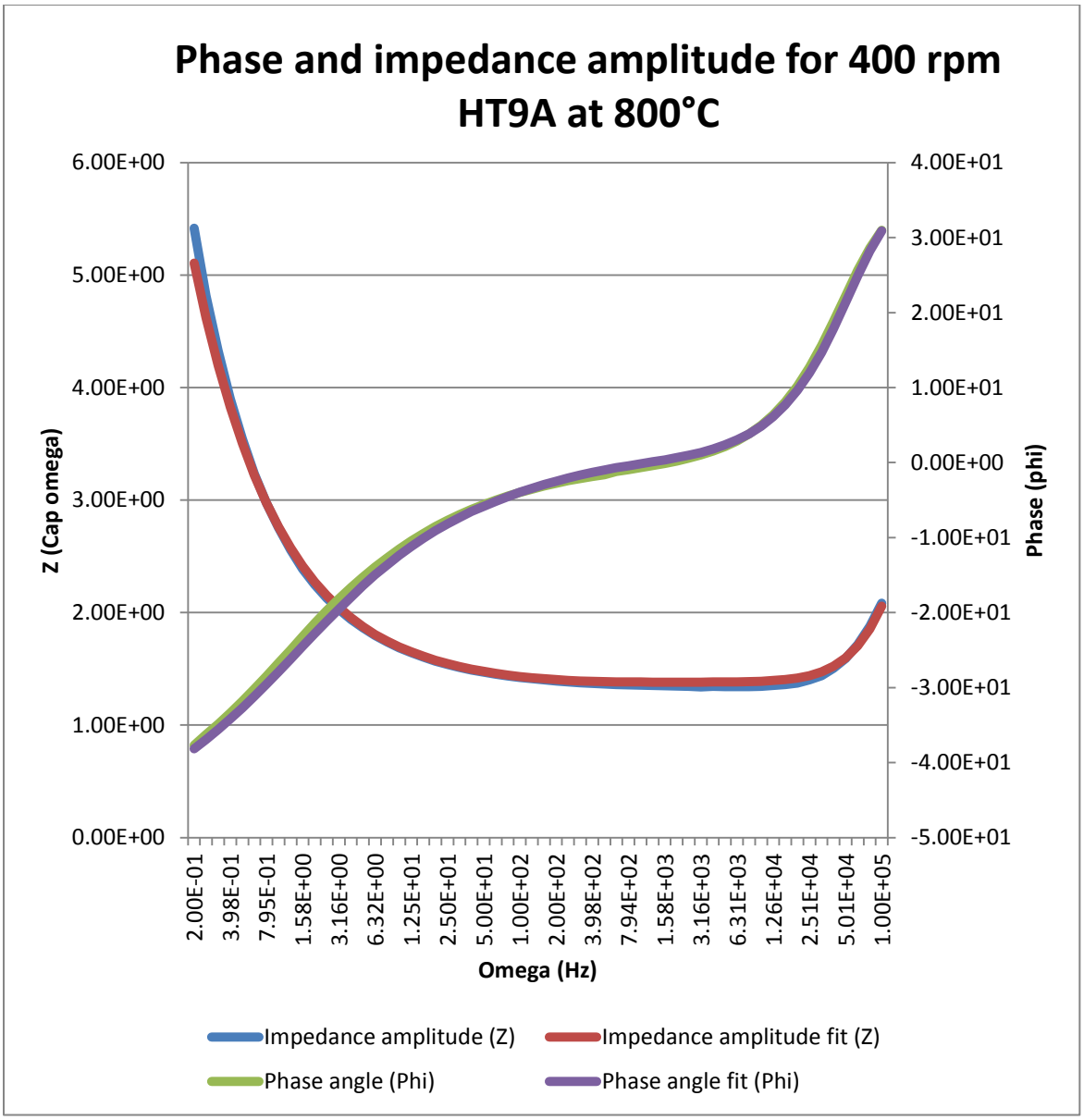

Figure 59. Phase and impedance amplitude for 400 rpm FSW HT9A at 800°C.

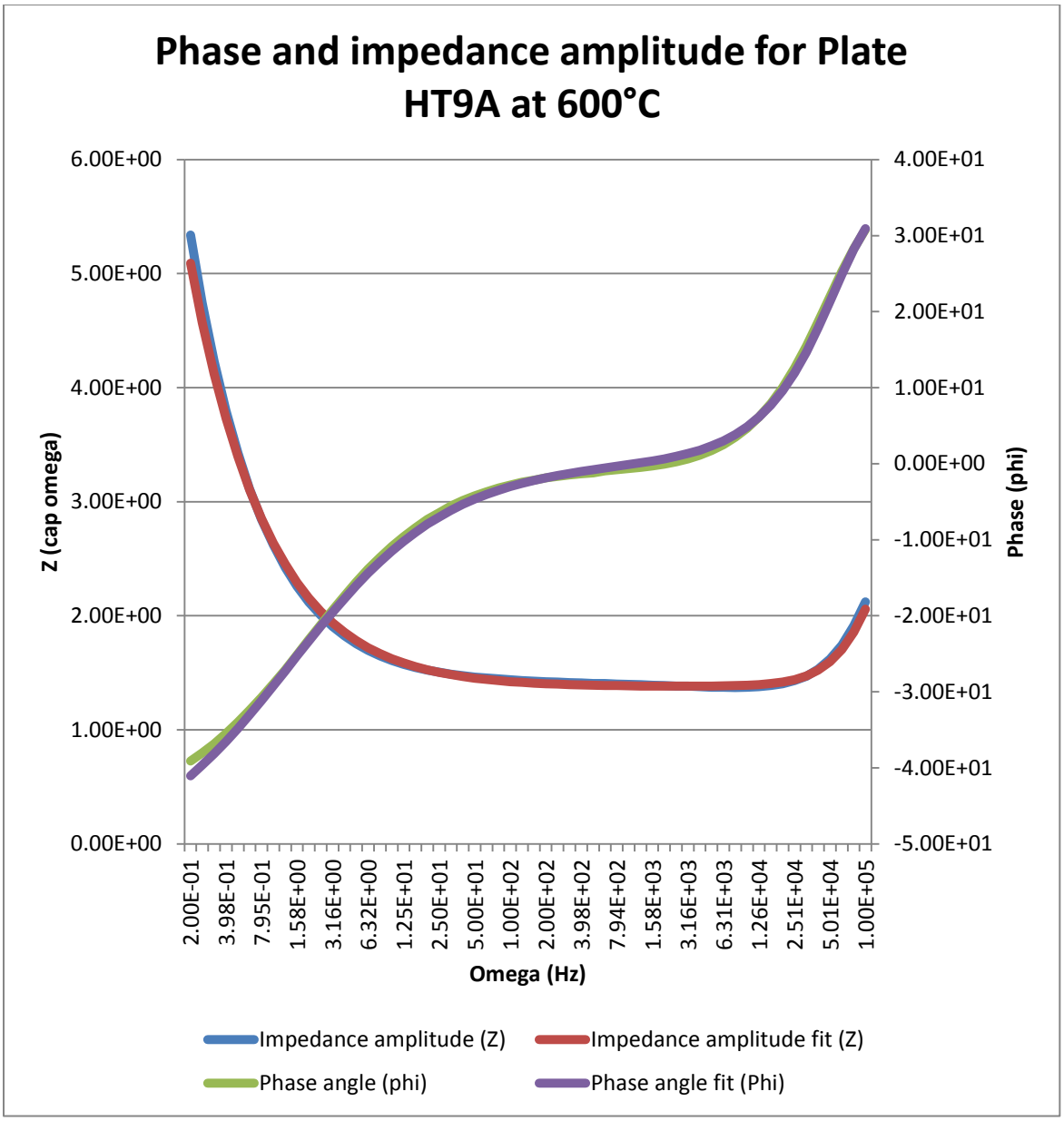

Figure 60. Phase and impedance amplitude for plate HT9A at 600°C.

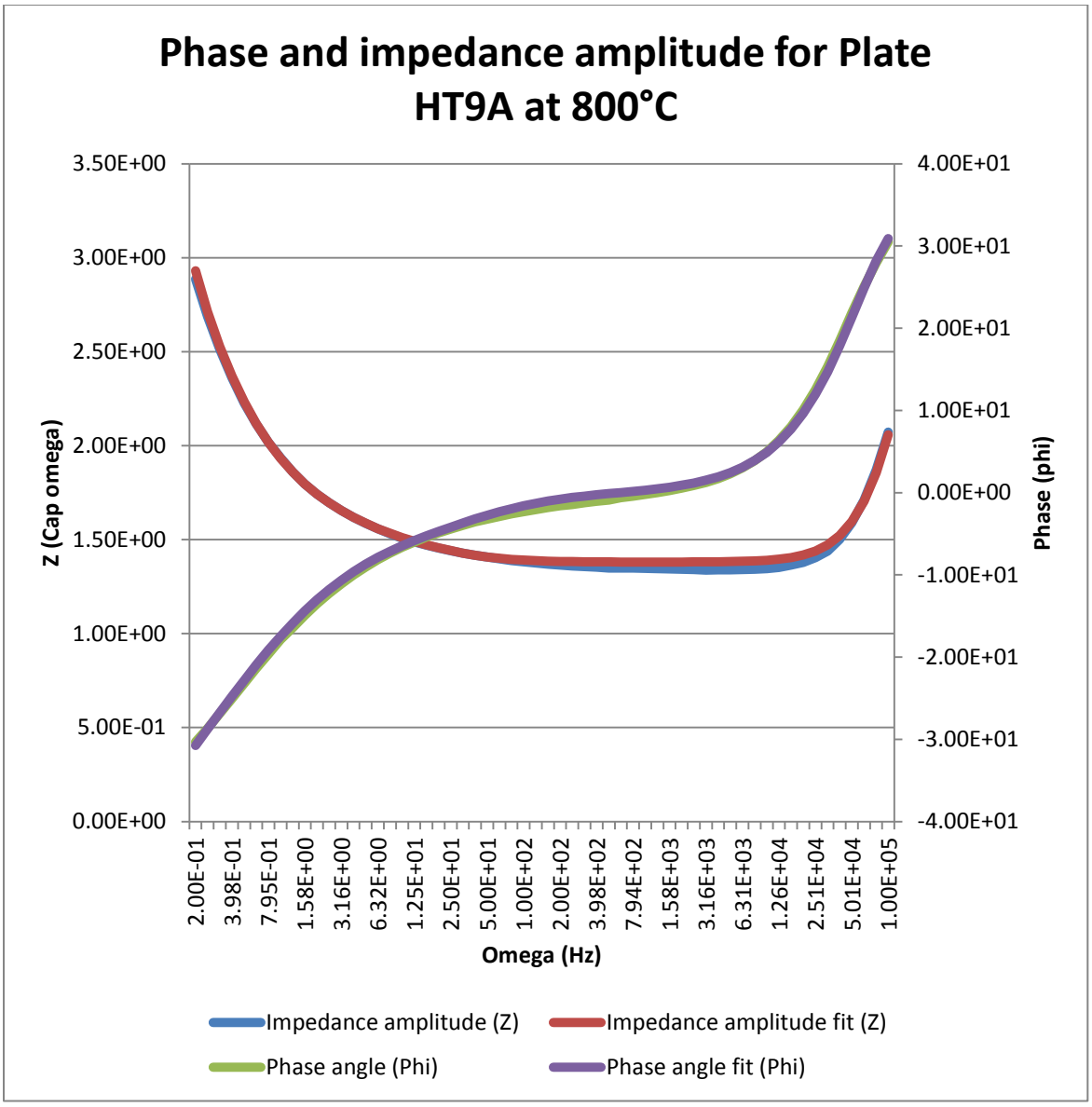

Figure 61. Phase and impedance amplitude for plate HT9A at 800°C.

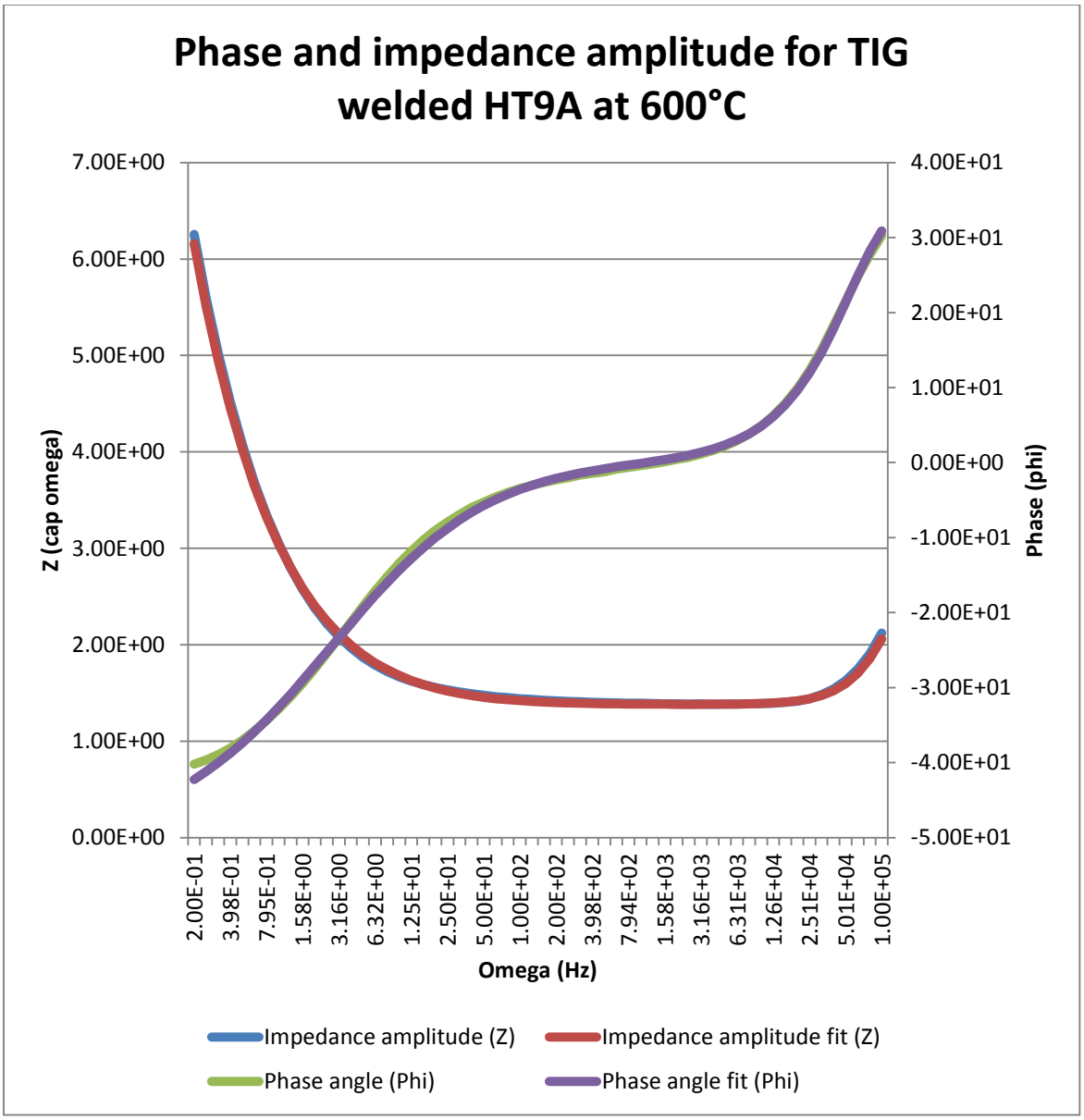

Figure 62. Phase and impedance amplitude for TIG welded HT9A at 600°C.

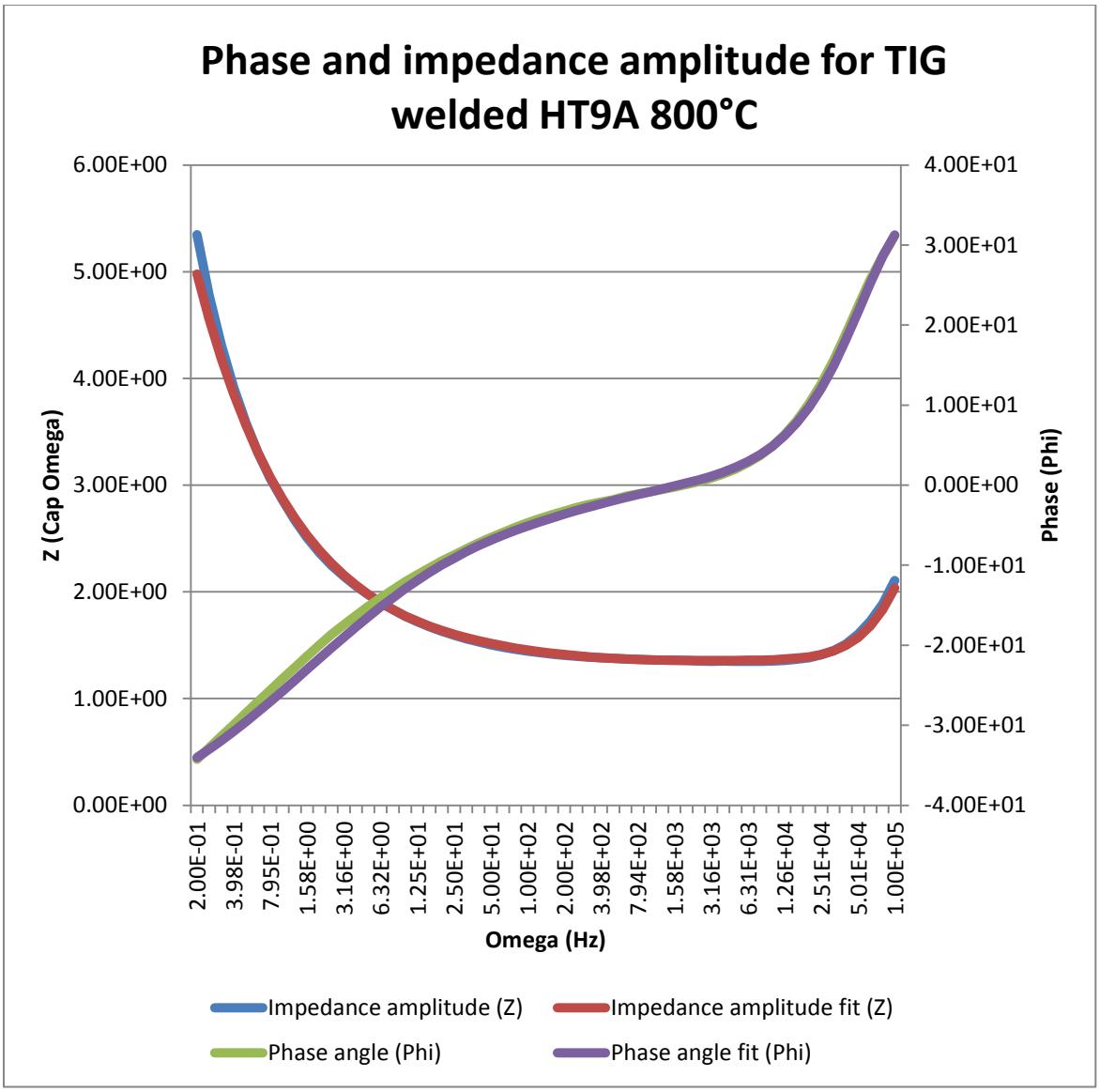

Figure 63. Phase and impedance amplitude for TIG welded HT9A at 800°C

THIS PAGE INTENTIONALLY LEFT BLANK

APPENDIX D: EDS DATA

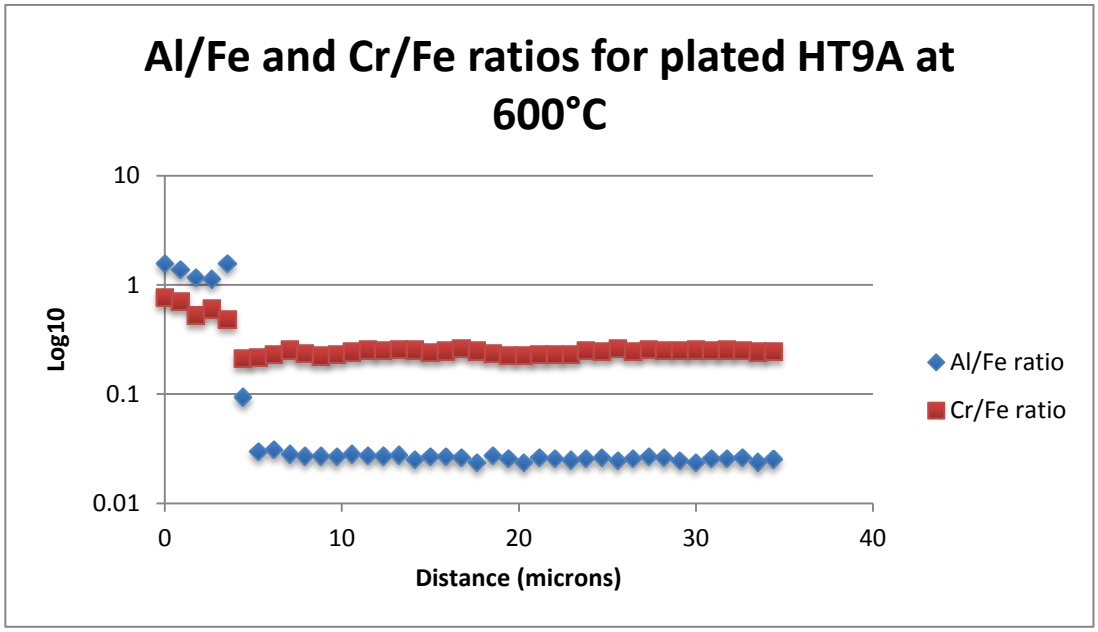

Figure 64. Al/Fe and Cr/Fe ratios for plated HT9A at 600°C.

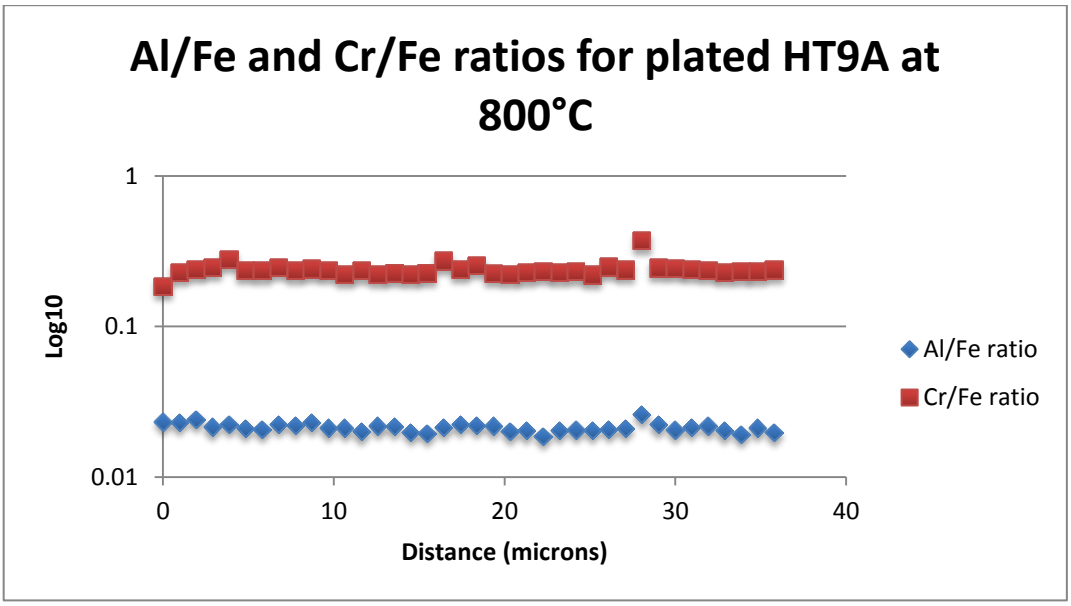

Figure 65. Al/Fe and Cr/Fe ratios for plated HT9A at 800°C.

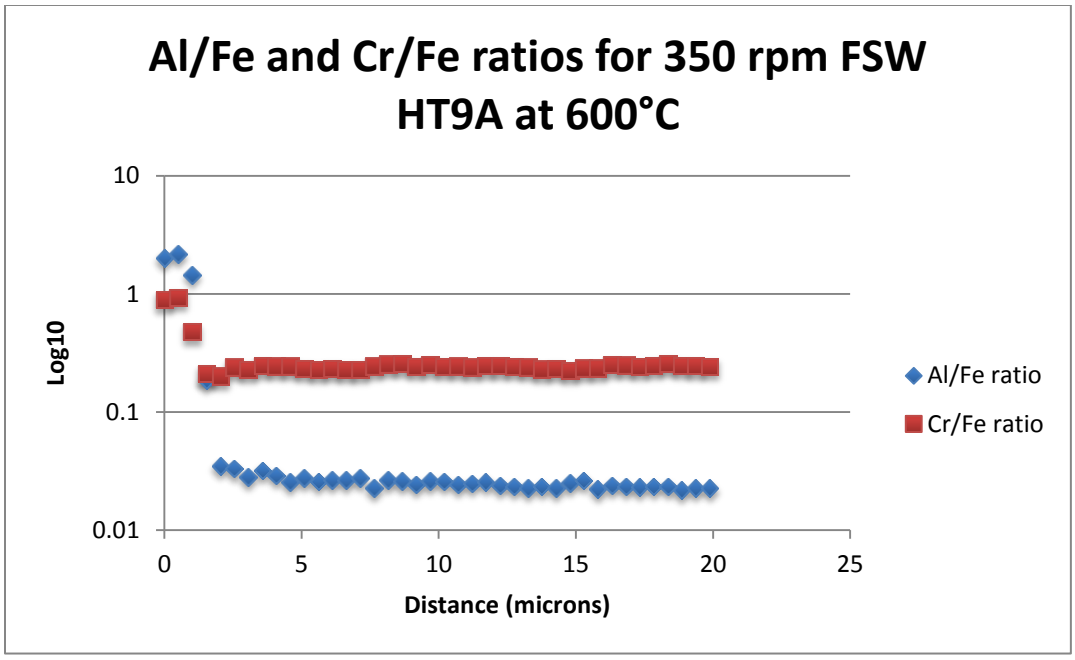

Figure 66. Al/Fe and Cr/Fe ratios for 350 rpm FSW HT9A at 600°C.

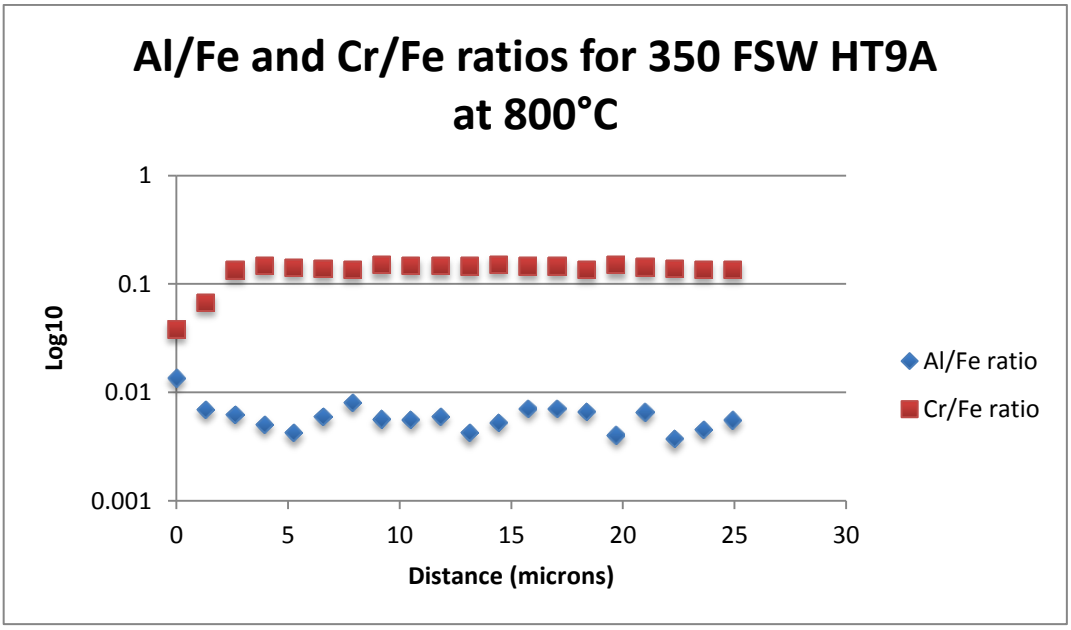

Figure 67. Al/Fe and Cr/Fe ratios for 350 FSW HT9A at 800°C.

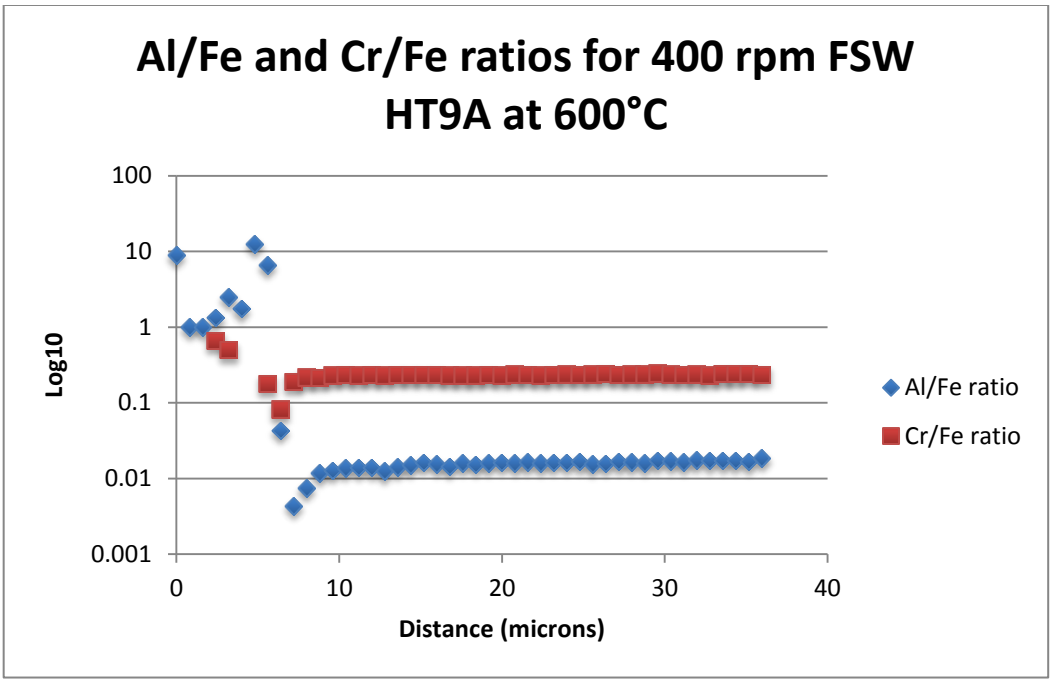

Figure 68. Al/Fe and Cr/Fe ratios for 400 rpm FSW HT9A at 600°C.

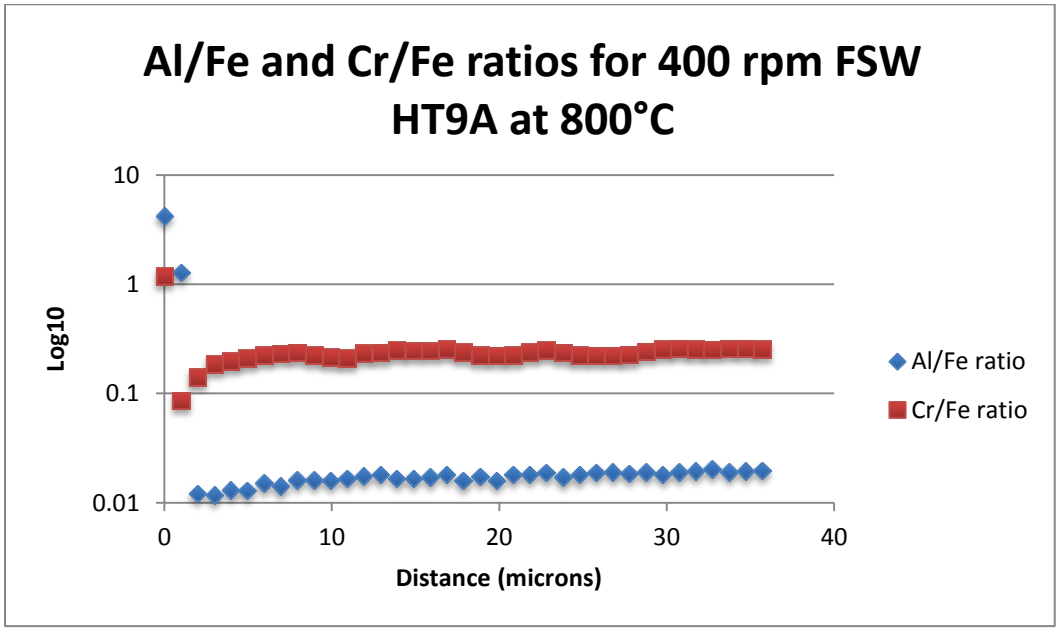

Figure 69. Al/Fe and Cr/Fe ratios compare to base signal (SE2) for 400 rpm FSW HT9A at 800°C.

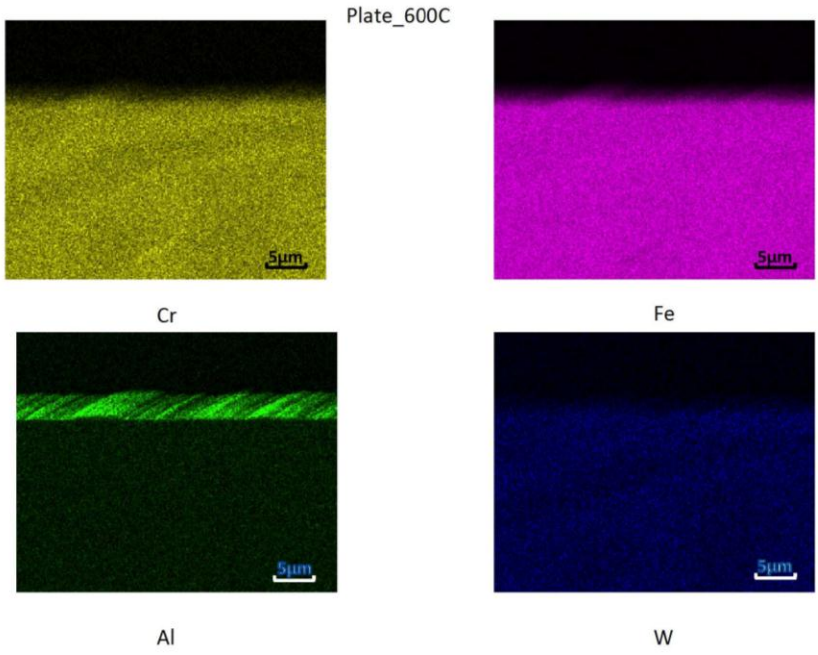

Figure 70. EDS scan for plate HT9A at 600°C.

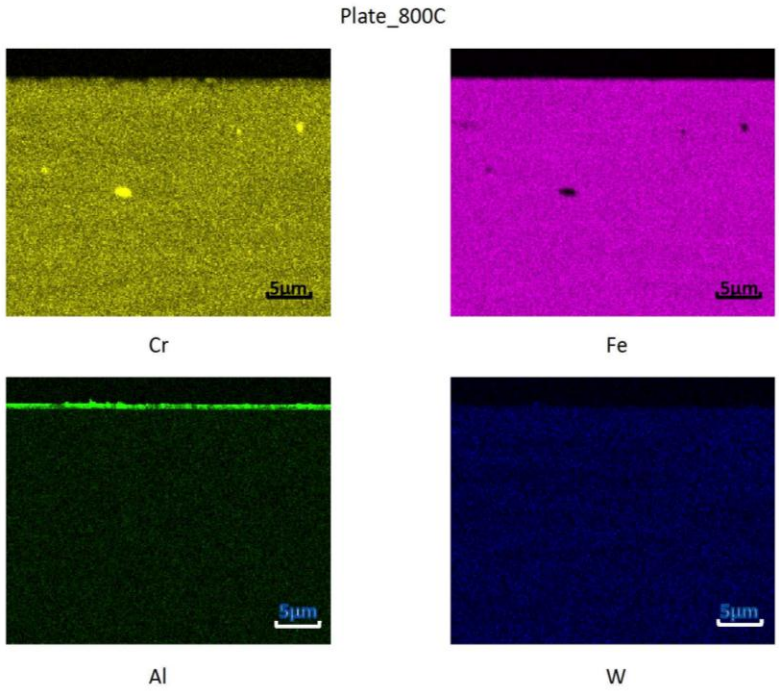

Figure 71. EDS scan for plate HT9A at 800°C.

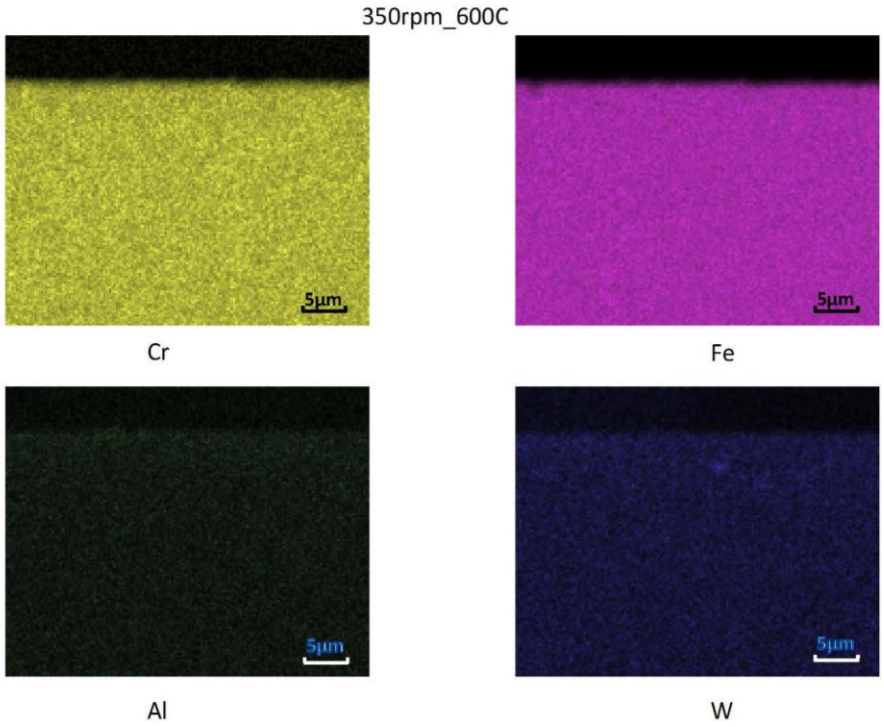

Figure 72. EDS scan for 350 rpm FSW HT9A at 600°C.

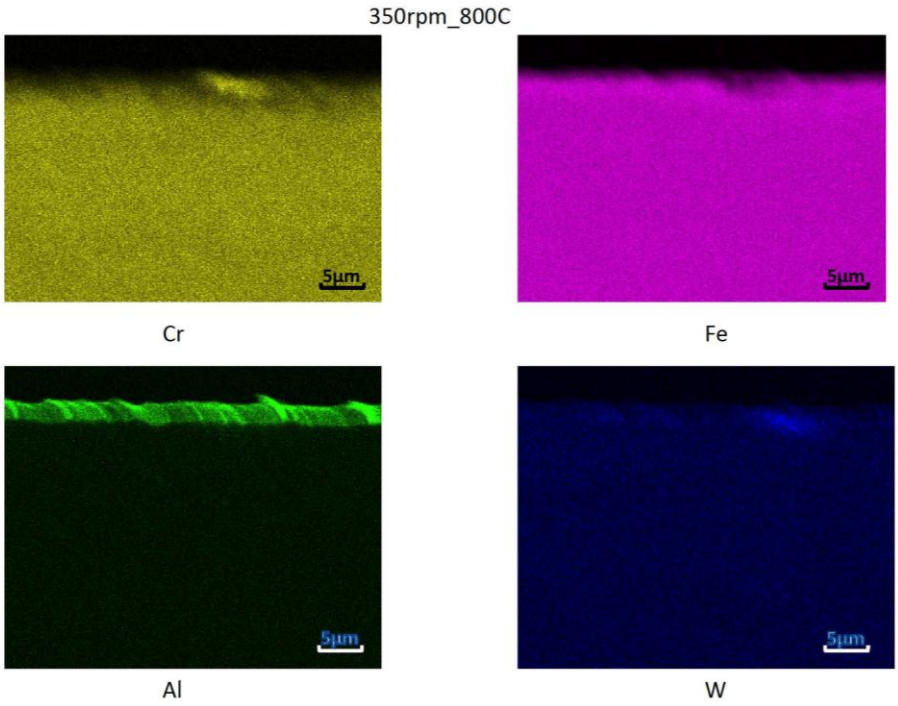

Figure 73. EDS scan for 350 rpm FSW HT9A at 800°C.

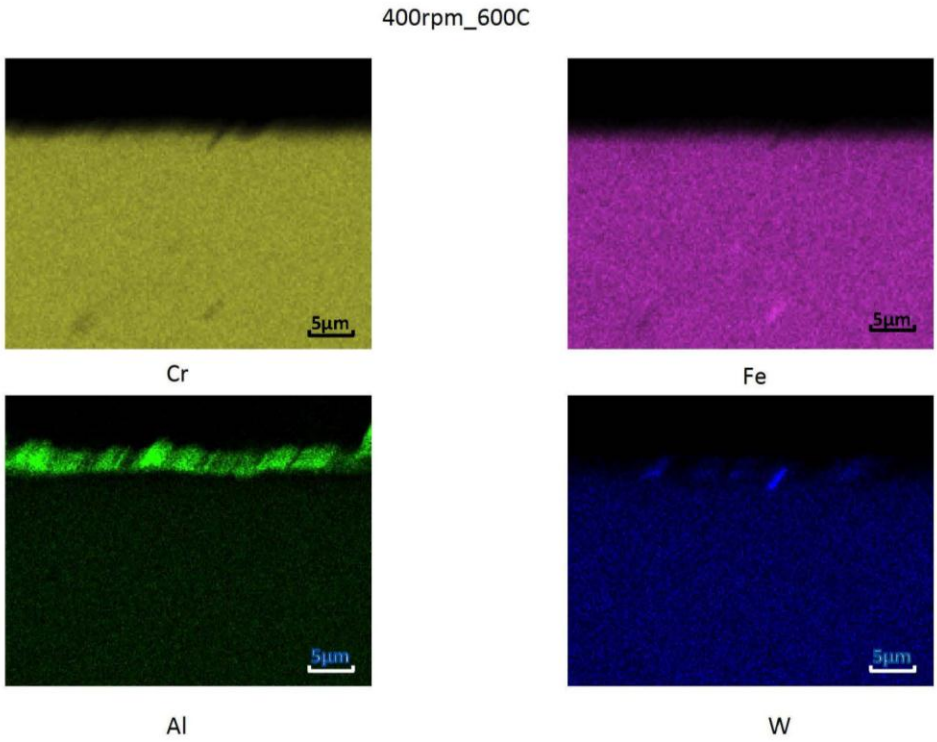

Figure 74. EDS Scan for 400 rpm FSW HT9A at 600°C.

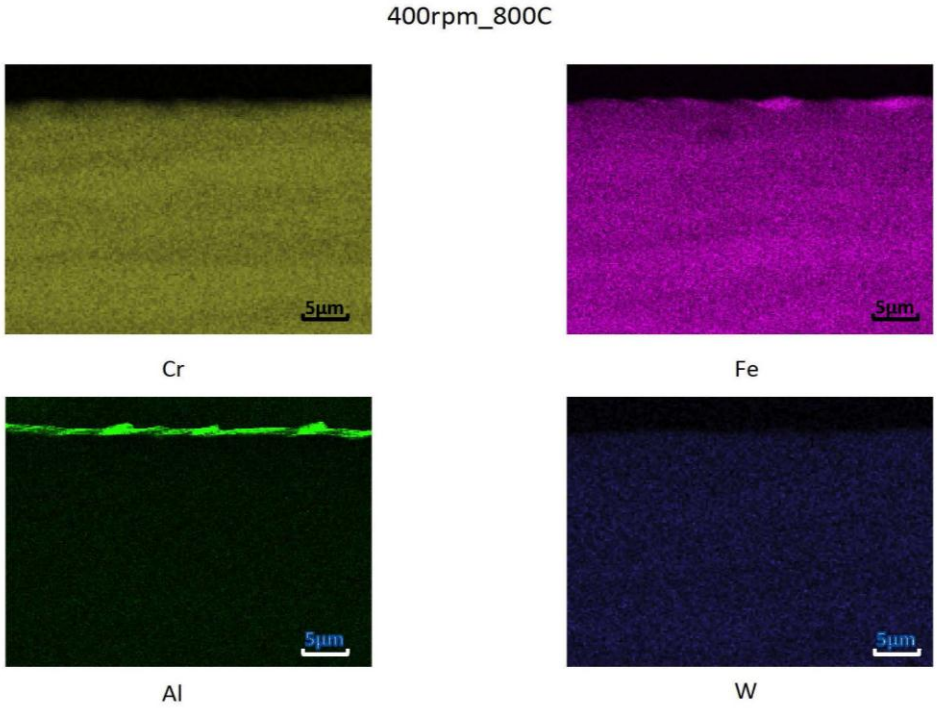

Figure 75. EDS scan for 350 rpm FSW HT9A at 800°C.

APPENDIX E: EBSD DATA

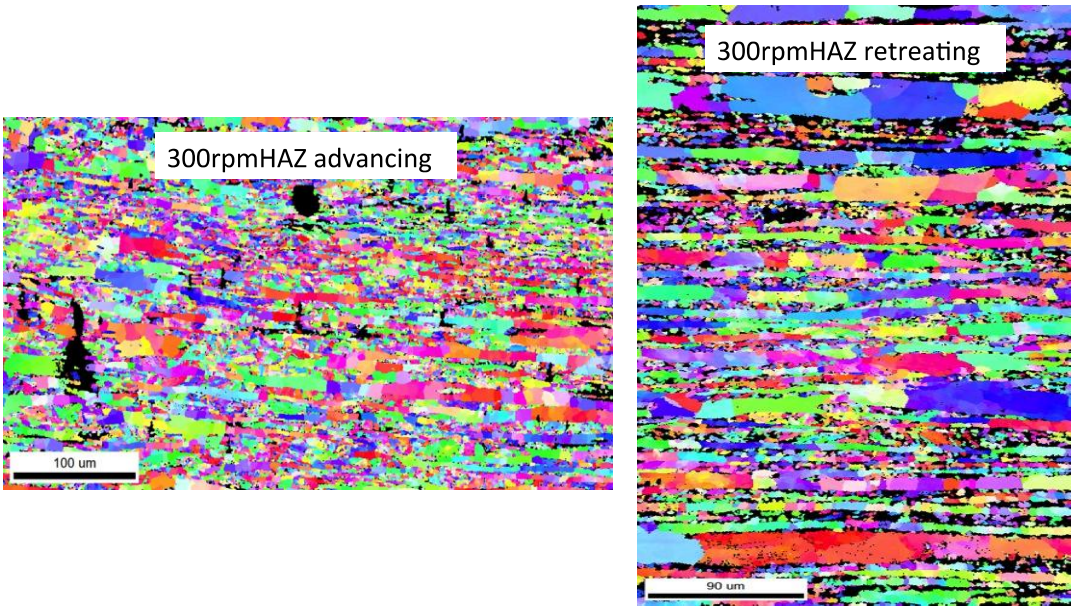

Figure 76. Comparison of advancing and retreating TMAZ for 300 rpm FSW, taken at 0.5-micron step size.

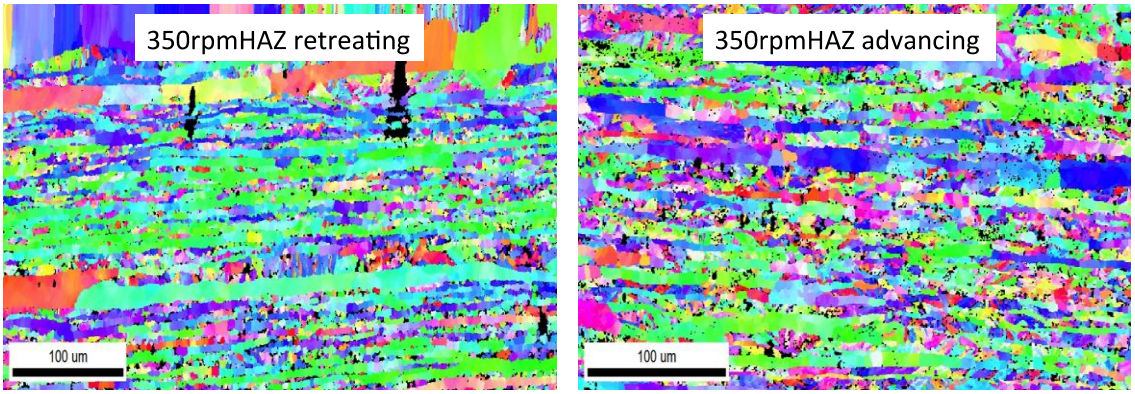

Figure 77. Comparison of advancing and retreating TMAZ for 350 rpm FSW, taken at 0.5-micron step size.

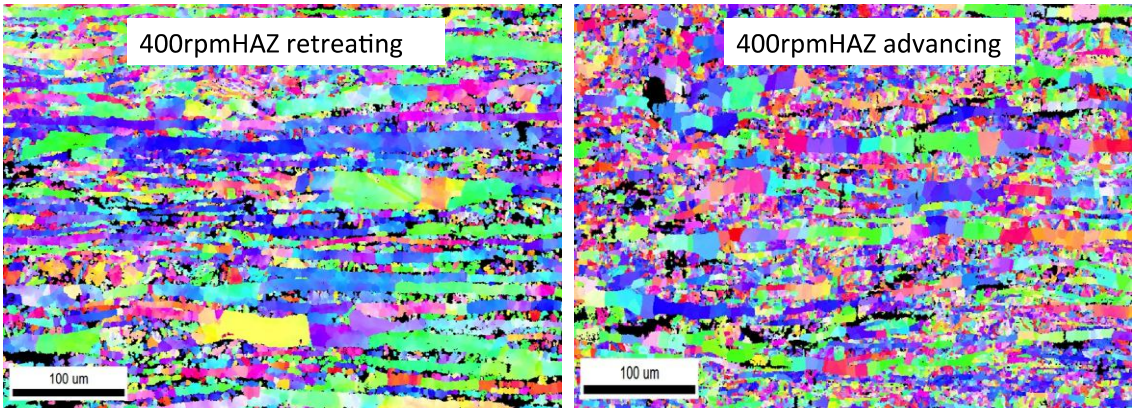

Figure 78. Comparison of advancing and retreating TMAZ for 400 rpm FSW, taken at 0.5-micron step size.

300rpm Parameter	Hardness (Gpa)	Modulus of Elasticity (Gpa)
CSZ	3.4±0.5	216.9±8.1
TMAZ	3.9±1.0	231.3±8.5
HAZ	3.1±5.4	221.8±5.4
Base	3.9±0.7	225.2±7.6

Table 11. Hardness data for 300 rpm indicating softening in stir zone, significant softening in HAZ and regain in hardness in base material.

400rpm Parameter	Hardness (Gpa)	Modulus of Elasticity (Gpa)
CSZ	3.2±0.5	215.0±4.5
TMAZ	3.7±0.7	216.5±7.9
HAZ	2.7±0.3	213.1±5.4
Base	4.0±0.5	221.3±5.1

Table 12. Hardness data for 400 rpm indicating softening in stir zone, significant softening in HAZ and regain in hardness in base material.

LIST OF REFERENCES

[1] U. Mustafa, "On the radiation damage characterization of candidate first wall materials in a fusion reactor using various molten salts," *Journal of Nuclear Materials*, vol. 359, no. 3, pp. 192–193, 201, August 2006.

[2] O. Chopra and D. Smith, "Low-cycle fatigue behavior of HT-9 alloy in a flowing-lithium environment," Argonne National Laboratory, Argonne, IL, Tech. Rep. CONF-830659-4, 1983.

[3] J. C. Farmer et al., "Corrosion of ferritic steels in high temperature molten salt coolants for nuclear applications," Lawrence Livermore National Laboratory, Lawrence, CA, Tech. Rep.LLNL-CONF-409085, 2008.

[4] H. Tanigawa et al., "Technical issues of reduced activation ferritic/martensitic steels for fabrication of ITER test blanket modules," *Fusion Engineering and Design*, vol. 83, no. 7-9, pp. 1471–1476, June 2008.

[5] R. S. Mishra and Z. Y. Ma, "Friction stir welding and processing," *Materials Science and Engineering R-Reports*, vol. 50, no. 1, pp. 1–78, August 2005.

[6] J. C. Feng, Y. C. Chen and H. J. Liu, "Effect of post-weld heat treatment on the mechanical properties of friction stir welded joints of 2219-O aluminum alloy," *Journal of Materials Science*, vol. 22, no. 1, pp. 297–299, January 2006.

[7] M. G. McKimpson and D. Odonnell, "Joining ODS materials for high-temperature applications," *Journal of the Minerals Metals and Materials Society*, vol. 46, no.7, pp. 49–51, July 1994.

[8] N. Sanghoon et al., "Microstructure and mechanical properties of friction stir processed ODS ferritic steels," *Journal of Nuclear Materials*, vol. 417, no. 1-3, pp. 245–248, October 2011.

[9] F. Legendre et al., "Some microstructural characterizations in a friction stir welded oxide dispersion strengthened ferritic steel alloy," *Journal of Nuclear Materials*, vol. 386-388, no. 1, pp. 537–539, April, 2009.

[10] M. H. Mathon et al., "Study of PM2000 microstructure evolution following FSW process," *Journal of Nuclear Materials*, vol. 386, no. 1, pp. 475–478, April 2009.

[11] P. Miao et al., "The microstructure and strength properties of MA957 nanostructured ferritic alloy joints produced by friction stir and elelctro-spark deposition welding," *Journal of Nuclear Materials,* vol. 367-370, no. 1, pp. 1197–1202, December 2007.

[12] F. Abe, "Precipitate design for creep strengthening of 9%Cr tempered martensitic steel for ultra-supercritical power plants," *Science and Technology of Advanced Materials,* vol. 9, no.1, pp. 1-2-15, March 2008.

[13] R. L. Klueh, "Elevated temperature ferritic and martensitic steels and their applications to future nuclear reactors," Oak Ridge National Laboratory, Oak Ridge, TN, Tech. Rep. ORNL/TM-2004/176, 2004.

[14] F. H. Huang, "Fracture toughness and tensile properties of alloy HT9 in thin sections under high neutron fluences," in *Proceedings of 15th International Symposium,* Philadelphia, PA, 1992, pp. 1267–1286, March 1990.

[15] S. Rosenwasser, "The application of martensitic stainless steels in a lifelong fusion first wall/blankets," *Journal of Nuclear Materials,* vol. 8586, no.1, pp. 177–182, March 1979.

[16] R. L. Klueh, K. Ehrlich and F. Abe, "Ferritic/martensitic steels: Promises and problems. Proceedings of the 5th International Conference on Fusion Reactor Materials," *Journal of Nuclear Materials,* vol. 191-194, no.1, pp. 116–124, September 1982.

[17] R. L. Klueh and D. R. Harries, *High-Chromium Ferritic and Martensitic Steels for Nuclear Applications,* American Society for Testing and Materials, West Conshohocken, PA, 2000.

[18] R. L. Klueh, "Elevated temperature ferritic and martensitic steels and their applications to future nuclear reactors," Oak Ridge National Laboratory, Oak Ridge, TN, Tech. Rep. ORNL/TM-2004/176, 2004.

[19] J. C. Farmer, "LIFE materials, corrosion and environmental fracture," Lawrence Livermore National Laboratory, Lawrence, CA, Tech. Rep. UCRl-TR-01 draft, 2008.

[20] G. Cam, "Friction stir welded structural materials: beyond Al-alloys," *International Materials Reviews,* vol. 56, no. 1, pp. 1–48, March 2011.

[21] J. Van den Bosch et al., "Compatability of ferritic-martensitic steel T91 welds with liquid-lead bismuth eutectic: Comparison between TIG and EB welds," *Journal of Nuclear Materials,* vol. 396, no.1, pp. 57–64, January 2010.

[22] P. Vasantharaja and M. Vasudevan, "Studies on A-TIG welding of low activation ferritic/martensitic (LAFM) steel," *Journal of Nuclear Materials,* vol. 421, no.1, pp. 117–123, February 2012.

[23] J. Rothwell and D. Abson, "Performance of weldments in advanced 9%Cr steel-'FB2,' " *Materials at High Temperatures,* vol. 27, no.3, pp. 253–264, September 2010.

[24] S. Kou, *Welding Metallurgy.* New York, NY: John Wiley and Sons, 1987.

[25] E. Lucon, A. Leenaers and W. Vandermeulen, "Post-irradiation treatment of three EUROFER97 joints," *Fusion Engineering and Design,* vol. 83, no.1, pp. 620–624, January 2008.

[26] V. Krishnardula, N. Sofyan, W. Gale, et al., "Joining of ferritic oxide dispersion strengthened alloys," *Transactions of the Indian Institute of Metals,* vol. 59, no.1, pp. 199–203, April 2006.

[27] J. L. Seran et al., "Pre and post-irradiation mechanical properties of ferritic-martensitic steels for fusion applications: EM10 base metal and Em10/Em10 welds," *Journal of Nuclear Materials,* vol. 212, no.1, pp. 588-593, December 1994.

[28] R. Lindau et al., "Mechanical and microstructural characterization of electron beam welded reduced activation oxide dispersion strengthened-Eurofer steel," *Journal of Nuclear Materials,* vol. 417, no.1-2, pp. 245-248, January 2011.

[29] H. Ogiwara et al., "Hot cracking susceptibility of F82H with controlled Ta content," *Journal of Nuclear Materials,* vol. 417, no. 1, pp. 59-62, December 2011.

[30] R. Nandan, T. DebRoy and H. Bhadeshia, "Recent advances in friction-stir welding—Process, weldment structure and properties," *Progress in Materials Science,* vol. 53, no.1, pp. 980-1023, August 2008.

[31] L. Wei and T. Nelson, "Influence of heat input on post weld microstructure and mechanical properties of friction stir welded HSLA-65 steel," *Materials Science and Engineering: A,* vol. 556, no.1, pp. 51-59, October 2012.

[32] R. Rai et al., "Review: Friction stir welding tools," *Science and Technology of Welding and Joining,* vol. 16, no.4, pp. 325-343, February 2011.

[33] H. Fujii et al., "Friction stir welding of carbon steels," *Materials Science and Engineering: A,* vol. 429, no.1, pp. 50-57, August 2006.

[34] R. Ueji et al., "Friction stir welding of ultrafine grained plain low-carbon steel formed by the martensite process," *Materials Science and Engineering: A,* vol. 423, no.1, pp. 324–330, May 2006.

[35] L. Cui et al., "Transformation in stir zone of friction stir welded carbon steels with different carbon contents," *ISIF International,* vol. 47, no.1, pp. 299–306, May 2007.

[36] P. J. Konkol and M. F. Mruczek, "Comparison of Friction Stir Weldments and Submerged Arc Weldments in HSLA-65 Steel," *Welding Journal,* vol. 86, no.6, pp. 187–195, July 2007.

[37] A. K. Lakshminarayanan and V. Balasubramanian, "Comparison of Electron Beam and Friction Stir Weldments of Modified 12 wt% Ferritic Stainless Steel," *Materials and Manufacturing Processes,* vol. 26, no.6, pp. 868–877, June 2011.

[38] H. Cho et al., "Microstructural analysis of friction stir welded ferritic stainless steel," *Materials Science and Engineering,* vol. 528, no.6, pp. 2889–2894, December 2011.

[39] M. Bilgin and C. Meran, "The effect of tool rotation and traverse speed on friction stir weldability of AISI 430 ferritic stainless steel," *Materials and Design,* vol. 33, no.1, pp. 376–383, January 2012.

[40] S. Noh et al., "Microstructure and mechanical properties of friction stir processed ODS ferritic steels," *Journal of Nuclear Materials,* vol. 417, no.1-3, pp. 245-248, October 2011.

[41] B. Baker et al., "Influence of heat input on friction stir welding for the ODS steel MA956," *Friction Stir Welding and Processing VII, TMS,* January 2013.

[42] A. Askari et al., "Analysis of friction stir welding and processing, in *Friction Stir Welding and Processing,* Materials Park, OH, ASM International, pp. 43–54, January 2007.

[43] Y. Chung et al., "Interface microstructure evolution of dissimilar friction stir butt welded F82H steel and SUS304," *Materials Science and Engineering: A,* vol. 528, no.1-2, pp. 5812–5821, July 2011.

[44] J. C Farmer et al., "Coolant compatibility studies for fusion and fusion-fission hybrid reactor concepts: Corrosion of oxide dispersion strengthened iron-chromium steels and tantalum in high temperature molten fluoride salts," Lawrence Livermore National Laboratory, Livermore, CA, Tech. Rep. LDRD final report, May 2010.

[45] P. Sabharwall et al., "Molten salts for high temperature reactors: University of Wisconsin molten salt corrosion and flow loop experiments—issues identified and path forward," Idaho National Laboratory, Idaho Falls, ID, Tech. Rep. INL/EXT-10-18090, 2010.

[46] E. T. Cheng, B. J. Merril and S. Dai-Kai, "Nuclear aspects of molten salt blankets," *Fusion Engineering and Design,* vol. 69, no.1-4, pp. 205–213, September 2003.

[47] J. C. Farmer, "Life materials overview of fuels and structural materials issues," Lawrence Livermore National Laboratory, Lawrence, CA, Tech. Rep. LLNL-TR-407386, 2009.

[48] D. F. Williams, L. M. Toth and K. T. Clarno, "Assessment of candidate molten salt coolants for the advanced high-temperature reactor (AHTR)," Oak Ridge National Laboratory, Oak Ridge, TN, Tech. Rep. ORNL/TM-2006/12, 2006.

[49] H. Nishimura et al., "Compatibility of structural candidate materials with LiF-BeF2 molten salt mixture," *Journal of Nuclear Materials,* vol. 283-287, no.1, pp. 1326–1331, January 2000.

[50] L. C. Olson, "Materials corrosion in molten LiF-NaF-KF eutectic salt," *Journal of Fluorine Chemistry,* vol. 130, no.1, pp. 67–73, May 2008.

[51] J. Farmer, S. Menon and P. LeGrand, "Effect of FSP on the electrochemical activity and passive film stability of ni-al bronze." in *Electrochemical Society Meeting,* Montreal, CAN, 2011.

[52] J. C. Farmer et al., "Corrosion of Oxide Dispersion Strengthened Iron-Chromium Steels and Tantalum in Fluoride Salt Coolant: An in Situ Compatibility Study for Fusion and Fusion-Fission hybrid Reactor Concepts," *Journal of Nuclear Materials,* vol. 419, no. 1-3, pp. 15–23, December 2011.

[53] J. C. Farmer et al., "MRS symposium proceedings 1125," Lawrence Livermore National Laboratory, Livermore, CA, pp. 41–48, 2009.

[54] T. R. Mcnelley and K. Oh-Ishi, "Microstructural modification of as-cast NiAl bronze by friction stir processing," *Metallurgical and Materials Transactions,* vol. 35A, no. 1, pp. 2951–2961, January 2004.

[55] P. Hosemann et al., "Micro-structural characterization of laboratory heats of the Ferritic/Martensitic HT-9 and T91," *Journal of Nuclear Materials,* vol. 403, no.1, pp. 7–14, May 2010.

[56] M. Mahoney and S. Sanderson, “Interim report: Taks II, demonstration of friction stir welding of small diameter tubes,” Advanced Metal Products and MegaStir Technologies, Provo, UT, 2012.

[57] A. J. Bard and L. R. Faulkner, *Electrochemical Methods, Fundamentals and Applications.* New York, NY: John Wiley and Sons, 1980.

[58] J. C. Zhao, “The diffusion-multiple approach to designing alloys,” *Annual Review of Materials Research,* vol. 35, no.1, pp. 51–73, January 2005.

[59] ASTM Standard E384-11E1, “Standard test method for Knoop and Vickers hardness of materials,” in *ASTM International,* West Conshohocken, PA, 2007, DOI: 10.1520/E0384-11E01, www.astm.org.

[60] S. K. Chimbli, D. J. Medlin and W. J. Arbegast, “Minimizing lack of consolidation defects in friction stir welds,” in *Friction Stir Welding and Porcessing IV,* Warrendale, PA, pp. 135–142, June 2007.

[61] P. Biswas, D. A. Kumar and N. R. Nandal, “Friction stir welding of aluminum alloy with varying tool geometry and process parameters,” in *Proceedings of the Institution of Mechanical Engineers, Part B- Journal of Engineering Manufacture,* vol. 226, no.1, pp. 641–648, April 2012.

[62] *A Handbook of Data about Metals and Metalworking,* American Society for Metals, Metals Park, Ohio: American Society for Metals, 1981.

INITIAL DISTRIBUTION LIST

1. Defense Technical Information Center
   Ft. Belvoir, Virginia

2. Dudley Knox Library
   Naval Postgraduate School
   Monterey, California